INVESTIGATION OF RF FRONT-ENDS FOR SIMULTANEOUS MULTINUCLEAR MR IMAGING AND SPECTROSCOPY

A Dissertation

by

CHUNG-HUAN HUANG

Submitted to the Office of Graduate and Professional Studies of
Texas A&M University
in partial fulfillment of the requirements for the degree of

DOCTOR OF PHILOSOPHY

Chair of Committee,	Steven M. Wright
Committee Members,	Krzysztof A. Michalski
	Jim X. Ji
	Mary P. McDougall
Head of Department,	Miroslav M. Begovic

August 2019

Major Subject: Electrical Engineering

Copyright 2019 Chung-Huan Huang

ABSTRACT

Simultaneous multinuclear acquisition has long been of interest due to the fact that it can provide from multiple nuclear information in a single scan. This directly reduces acquisition time and provides a potential application on quantitative analysis at multiple nuclei, e.g. hyperpolarization and MR Fingerprinting. A direct sampling is preferred for the simultaneous acquisition since the structure can simplify phase synchronization relative to mix the frequency down to baseband and sample. But this places a great demand on data throughput while digitizing a whole spectrum. Undersampling technique was introduced and applied in this dissertation but it requires a passband filtering around the resonant frequency. Another issue is that there can be a great difference in signal sensitivity between multiple nuclei. In this dissertation, a reconfigurable triplexer front-end is proposed which can provide separate filtering at different nuclei and gain controls on each signal path temporarily to improve SNR performance in a single channel digitization.

Simultaneous MR images ($^{1}H/^{23}Na/^{2}H$) were acquired by comparing the proposed narrow band front-end filtering and a wideband, low pass filtering within a single channel. The front-end approach demonstrates that a higher SNR was achieved because the front-end can provide a narrow band filtering and separate gain controls on the resonant frequencies. Both simultaneous MR images and MR spectroscopies ($^{1}H/^{23}Na/^{2}H$ and $^{1}H/^{13}C/^{15}N$) are further compared with single nuclear acquisition from the Varian system, showing that the front-end performance is comparable to a commercial system but using

a less complex structure. Additionally, for simultaneous MR spectroscopy, single channel digitization performs as well as three channel digitization separately. This validates that an improvement on data throughput by generating only one third data size when comparing to digitizing each of the nuclei separately and allows other digitizer channels to be available for array application. Large signal dynamic range is also conducted in this dissertation to verify the benefit of the triplexer front-end can achieve at a higher SNR for all nuclei.

An array can offer multiple advantages over single element and is desirable, but coupling between elements has always been a major issue. Currently, conventional approaches to decouple are limited either by coil geometry or to a single frequency and a complex matching and tuning circuit may be required to decouple multiple nuclei with existing approaches. Therefore, a preamp decoupling approach was proposed with a fixed series resonant circuit and was evaluated based on a high input impedance Op Amp across multiple bands. Noise models of an Op Amp were developed to find an acceptable NF region condition. Impedance transformation and decoupling were also evaluated at $^{1}H/^{13}C/^{15}N$. The overall evaluation of the approach provides a possibility on the multiband array decoupling with an ease and fixed structure.

ACKNOWLEDGEMENTS

I would like to thank my advisor, Dr. Steven Wright, for bringing me into this field and guiding me on the path of the research road. I also want to extend my appreciation to my committee members, Dr. Krzysztof Michalski, Dr. Jim Ji, and Dr. Mary McDougall for spending their time on my topic.

Thanks also go to my lab colleagues for the knowledge what they had shared and the discussions what we have had.

Lastly, I am here to show my sincere thanks to my family. For my wife, Chien-Wei, thank you for your support, patience, and taking care of our kids during these years. For my two kids, Hannah and Alfie, thank you for giving me fun while I was stressful and frustrated.

CONTRIBUTORS AND FUNDING SOURCES

Contributors

This work was supervised by a dissertation committee consisting of Professors Steven Wright (advisor), Krzysztof Michalski and Jim Ji of the Department of Electrical & Computer Engineering and Professor of Mary McDougall of the Department of Biomedical Engineering.

Funding Sources

Graduate study was supported by the sponsorship of National Chung-Shan Institute of Science and Technology in Taiwan.

Broadband system was built previously, and available by MRSL student for this research.

NOMENCLATURE

TAMU	Texas A&M University
MRSL	Magnetic Resonance Systems Lab
MRI	Magnetic Resonance Imaging
MRS	Magnetic Resonance Spectroscopy
T	Tesla
QWTL	Quarter-Wavelength Transmission Line
RF	Radio Frequency
Tx	Transmit
Rx	Receive
EM	Electromagnetic
Op Amp	Operational Amplifier
LNA	Low Noise Amplifier
ppm	Parts Per Million
ADC	Analog-to-digital Converter
TL	Transmission Line
NF	Noise Figure
FID	Free Induction Decay

TABLE OF CONTENTS

Page

LIST OF FIGURES

Page

LIST OF TABLES

CHAPTER I

INTRODUCTION

I.1 Motivation

Statistics from the American Cancer Society show that an estimated 1.7 million new cases of cancer will be diagnosed across the United States and around 0.6 million people will die from the disease in 2018 [1]. Additionally, American Cancer Society even indicates that the number of people diagnosed with cancer reached 14.1 million in 2012 and is expected to rise to approximately 23.6 million by 2030. Accompanied by the rapid increase of those people suffering with cancer, improved methods to detect and monitor the progression of cancer is of critical importance.

Currently, nuclear magnetic resonance (NMR) has been widely used in determining chemical composition and molecular structure to monitor cellular metabolism of cancer [2-4] with applications of NMR spectroscopy or magnetic resonance spectroscopy (MRS) and imaging (MRI) due to its non-invasive method on clinical diagnostics [5, 6]. Different nuclei have separate capability for monitoring specific metabolisms. Some of them have very low signal sensitivity which can be improved by using hyperpolarization technique [7-9]. The observation on organic compounds may be studied by ^{13}C spectroscopy. Typically, ^{13}C is used to provide information about glucose metabolisms [10, 11], and is commonly used as a quantitative way to measure metabolic flux as a biomarker. Another nucleus example is ^{15}N, the changes in nitrogen metabolism such as glutaminolysis, nucleotide biosynthesis, and glycolysis, is able to help us to discriminate normal and cancerous tissues through breast cancer biopsies [12]. Besides

the above two isotopes, there are other nuclei that can be used for different type of diagnosis, i.e. ^{23}Na is used for a tissue tumor malignancy indicator through tissue sodium concentration [13, 14]. However, most commercial systems have limited capability to provide multiple nuclear information in a single scan. This directly increases total scan time and operating cost if we would like to access multiple biomarker information at the same time, especially in hyperpolarization application. Therefore, acquiring multiple nuclei in a single scan is always desirable since the more nuclei we are able to obtain, the more metabolic information we can access and this brings us to the interest on multinuclear acquisition during these years [15-17].

I.2 Challenges and objective

Most in vivo multinuclear MR experiments are involved with single frequency acquisition currently. However, these systems expose an issue that can only provide limited metabolic information in a given fixed scan time. To address this issue, there are some groups already investigating multinuclear acquisition and this can be back to 1980s [7, 15, 18-21]. Generally, interleaved and simultaneous acquisition are ways to acquire multiple nuclei. The difference between two approaches is that interleaved method obtains multiple nuclei at different time window whereas truly simultaneous method acquires all nuclei in a same time period. In the early times, conventional interleaved acquisition of different nuclei was regarded as sufficient. However, this may not be available when novel techniques emerge, i.e. hyperpolarization [7, 22] and MR Fingerprinting [23], due to the duty cycle of data acquisition has been increased in MRI and MRS for multinuclear acquisition. As of today, simultaneous acquisition can be achieved by modifying existing

MR scanners, but most are still limited to dual nuclei [7, 16]. Importantly, current simultaneous acquisition is based on mixing down frequency to the baseband instead of using direct sampling. This approach involves more analog components, i.e. mixers, LOs, IF amplifiers, filters, etc. For a high-channel-count system, direct sampling can simplify phase synchronization between devices while there is no mix down stages.

Another issue raised here is that most of dual frequency schemes utilize separate coils [24]. Separate multituned coils can be applied without the proposed front-end, but this will complicate the coil setup in the limited space of a magnet. Importantly, digitizing different nuclei separately will result in a higher data throughput. Combining different nuclei signals can improve the data size issue since it only digitizes one channel data. A proper filtering at resonant frequencies is also necessary when applying undersampling technique to prevent out of band signal and noise folded into the desired bandwidths. Thus, one of the challenges now is to investigate a filtering front-end structure where the frequency can be changed easily to fit different nuclei and also can help on transition from systems to systems with different magnetic fields very quickly in the simultaneous multinuclear acquisition.

Another challenge of multinuclear simultaneous acquisition in the recent years will be decoupling arrays at multiple frequencies. Array coils are desirable to improve signal-to-noise ratio (SNR), resolution and scan time. However, decoupling between array coil elements is always a main concern because coupling effect can cause degradation on the SNR performance [25]. Therefore, decoupling between array coils must be in good isolation to prevent induced current from other coils. Today, there are three major

approaches for array decoupling, e.g. inductive decoupling, capacitive decoupling, and preamp decoupling [26-29]. Nonetheless, these approaches are constrained either to single frequency or geometry structure of coils. This could be a major issue if implementing arrays at multiple frequencies. In this dissertation, we will evaluate a possibility of using high input impedance operational amplifiers for preamp decoupling with preliminary results. With such configuration, it can provide a much simpler way to carry out the implementation and also facilitate the operation process of multi-tuned array in the future.

To complete the challenges, the primary objective of this dissertation is to investigate a simple structure which can be applied to simultaneous acquisition at multiple frequencies with undersampling technique. Furthermore, preliminary results of using high input impedance as preamp decoupling will be evaluated. This could be achieved by separate the dissertation into three specific aims.

Aim 1: Develop a reconfigurable RF filtering front-end at dual nuclei and compare the performance with commercial diplexers.

Aim 2: Expand the front-end to three nuclei which is capable of acquiring up to three nuclei MRI and MRS simultaneously and evaluate the performance with single frequency acquisition using a Varian system.

Aim 3: Evaluate the possibility of using a high input impedance operational amplifier for array decoupling at multiple nuclei while still maintaining low NF.

I.3 Dissertation organization

The dissertation is divided into six chapters as follows:

Chapter I introduces the motivation, challenges and objective, and organization of the dissertation.

Chapter II gives the fundamental background to this research, i.e. NMR signal generation, slice excitation at multiple nuclei simultaneously, MR system configuration, undersampling technique, hyperpolarization technique, and array decoupling approaches.

Chapter III describes a flexible RF filtering front-end design for two nuclei (^{1}H and ^{23}Na) MRS with quarter-wavelength transmission line (QWTL) structures. In this chapter, both simulation and experimental results were compared to verify the performance between the QWTL filtering front-end and the commercial diplexers. Additionally, undersampling technique was employed to reduce data throughput by using an Ultraview digitizer. The results show that the QWTL filtering front-end structure can have similar performance as the commercial diplexers but providing a flexibility on frequency selection. In the meantime, the front-end structure allows us to apply different gain at each of the signal paths to optimize signal sensitivity to different nuclei.

Chapter IV presents a true simultaneous MRI and MRS acquisition with a reconfigurable front-end at three nuclei (^{1}H/^{23}Na/^{2}H and ^{1}H/^{13}C/^{15}N). The narrow band filtering front-end is expanded to fit three nuclei from the one in Chapter III. Initially, the front-end was tuned to fit ^{1}H/^{23}Na/^{2}H since these nuclei have a larger signal sensitivity and samples are easier to obtain while comparing to ^{1}H/^{13}C/^{15}N. Additionally, both ^{2}H and ^{23}Na Larmor frequencies are close to the interested nuclei, ^{15}N and ^{13}C, respectively. This can facilitate the system transition on different nuclei. Simultaneous acquisition was implemented with a home-built broadband system and the proposed front-end. The results

were compared with single nuclear acquisition with a commercial MRI spectrometer (Varian Unity Inova). Simultaneous multinuclear MRI and MRS were obtained at $^{1}H/^{23}Na/^{2}H$ whereas only simultaneous MRS was acquired at $^{1}H/^{13}C/^{15}N$. The results show that the front-end with simultaneous MRS can perform as well as the Varian system with single frequency acquisition at both $^{1}H/^{23}Na/^{2}H$ and $^{1}H/^{13}C/^{15}N$. Simultaneous MRI with the front-end filtering even demonstrates that a better SNR was achieved over a wideband, low pass filtering structure because it can provide separate filtering and gain controls at each signal path to best use a digitizer's dynamic range for nuclei where the sensitivity varies a lot. Moreover, with the simultaneous acquisition schematic, one channel digitization MRS results were compared with three channel digitization by separating three filtered signals into different input channel of the digitizer. The results demonstrate single channel digitization can perform as well as three channel digitization separately but generating less data throughput and use less input resource of the digitizer. Signal dynamic range between two nuclei with large difference on sensitivity is also investigated by optimizing a constant gain to all nuclei either at proton and carbon. While compared to the triplexer front-end, the front-end presents an improvement on SNR, showing the benefit to apply separate signal conditioning for each nuclear.

Chapter V focuses on using a low noise, high gain, wide bandwidth, and high input impedance Op Amp as a preamplifier decoupling approach for array coils. In this chapter, NF of an Op Amp will be studied by developing Op Amp noise models. This chapter also compares the performance of an Op Amp based preamplifier to a commercial preamplifier to verify the NF performance. Series resonant circuit with impedance transformer was

simulated to achieve an acceptable NF region at $^{1}H/^{13}C/^{15}N$ and a good decoupling at X-nuclei. Overall evaluation shows a possibility of using this approach to decouple arrays at least at two frequencies.

Chapter VI summarizes the important findings of this research in the dissertation. Improvement of future work is also discussed in the chapter in implementing multi-channel simultaneous acquisition at multiple frequencies.

CHAPTER II

BACKGROUND

II.1 Magnetic resonance signal

NMR signal is sometimes referred to free induction decay (FID). This is essential information to reconstruct MRI or MRS. In this section, we will introduce how a MR signal being produced and transformed into a form that we are familiarized with, e.g. an image. Essential backgrounds related to this dissertation will be discussed in the following.

II.1.1 Spin excitation

Only nuclei with a nonzero net spin number can have MR signals, i.e. ^{1}H, ^{13}C, ^{15}N and etc. In general, nuclei net spin number (I) can be categorized into three groups, half integer, integer, and zero, based on number of protons and neutrons. A charged particle will create a magnetic momentum along the spin axis shown in Figure 1. black arrow through the particle. A zero net spin number nuclear, for example ^{12}C, does not allow to have spin phenomena. This will result in no magnetic momentum being generated. Thus, this is why we are not interested in about this type of nucleus in NMR due to no signal can be detected.

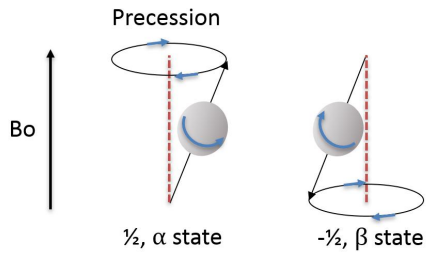

Figure 1. A charged particle spin around its spin axis and precession along external magnetic field.

A nucleus with net spin number not equal to zero, e.g. half integer net spin number, is known that there will be two orientation states (α state or β state) when applying an external magnetic field. A charged particle such as electron or proton can precess about an external applied magnetic field. The frequency of precession or Larmor frequency is defined as the number of times per second which the particle precesses about a vertical axis (red dashed line) in Figure 1. This Larmor frequency increases with the strength of B_0 times a constant known as a gyromagnetic ratio. The gyromagnetic ratio differs from nucleus to nucleus.

Table 1 shows some commonly used nuclei properties including net spin number, gyromagnetic ratio and its natural abundance [30]. Therefore, Larmor frequency of each nucleus can be calculated based on

$$f_0 = \gamma B_0 \tag{1}$$

where γ is the gyromagnetic ratio of the nucleus and B_0 is the static magnetic field. For example, proton Larmor frequency is about 200.1 Mhz at 4.7 T. A resonance condition can be met if RF frequency is the same. This allows energy transition between α and β states since the energy difference corresponds to this frequency, resulting in proton spins absorbing the RF signal energy. A proton FID signal then will be released in a RF form when the RF source signal is turned off due to all spins return back to an equilibrium state.

Table 1. Common nuclei properties including net spin number, gyromagnetic ratio, natural abundance, and relative sensitivity [30].

Nucleus	Net spin	Gyromagnetic ratio (Mhz/T)	Natural Abundance (%)	Relative Sensitivity
^{1}H	1/2	42.577	99.985	1
^{2}H	1	6.536	0.015	$1.45x10^{-6}$
^{13}C	1/2	10.708	1.1	$1.75x10^{-4}$
^{15}N	1/2	- 4.317	0.366	$3.82x10^{-6}$
^{19}F	1/2	40.053	100.00	0.834
^{23}Na	3/2	11.27	100.00	0.0927
^{31}P	1/2	17.251	100.00	0.0665

II.1.2 MRI slice excitation

To image a certain desired slice in a phantom requires the FID come from spin resonance within that desired section. However, with a perfect uniform magnetic field, all spins present same resonant frequency without spatial information. Thus, gradients are needed to generate a spatial-varying magnetic amplitude depends on spin location. Within this magnetic gradient region, spins precess slightly differently due to the gradient field adds or subtracts from the main magnetic field. In general, slice select gradient allows us to choose the desired slice image whereas frequency encoding and phase encoding are two gradients for two-dimensional NMR signal mapping. MRI images then can be acquired

by postprocessing the NMR signal in k-space with Fourier Transform. There will be more detailed information on MRI principle in references [31-33] if interested.

In general, a trans-axial selective slice excitation RF bandwidth (tBW) will be inversely proportional to its length and can be realized based on following equation,

$$\mathrm{tBW} = \gamma G_{ss} \Delta z \tag{2}$$

where γ is the gyromagnetic ratio of the excited nucleus, G_{ss} is the slice select gradient strength, and Δz is the slice thickness of excitation plane. We can observe that the thickness of the slice is basically determined by three factors, gradient strength, nuclear gyromagnetic ratio, and excited RF pulse bandwidth.

Generating multiple RF pulses concurrently is unavoidable while implementing simultaneous acquisition at multiple frequencies. This results in either different slice thickness at each of the interested nuclei if the RF bandwidth and the slice select gradient are fixed, or the RF bandwidth varies with different nuclei if the gradient strength and the slice thickness are constant. Similarly, if a same gradient either in frequency encoding or phase encoding direction is applied to different nuclei, FOV in two directions will vary and is depended on nuclear gyromagnetic ratio if receiver bandwidth and phase encoding time are fixed. This imposes a challenge on the simultaneous multinuclear acquisition, but it may be resolved by applying a complex pulse sequence which is not discussed here. In this dissertation, we simply implemented a pulse and acquire sequence with hard pulses at three frequencies for the MRS experiments and a gradient echo sequence with sinc pulses with same gradient fields to each nuclear for the MRI experiments to demonstrate the capability of simultaneous acquisition.

II.2 Magnetic resonance system

A MR system hardware is necessary in order to acquire NMR signals. Generally, a MR system, illustrated in Figure 2, consists of a main magnet, shim coils, a waveform generator including RF amplifiers, gradients, receiver chain including spectrometers, and a host computer.

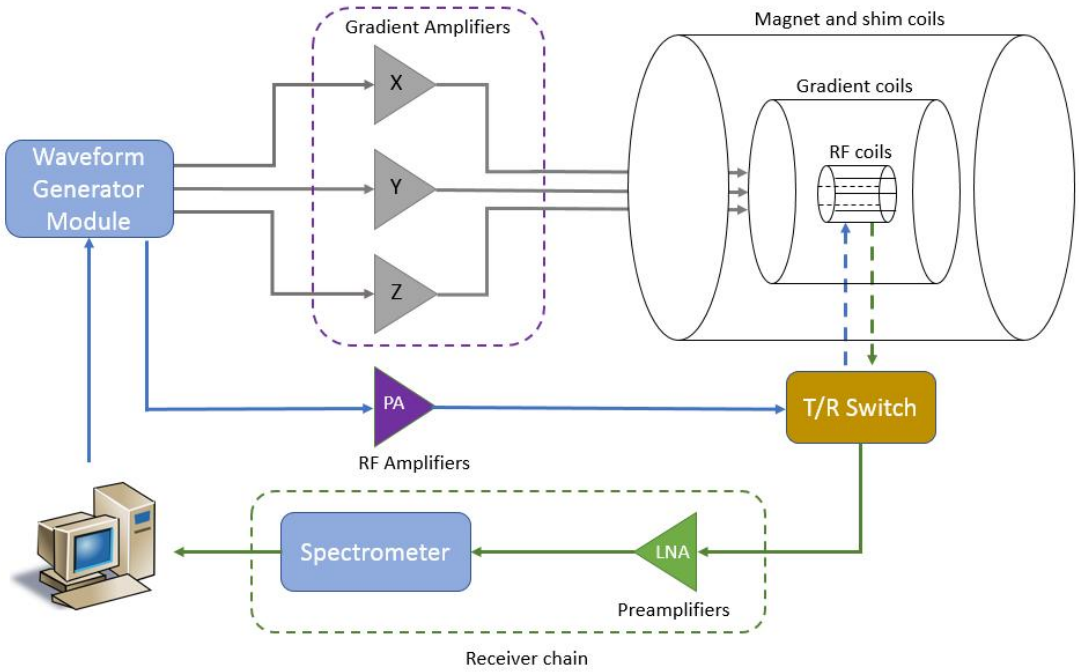

Figure 2. A MR system function block diagram.

II.2.1 System hardware

In Figure 2, the main static magnet determines the NMR signal strength directly and most research nowadays is primarily based on high field scanners [34, 35]. Shim coils are used to compensate the static magnetic field to be more uniform to increase received

signal intensity [36]. The RF amplifier is used to amplify transmitted RF pulses whereas the spectrometer can acquire received signals. The gradients are known to generate a 3-dimensional varying field strength where these fields will correspond to slightly different resonant frequencies. This allows us to excite and acquire specific region of the spins [33]. A host computer serves as a control center where it can determine the parameter setting and display acquired images or spectroscopies on the monitor.

RF coils are also necessary to transmit and receive signals which is not shown here within the system. As of today, there are two main types of probe coils, i.e. volume coils and surface coils. Volume coils normally can have a better uniform B_1 field rather than surface coils [37]. In order to keep a homogenous field in the region of interest, volume coils are often used as a Tx coil. On the other hand, Rx coil is responsible to detect and receive the MR signal. Sometimes, the detecting region is only a small portion of body. Thus, it is quite often to have surface coils as a receive coil to provide an uniform excitation field locally with higher SNR [38].

II.2.2 Undersampling

In a commercial spectrometer, the receiver chain typically contains mixers which are used to convert the oscillating frequency down to baseband. The function block diagram can be seen in Figure 3. While the receive signal is generated from RF coils and being amplified, the amplified signal will then be mixed with a local oscillator and digitized by an analog-to-digital converts (ADCs). However, most of the spectrometers are involving more than one mix down stage, resulting in more components such as mixers being added in the receiver chain. Moreover, multi-channel acquisition leads to use more

ADCs in the spectrometer. All of above adds uncertainty to phase stability and increase system complexity while performing multi-channel acquisition at multiple frequencies. Therefore, the research presented in this dissertation proposes a direct sampling approach.

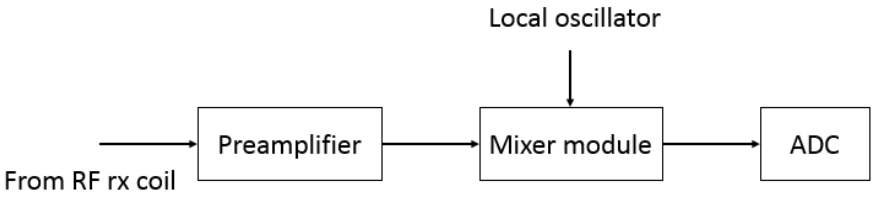

Figure 3. Receiver chain function block diagram with down converters.

Today, most applications including NMR signal have very limited interest bandwidth of kilohertz order around the resonant frequencies. Even though high technique electronics allow us to acquire a whole spectrum at high frequencies, this places a great demand on data throughput. Thus, undersampling technique is often desirable to reduce throughput load during digitization. As this technique has already been widely used in various fields, e.g. radar image, communication [39, 40], however, undersampling scheme with multinuclear simultaneous structure is relatively new in MR field. One of current researches focuses on dual nuclei simultaneous recording with this technique [15]. Unfortunately, this is implemented at a low field (0.5 T) scanner and the receive signal is mixed down to audio frequencies instead of direct sampling.

In general, reconstruction of original waveform is permitted if a sampling rate is twice of a signal bandwidth where the sampling rate is lower than the Nyquist rate. But

this replies on a proper filtering. Figure 4 (A) illustrates two waveforms with different sampling rates in time domain. Dots are regarded as sample points. We can observe that blue curve has a sampling rate larger than Nyquist rate, resulting in a correct waveform reconstruction. However, using a lower sampling rate for blue curve can trace out another lower frequency waveform presented in red curve if there is no proper bandpass filter. This makes samples become indistinguishable from the samples of a lower frequency and aliasing of high frequency signal. Figure 4 (B) presents a point of view from frequency domain. A bandpass filter is applied around a signal band. While using the undersampling technique, original signal band will alias down to the Nyquist region. But since we already filter all out of band noise in advance, thus aliased band still contain original waveform integrity. This makes us able to reconstruct the waveform correctly without distortion but with less data throughput.

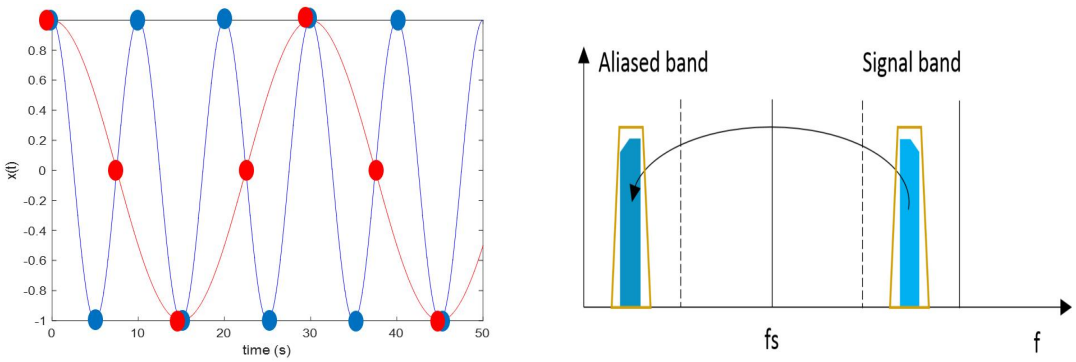

(A) (B)

Figure 4. (A) Two waveforms are digitized with different sampling rate in time domain. Insufficient sampling rate causes aliasing in a lower frequency (red curve) when reconstructing original signal. (B) Applying proper bandpass filtering at high frequency allows original signal being reconstructed correctly in frequency domain.

II.3 Hyperpolarization

Today, NMR is able to provide useful biomedical information. However, low sensitivity of some nuclei is still a big challenge till now. From Table 1, some of the isotopes such as ^{13}C and ^{15}N, the natural abundances are only about 1.1% and 0.4%, respectively. Furthermore, nuclei with short T_1 time are difficult to detect. Therefore, researchers in MRS/MRI have been devoted to acquiring higher signal level for a long time due to higher signal intensity can lead to a higher resolution on imaging and larger signal-to-noise ratio (SNR) on spectroscopy. This directly helps to identify and track disease much faster and more precisely.

Dynamic nuclear polarization (DNP) is recently developed and is regarded an emerging technique to enhance the sensitivity of spins for more than 10,000-fold by transferring high polarization from electrons to nuclei [8]. Figure 5. presents spin polarization curves at different temperatures for both ^{13}C and electron based on the following equation,

$$\mathbf{P} = \frac{n_\beta - n_\alpha}{n_\beta + n_\alpha} = \boldsymbol{tanh}\left(\frac{\gamma \hbar B_0}{2kT}\right) \tag{3}$$

where γ is gyromagnetic ratio of the spin, $\hbar$ is the Planck's constant, B_0 is the applied external magnetic field, k is the Boltzmann constant, and T is temperature. We can observe that even with state-of-the-art magnet, ^{13}C polarization has increased from 0.08 % to 0.4 % when comparing to 4.7 T at 1.5 K. But the improvement is relatively small while comparing to electron polarization at same temperature. This characteristic allows us to build up nuclear polarization more efficiently instead of increase main magnetic field

strength. This is the reason why researchers are fascinated with this technique to improve nuclear sensitivity.

Importantly, the DNP was successfully quantified the exchange between $^{13}C_1$-pyruvate, $^{13}C_1$-lactate, and $^{13}C_1$-alanine with kinetic modeling and animals with dose-response [41]. This provides an approach that pyruvate-lactate exchange can be used an observation *in vivo* to identify the tumor grade and monitor the treatment efficiency more precisely. But there are limitations using the DNP when acquiring signals, e.g. the decaying time of polarized spins can only last few seconds to minutes and waiting time for cooling down sample solution may take up to couple of hours. This directly limits the number of observations that can be made in a given period of time where the case is considered under single nuclear acquisition. Thus, more time will be needed if involving multiple nuclei detection when using conventional single frequency acquisition. This again motivates us on simultaneous acquisition for multiple nuclei in hyperpolarized applications.

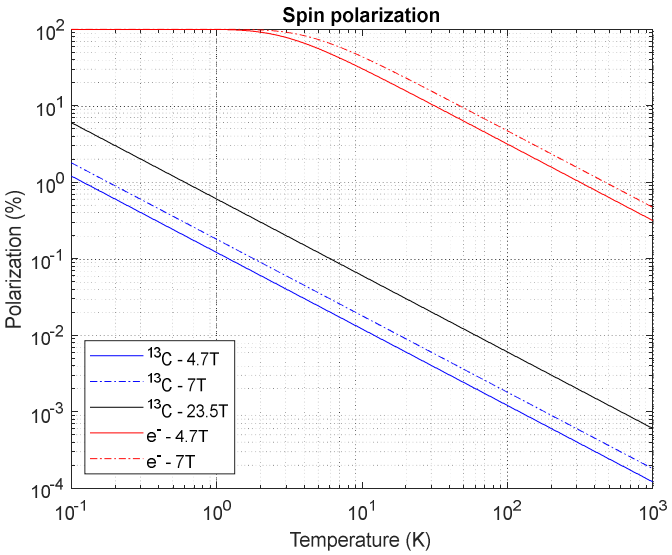

Figure 5. ^{13}C and electron polarization curves at different temperature and magnetic field strengths.

II.4 Array element decoupling

In order to have better sensitivity on the NMR signal and less scan time by acquiring undersampled k-space data, parallel acquisition has become a popular research topic in the recent years [42, 43]. This leads a lot of MR instrument vendors start to develop multiple receiver channel systems. We believe this will extend to multi-nuclear arrays. However, induced current from other coils could be a major issue due to coupling will result in degradation on SNR [44].

As of today, there are three major decoupling approaches, inductive decoupling, capacitive decoupling, and preamp decoupling. Inductive decoupling uses overlapping geometry between neighboring resonant element coils to cancel magnetic fluxes resulting in zero mutual inductance [29]. However, non-adjacent elements still have induced current

existing which causes coupling effect. Additionally, this approach cannot work perfectly in coils that are more than three elements due to geometry limitation [45]. Capacitive decoupling involves with ladder networks to achieve zero mutual inductance between coils [28]. Even this method allows us to apply decoupling to non-adjacent coils, a symmetric coil arrangement is required and the resistive coupling is not taken into consideration. Preamp decoupling is the most fascinating decoupling method replying on low input impedance preamplifiers. Generally, the induced current will be minimized between coils due to input impedance looking from coil to preamplifiers is high [26, 27, 29] which is shown in Figure 6 (A). Hence, decoupling is achieved and the approach can easily be applied if coils are separated over a wide range of distance. However, there is no such multi-frequency commercial isolating preamplifiers available, and most single frequency isolating preamplifiers are expensive. Thus, we think it may be feasible to use the high input impedance characteristic of an Op Amp to perform this preamp decoupling. The proposed structure is shown in Figure 6 (B). The advantage of using this method is that it is more inexpensive with less complex structure but can be applied to multiple frequencies with fixed tuning circuit since acceptable NF region can across wide range of source impedances.

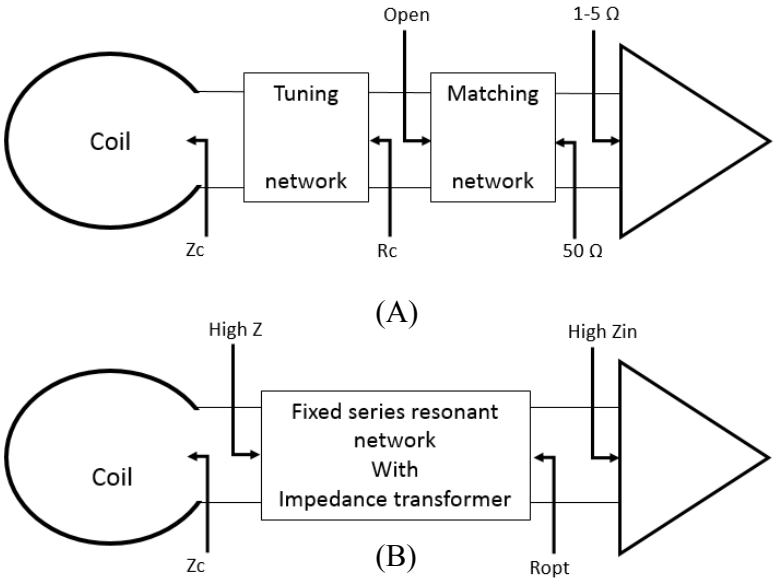

Figure 6. (A) Conventional preamp decoupling diagram and (B) recommended structure with a high input impedance Op Amp.

Preamp decoupling method allows us to isolate induced current between coils, but noise degradation of preamps still needed to be taken care of. In MR systems, coil dominated noise or sample dominated noise level is on the order of microvolt to nanovolt. If system noise is larger than picked up noise, MRI/MRS SNR will degrade. In 1944, Friis had already defined the NF equation to determine SNR degradation [46]. For a nth-cascaded system, overall NF can be derived as,

$$F_{total} = F_1 + \frac{F_2 - 1}{G_1} + \frac{F_3 - 1}{G_1 G_2} + \cdots + \frac{F_n - 1}{G_1 G_2 \cdots G_{n-1}} \quad (4)$$

where F_n and G_n are the NF and gain of the nth stage device, respectively. It is apparently that the first stage NF dominates the total NF of the system. Therefore, it is important to keep the NF of first stage, normally is LNA, as small as possible in order to maintain

intrinsic SNR. According to Cao X., *et al.* [47], an intrinsic SNR of a MR system will degrade by about 5 % if the first stage LNA has a NF of 0.5 dB and a gain of 25 dB. In such case, noise contributed by the later stages only increases a little without affecting overall performance. However, if the LNA has a NF of 6 dB, the SNR at output of the system drops to 50 % of the intrinsic SNR. Improving on the main magnetic field will still improve SNR with such LNA specification, but the SNR cannot be optimal.

In the early years, preamplifiers were designed to match to 50 Ω in order to have a maximum power transfer to loads [48], but NF of preamplifiers may not be optimized in such case. At that time, arrays were not quite popular so decoupling between coils was not aware of. As time passes by, more and more groups are involving with arrays on parallel imaging [42, 43, 49, 50], decoupling between coils has become a major issue. The decoupling issue will be the same for multi-nuclear arrays in the future. Thus, here we analyze noise models for an Op Amp based on Karki [51], allowing us a more flexible way to design a preamplifier with an high input impedance Op Amp for the preamp decoupling. This can minimize induced current flowing through the amplification stage but still maintaining original data integrity [25].

CHAPTER III

RECONFIGURABLE RF FILTERING FRONT-END FOR DUAL NUCLEI[1]

III.1 Introduction

Nowadays, we are able to digitize a wide spectrum which contains the bands of interest with a high-speed digitizer. But this places a great demand on data throughput and most high resolution digitizers are pricey. Undersampling technique is one way to reduce data throughput with an affordable digitizer. However, undersampling requires passband filtering around the resonance frequency of each nuclei to prevent out of band signal and noise. Unlike conventional single nuclear acquisition, applying one bandpass filter can only filter one frequency but removing the rest of interested bands. Importantly, different nuclei may have huge signal sensitivity variation. This may be an issue while acquiring multiple nuclei simultaneously. Therefore, here we present a simple method to separate data paths to filter two nuclei (^{1}H and ^{23}Na) by using a quarter-wavelength transmission line (QWTL) filtering structure shown in Figure 7 with the undersampling technique. An incoming signal was picked up by a receive coil and passed through a LNA prior to channelization. The filtered signals then being combined back before digitization. Since we separate each nucleus in its own data paths, independent gain is available by adding attenuators to each of the data paths in order to best use of the receiver's limited dynamic range.

---

[1] Reprinted with permission from "Flexible RF Filtering Front-End For Simultaneous Multinuclear MR Spectroscopy" by C.-H. Huang, S. E. Ogier, M. Gu, S. M. Wright in 40th Scientific Meeting, USA. Copyright 2018 by IEEE Engineering in Medicine and Biology Society.

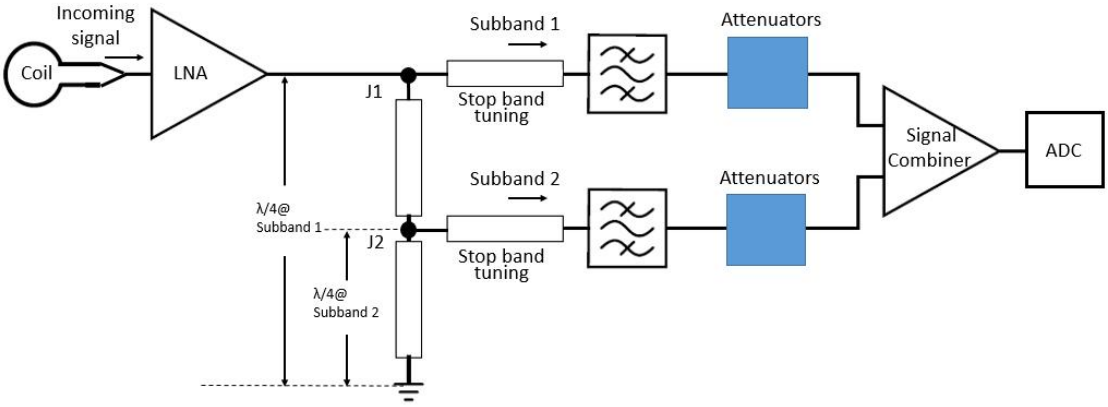

Figure 7. A dual band receiver chain for ^{1}H and ^{23}Na MRS uses a QWTL front-end followed by a stop band transmission line and a bandpass filter at each data path. Separate gain at each data paths is allowable after two bandpass filters. Two filtered data are combined before digitization. "Reprinted with permission from [52]."

There are several ways to multiplex and demultiplex signals to alleviate the issue of scarce resources in a wideband system, i.e., using diplexers or duplexers, or even more complex methods such as time-domain multiplexing, frequency-domain multiplexing techniques, and etc. [53-55], and diplexers or duplexers have been utilized for a long time as a splitter or combiner for processing signals because of their ease of use. However, a constraint of using a diplexer is the limited flexibility on frequency selection. Most commercial diplexers are built with a low passband region ranging from DC to fifty megahertz or higher and a high passband region from a hundred to several hundred megahertz. Therefore, the MRS results at ^{1}H and ^{23}Na were compared with using the commercial diplexers structure to verify the performance of the QWTL with an advantage of flexible frequency selection.

III.2 Design of reconfigurable RF filtering front-end

In this section, we are going to describe how to design a reconfigurable RF filtering front-end hardware. The hardware basically consists of a QWTL front-end (or known as a QWTL diplexer in this chapter) with a signal combiner and data acquisition.

III.2.1 QWTL diplexer with tunable stopband TL

As illustrated in Figure 7, the QWTL front-end was composed of two series of QWTLs made of Belden RG58A/U and BNC T-connectors, allowing the frequency bands to be easily changed. Two section QWTLs can provide high impedance toward ground to two desired signal bands due to inverse admittance of QWTL characteristic, i.e. 52.6 MHz (subband 1 – ^{23}Na) and 200.125 MHz (subband 2 – ^{1}H), at the input of each data path respectively. Thus, J1 port appeared an open to subband 1 and subband 1 is directed to the upper path. In the meantime, J1 port showed as a short to ground to subband 2, directing subband 2 to J2 port. At J2 port, it presented an open to ground to subband 2 and directed subband 2 go along the lower path. A tunable stopband TL was added to each data path after the QWTL structure by providing an electrical open to neighboring passband frequency. M. Karlsson. et al., mentioned that an input impedance looking into stopband TL at both channels should be greater than 600 Ω at neighboring frequency in order to have a good forward transmission. A fine tune on the tunable stopband TLs is necessary so that the return loss of desired band is larger than 15 dB and unwanted band is lower than 10 dB in the design.

III.2.2 Bandpass filter

Bandpass filters may not be necessary if acquiring data with a fully sampling rate. However, we in general use the undersampling technique for data acquisition, so bandpass filters with specific bandwidth and center frequency at the two desired subbands are required to filter aliased noise. Since MR signals are in narrow bands, bandwidth of filters is not necessary to be large. In our experiments, a 200 MHz (2800-SMA, KR Electronics Inc., NJ) bandpass filter with a 3db bandwidth of 6 Mhz and a 50 MHz (2867, KR Electronics Inc., NJ) bandpass filter with a 3db bandwidth of 9 Mhz are selected.

III.2.3 Two port signal combiner

A wideband and low distortion Op Amp from Texas Instruments (OPA843) was chosen as the main structure of the signal combiner by summing up two signals together [56]. The reason to choose OPA843 is that its bandwidth can cover our highest observed frequency, 200 Mhz, with a unity gain. Additionally, it has very low input voltage noise which is $2\text{nV}/\sqrt{\text{Hz}}$. In other words, only small amount of noise will be added to original signal noise level. From Figure 8 (A), it can be seen that noise gain is designed to equal to 3 giving a 500 Mhz bandwidth at a gain of -1 for each of subbands to maintain loop stability. Additionally, input termination resistors R_1 and R_3 were added to adjust input impedance for both inputs to a lower value when R_2 and R_4 were high values. In our design, both R_2 and R_4 were same with R_7 (unity gain) where R_7 in larger values can reduce the output loading and improve harmonic distortion performance. Thus, with a gain of -1, both R_2, R_4 and R_7 were 402 Ω. This required R_1 and R_3 to be 57.1 Ω to perform a 50 Ω input impedance to match to signal source for both inputs. Since OPA843 is a high-speed

input stage device, a relatively high input bias current will be presented, resulting in a dc offset at output. In order to reduce dc term error, total DC impedance looking out of each input port should be matched for bias current cancellation. Thus, shunt resistors R_5 and R_6 were placed in parallel at the noninverting input to present a compensation resistor of 140 Ω. The value of the compensation resistor was calculated based on parallel impedances looking into two signal sources and output where source impedances and the feedback resistor are included. The circuit diagram was fabricated through LPKF with a two-layer copper FR4 board shown in Figure 8 (B) for parasitic capacitance reduction. In general, adding an active component will result in an additional noise being added and degrade SNR. But since we placed a low noise preamplifier as an initial stage in the receiver chain where this circuit is at a later stage. The dominated NF will be dominated by the preamplifier and cascade NF can be calculated to observe the NF variation when adding this signal combiner. The overall NF increment is about 0.1 dB difference.

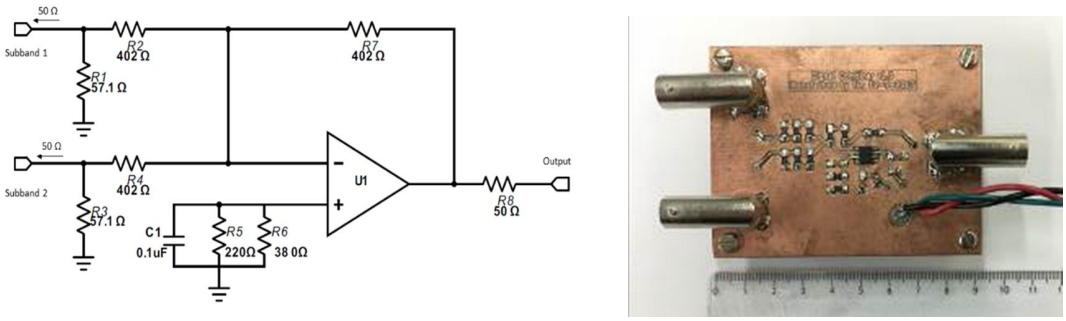

(A) (B)

Figure 8. (A) Two-port signal combiner circuit schematic and (B) physical hardware top view with a ruler scaled in cm. The signal combiner was fabricated in a two-layer FR4 board. "Reprinted with permission from [52]."

III.2.4 PC-based data acquisition

Combined signals after the signal combiner were directly digitized by a 16-bit, 250 MS/s/ch, 4-channel ADC acquisition card (AD16-250, Ultraview Corp., CA). Because this sampling rate is below the Nyquist rate for the ^{1}H frequency, a sampling rate of 230 MS/s was used to ensure that the aliased ^{1}H frequency was separated from the ^{23}Na frequency. A Labview program provided by the manufacturer was used to control the Ultraview.

The Ultraview digitizer provides a function to acquire data from external triggers which is provided from the Varian. This trigger is regarded as Selective Recording and is a TTL level. However, the trigger level is recommended between 0 V to 2.5 V with a maximum of 3.3 V. In order to get a precise timing of the trigger signal, this input was synchronized with the same clock as used in the digitizer and broadband system front stage, multifunction I/O PCIe-6363 board (National Instruments). Even though the control trigger signal was generated from PCIe-6363, however, the PCIe-6363 was programmed to providing a 10 V pulse signal. This is not able to be used directly to control the Ultraview ADC. Therefore, a voltage regulator capable of generating a TTL with maximum voltage of 3.3 V is needed. Thus, an additional octal transceiver bus circuit, shown in Figure 9 (A), was designed to convert the TTL trigger signal to +2.2 V from damaging the Ultraview digitizer and also can improve TTL delay time at output. LM-317 (Texas Instruments) was selected as our main regulator due to it can provide an adjustable output voltage range from 1.25 V to 37 V. Since our desired maximum output was set to +2.2 V, there is a wide range of input voltage tolerance because of its input-to-output

differential voltage can be up to 40 V. In Figure 9, R1 and R2 was selected as 466 Ω fixed resistor and a 10 kΩ variable resistor, respectively. A +2.2 V output signal can be generated by tuning the variable resistor while input DC is powered by a +9 V battery. Both input and output terminals were parallel with a capacitor to reduce ripples. An octal buffers and line drivers (SN74LS245, TI) was used to improve the performance of the receiver. The device was chosen because it can drive terminated lines down to 133 Ω and the input tolerance was compatible with +2.2 V logic inputs which just meets our requirements. Finally, all acquired signal reconstruction and analyses were performed by using Matlab.

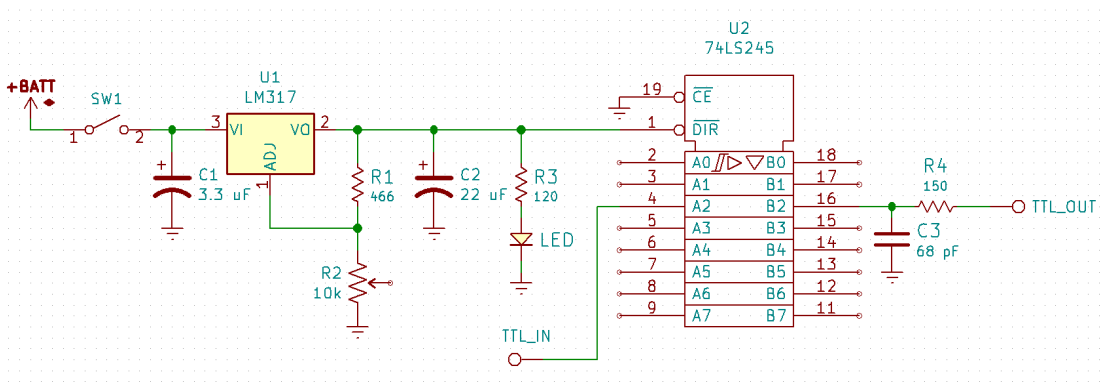

Figure 9. The buffer circuit diagram for trigger input of the Ultraview digitizer.

III.3 Simulations and experiment results

Simulated and experimental results of the reconfigurable RF filtering front-end are presented in this section. Performance of the digitizer is discussed to verify its internal bandwidth. Moreover, fully sampling with mix down stages was applied to compare with

undersampling between the Varian system and the digitizer. Lastly, ^{1}H and ^{23}Na MRSs were acquired and compared by using the QWTL front-end and commercial diplexers.

III.3.1 Performance of the Ultraview digitizer

The digitizer we were using in the simultaneous acquisition is Ultraview AD16-250. From product specification, it has an input bandwidth from DC to 700 Mhz. However, the maximum sampling rate of the digitizer is 250 MSPS. This means noise from 125 Mhz to 700 Mhz will fold back into a lower band region when using a maximum sampling rate. Ideally, noise increases in a ratio of square root of 2 when noise region folds once. So more folding times results in a higher noise level. Typically, a digitizer with internal filters can eliminate this noise from aliasing down to baseband. But the Ultraview ADC seems to not have this feature. To verify the internal filtering function, measurements were employed by acquiring noise level using different sample rates.

Noise was acquired by terminating a 50 Ω load to an input of the digitizer (with anti-aliasing filter). Different sampling rate of 80, 120, 160, 200 and 240 MSPS were used for noise acquisition. A noise region was chosen with a bandwidth of 20 Khz centered at 30.7 Mhz (^{2}H Larmor frequency at 4.7 T) so that the lowest sampling rate was able to fully sample at desired frequency band. The number of folds can be calculated by using each of the sampling rates shown in Figure 10. The horizontal axis is frequency where Fs is the designated sampling rate. The point where the vertical blue dash line intersected with the horizontal axis is a frequency region where the noise is observed at baseband. Blue points along with the blue dashed line represent the number of folds while using different sampling rates. In Figure 10, there are five blue points except for frequency under Fs/2.

This tells us noise will be added up to 6 times presented in baseband frequency region. In other words, noise level will increase by a factor of square root of 6 when compared to fully sample without undersampling.

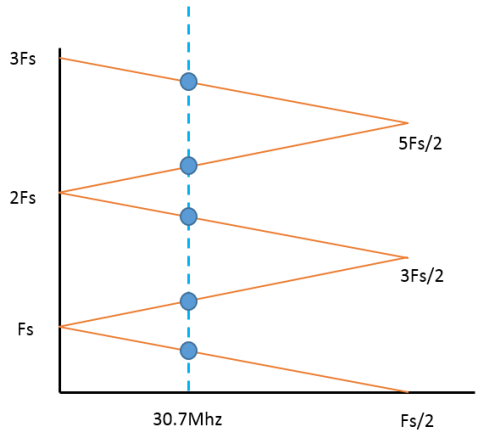

Figure 10. Relationship between aliasing folds with a given sample rate.

Let us assume the Ultraview ADC does not have built-in filters to get rid of out of band noise up to 700 Hz. There will be 17, 11, 8, 6 and 5 folds when sampling rates are 80, 120, 160, 200 and 240 MSPS, respectively. Table 2 shows that the total number folds of noise being added up within Nyquist region at different sampling rate.

Table 2. Number of folds added to Nyquist region at different sampling rates.

Number of folds	Sampling rate (Mhz)
17	80
11	120
8	160
6	200
5	240

As mentioned previously, the observed center frequency at baseband for noise was at 30.7 Mhz. Noise level was calculated by taking standard deviation of a bandwidth of 20 Khz. According to previous assumption, noise level will be proportional to square root of number of total folds because folding once will result in noise level being added twice. Thus, theoretical value can be calculated based on the assumption and compared to the measurements shown in Figure 11. In Figure 11, normalized noise level was used so that there is no need to convert the FFT amplitude when using different sampling rates. The red curve is the actual measured data and the blue dash curve is the theoretical data. It is obvious that two curves are matched to each other and the difference is less than 10 %. The results show us that the Ultraview digitizer does not provide a proper internal filtering when using different sampling rates. Out of band noise (in the digitizer) up to 700 Mhz will be aliased down to baseband even though an external analog bandpass filter is applied at the input of the digitizer.

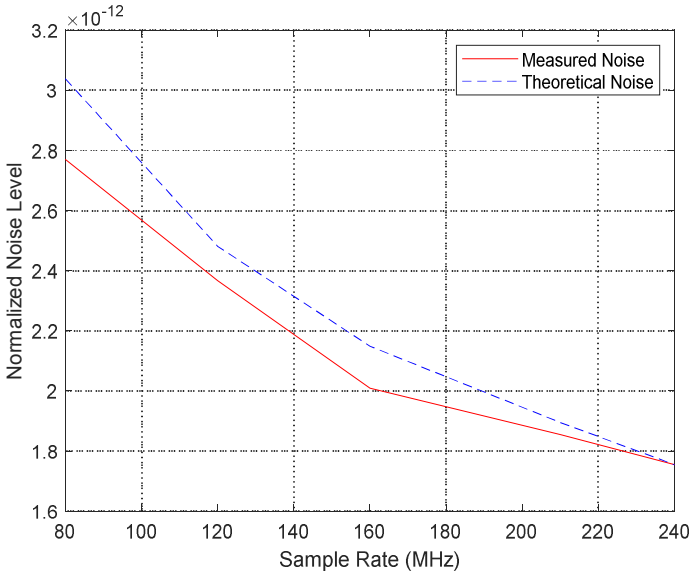

Figure 11. Measured and theoretical normalized noise level acquired by the Ultraview digitizer with input terminating with a 50 Ω load and an anti-aliasing filter at different sampling rates.

III.3.2 Fully sampling versus undersampling

The QWTL diplexer was designed and simulated with 2016 Advanced Design System (ADS) and bench measurements were taken with a HP 4195A vector network analyzer (Keysight Technologies, Inc., CA). Both ^{1}H and ^{23}Na MRS were performed with a 4.7 T Varian Unity Inova scanner in TAMU MRSL. A commercial 6 cm birdcage coil from Varian was used for ^{1}H acquisition, and a custom built eight-turn solenoid coil with a diameter of 1.5 cm was tuned to the ^{23}Na Larmor frequency and placed inside of the birdcage coil shown in Figure 12. A 5 ml tube filled with 0.6 % NaCl in water was selected as a reference phantom for two nuclei and positioned inside of loop coil. A pulse and acquire pulse sequence was used for spin excitation with 0.2 sec acquisition time, 100

KHz spectral width, and 1 sec TR. The pulse sequence was generated from the Varian for the experiments. Both ^{1}H and ^{23}Na MRSs were acquired by using the Varian which digitizes signal with a fully sampling rate at baseband and the Ultraview which digitizes signal with undersampling technique. Two MRS SNR results are shown in Table 3. ^{23}Na SNR are found to be similar between the two configurations. ^{1}H SNR obtained by the Ultraview is somewhat smaller than acquired by the Varian. This appears to be due to some out of band noise is added after the filtering. If the signal noise level is too small, the noise may be affected by the aliased noise from higher frequencies as describing in section III.3.1 in the Ultraview.

Figure 12. A 6 cm birdcage coil used for ^{1}H acquisition (left). An eight-turn solenoid coil with a diameter of 1.5 cm was used for ^{23}Na acquisition placed inside of the birdcage coil (right). A 5 ml tube filled with 0.6 % NaCl solution was used as a reference phantom.

Table 3. ^{1}H and ^{23}Na SNR comparison between the Varian and the Ultraview digitizer. "Modified with permission from [52]"

	Varian	Ultraview
^{1}H-SNR	1382	1098
^{23}Na-SNR	131	137

III.3.3 ^{1}H/^{23}Na MRS comparison between the QWTL diplexer and the commercial diplexer before signal combiner

Figure 13 shows the simulation of S-parameter plots from 2016 ADS and measurement results for both the QWTL diplexer and the commercial diplexer (Comet CF-530, NCG Companies Inc., Chino, CA) at two desired frequencies. Port 1 is the input of the QWTL diplexer shown as J1 port in Figure 7. Port 2 and port 3 are the outputs of the bandpass filters for subband 1 and subband 2, respectively. The third port will be terminated with a matched load while measuring forward transmission between the other two ports. From Figure 13 (A), it can be seen that the simulated return loss can reach 20 dB at both ^{1}H and ^{23}Na frequencies. The measured results present a lower return loss at ^{1}H frequency, however, the overall measured data have a much smooth and wider bandwidth around two frequencies among three curves. Isolation between two subband outputs are also simulated and measured, performed in Figure 13 (B). It is obvious that there are two passbands between two ports from simulated curve. This may be due to that the filter response is not specified so precisely and is regarded as an ideal filter. Nonetheless, overall simulated S_{23} presents at a reasonable magnitude of at least 80 dB which is similar to both the QWTL diplexer and the commercial diplexer, giving out a

good isolation between two subband outputs. From Figure 13 (C) and Figure 13 (D), we can observe that both the simulated and measured results presenting that two subband channels are able to provide blocking on neighboring band signals. It seems to have a higher power transmission in out-of-bands regions in both simulated S_{21} and S_{31} plots. This may be due to some limitations existing in the simulation, i.e. BNC connectors are not taken into consideration and the filter response parameters are not precisely defined presenting that two subband channels perform the blocking neighboring band signals not quite well as the experiment results. Nonetheless, both plots show that a high agreement between the QWTL diplexer and the commercial diplexer with S_{21} of 2 dB and S_{31} of 5 dB, caused by the insertion loss of two bandpass filters.

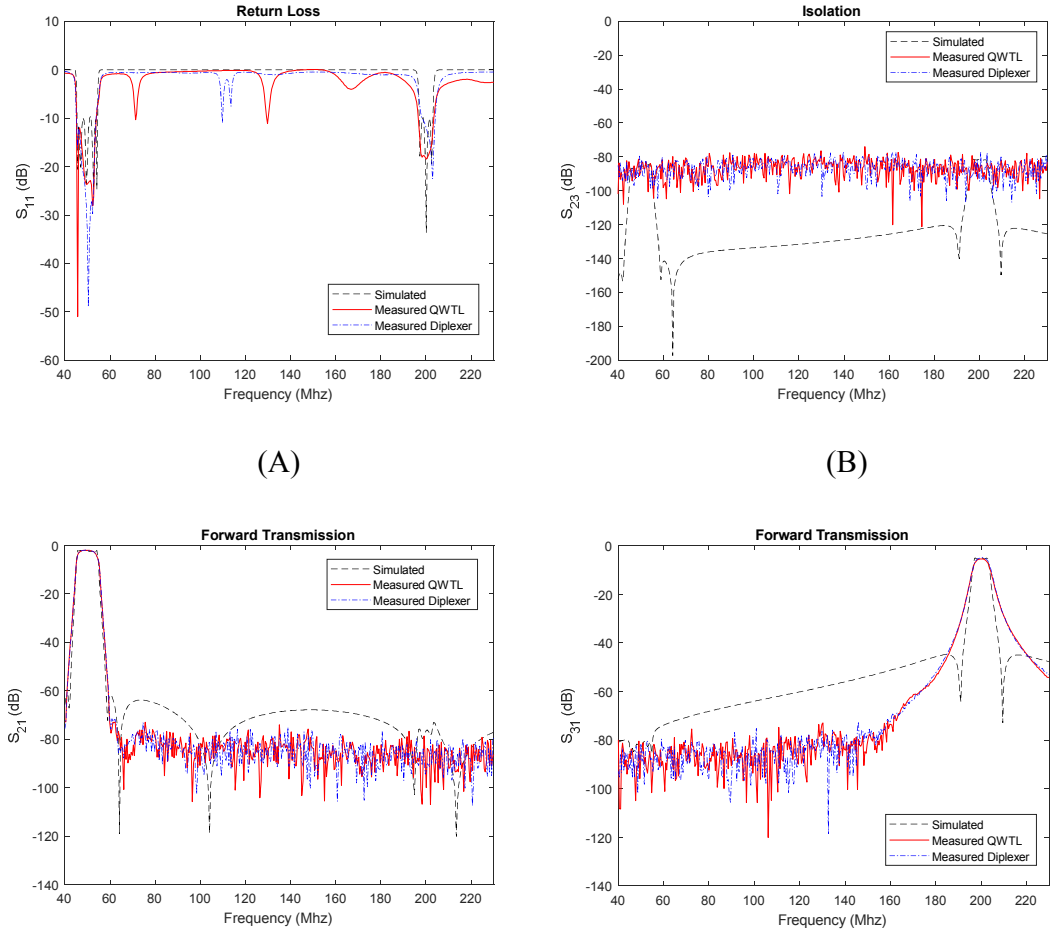

Figure 13. Simulated S-parameter plots and measurements for the QWTL diplexer and a commercial diplexer (Comet CF-530) with bandpass filters. Port 1 is the input signal, and port 2 and port 3 are the two outputs of two desired signal paths respectively for two configurations. (A) S11 return loss in dB at input Port 1, (B) S_{23} isolation in dB between two outputs, (C) S_{21} forward transmission in dB (subband 1), and (D) S_{31} forward transmission in dB (subband 2). "Modified with permission from [52]."

Bench results show that the QWTL diplexer and the commercial diplexer have a similar performance. MRS for both subbands were further measured to verify the capability between two configurations. Each desired signal was transmitted and received

through a separate single coil. Both signals were obtained before the signal combiner with one signal acquisition at a time. A single transient was used for ^{1}H-MRS data acquisition with spectral width of 100 kHz, recycle delay of 1 sec, pulse power of 36 dB, pulse width of 104 us (90 tip angle), and acquisition time of 0.2 sec. ^{1}H spectra were acquired and normalized to its peak value shown in Figure 14 for both the QWTL diplexer (red line) and the commercial diplexer (blue line). From Figure 14 (A), it can be seen that ^{1}H signal-to-noise ratio (SNR) of the QWTL diplexer is 1098 which is close to SNR of the commercial diplexer, 1087. Similarly, Figure 14 (B) shows the normalized ^{23}Na-MRS results. All parameters were the same with ^{1}H-MRS setup except pulse width set to 34 us (90 tip angle). In order to have a better observation on ^{23}Na spectra, 10 Hz line broadening was applied before Fourier Transform to reduce noise level. MR spectroscopy SNR in this dissertation is calculated by dividing spectrum peak signal to a standard deviation of a noise region. It can be seen that the QWTL diplexer can achieve a SNR of 130 whereas the commercial diplexer has a SNR of 135. Both ^{1}H and ^{23}Na MRS show that the QWTL diplexer can perform as well as the commercial diplexer before the signal combiner.

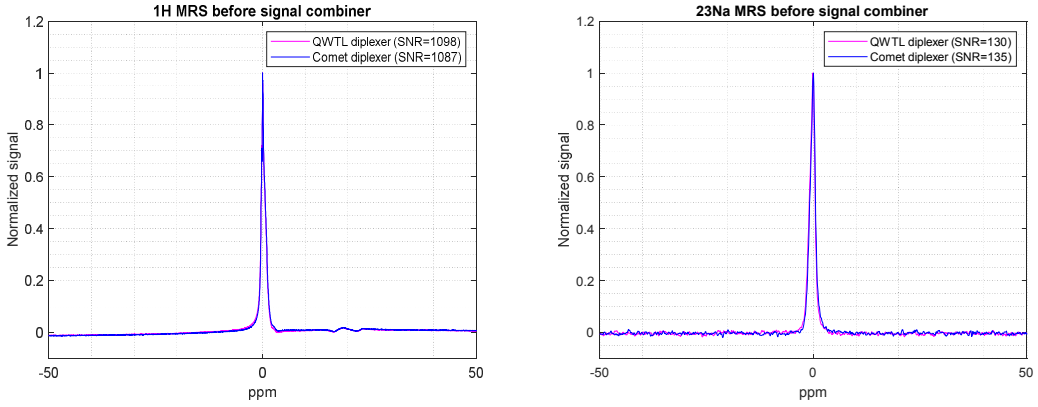

(A) (B)

Figure 14. MRS for the QWTL diplexer and the commercial diplexer before the signal combiner. Spectra are normalized to its peak. A single transient was acquired and the spectral width was 100 kHz. 10 Hz line broadening was used for ^{23}Na. Horizontal axis only displays ±50 ppm range. (A) ^{1}H-MRS SNR of the QWTL diplexer is 1098 and SNR of the commercial diplexer is 1087. (B) ^{23}Na-MRS SNR of the QWTL diplexer is 130 and SNR of the commercial diplexer is 135. "Modified with permission from [52]."

III.3.4 ^{1}H/^{23}Na MRS comparison between the QWTL diplexer and the commercial diplexer after signal combiner

Forward transmission was measured on the bench between the input of the QWTL diplexer and the output of the signal combiner shown in Figure 15. Out of band frequencies were blocked as expected and passbands occurred at 50 MHz and 200 MHz with a 3dB bandwidth of 9 MHz and 7 MHz respectively. Both the QWTL diplexer and the commercial diplexer show that the insertion loss is mainly determined by the bandpass filters. The combiner provided an additional 5.5 dB of loss at 50 Mhz and this loss can be compensated by increasing gain stage controlled by the Op Amp if it is necessary. In our experiments, as the input noise was dominated by the coil prior to low-noise amplification

stage and overall NF is dominated by the first stage preamplifier, SNR will not change even adding additional gain. ^{1}H-MRS and ^{23}Na-MRS were obtained after the signal combiner for both the QWTL diplexer (red line) and the commercial diplexer (blue line) shown in Figure 16 with the same parameter settings as well as when signals were obtained before the signal combiner. With the signal combiner, ^{1}H SNR of the QWTL diplexer is 1041 and SNR of the commercial diplexer is 1059. Similarly, ^{23}Na SNR of the QWTL diplexer is 125 whereas SNR of the commercial diplexer is 119. We can notice that the ^{1}H and ^{23}Na SNR are almost the same before and after the signal combiner for both the QWTL diplexer and the commercial diplexer.

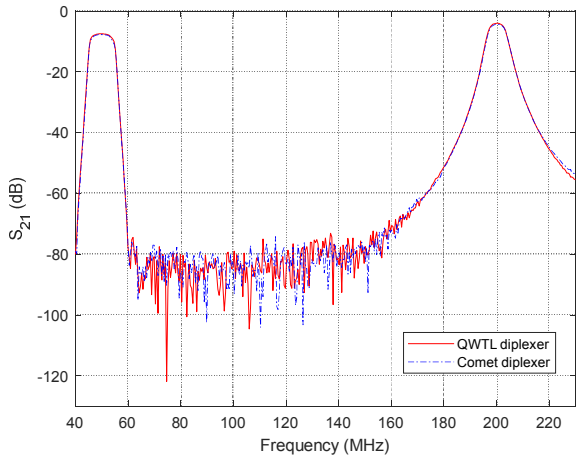

Figure 15. Measured forward transmission after the signal combiner with the QWTL diplexer filtering structure and the commercial diplexer filtering structure. Two desired passbands are occurred at 50 Mhz and 200 Mhz, respectively. "Modified with permission from [52]."

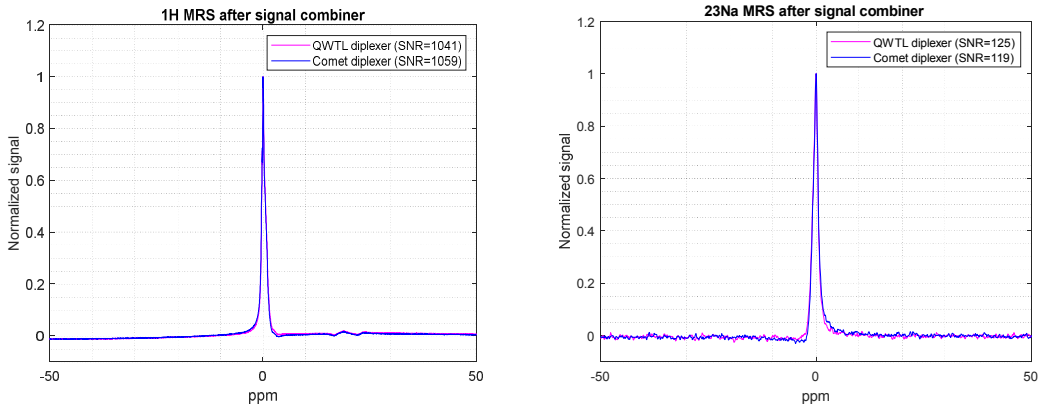

(A) (B)

Figure 16. MRSs for the QWTL diplexer and the commercial diplexer after the signal combiner. Spectra are normalized to its peak. A single transient was acquired and the spectral width was 100 kHz. 10 Hz line broadening was used for ^{23}Na. Horizontal axis only displays ±50 ppm range. (A) ^{1}H-MRS SNR of the QWTL diplexer is 1041 and SNR of the commercial diplexer is 1059. (B) ^{23}Na-MRS SNR of the QWTL diplexer is 125 and SNR of the commercial diplexer is 119. "Modified with permission from [52]."

III.4 Discussion and conclusion

A good agreement on S-parameter plots can be seen between the simulation and measurements in Figure 13 for both the QWTL diplexer and the commercial diplexer with bandpass filters. Even though there are unwanted signal bands existed, presenting a higher transmit power in forward transmission simulation. This may be due to that the simulation for the proposed QWTL diplexer are assumed to be an ideal transmission line in the ADS software. Thus, simulated electrical length may not correspond to real cables and does not take cable loss into consideration.

Comparison of ^{1}H SNR between the Ultraview and the Varian show that undersampling the received signal performs only slightly worse than mixing to baseband

and fully sampling. This may due to out of band noise was added after analog filtering described in section III.3.1. However, ^{23}Na SNR acquired from two structures present very small difference. The SNR is not lower than mixing down to baseband with the proposed structure. Additionally, the proposed filtering design allows researchers to acquire data with a lower sampling rate to reduce data throughput and processing requirements. For example, ^{1}H data acquired at 4.7 T using a 230 MHz sampling rate produces 40 percent less data than sampling at the Nyquist rate. All in all, the overall ^{1}H and ^{23}Na SNR results show high correspondence between the proposed QWTL diplexer and the commercial diplexer, demonstrating that the QWTL diplexer has similar performance as the commercial diplexers both before and after the signal combiner. The significance of this is that the proposed QWTL filtering structure can be easily tuned to other bands of interested nuclei by swapping to corresponding quarter-wavelength transmission line cables and filters. Transferring the design to more than two nuclei is also simple by adding more sections of QWTLs which will be discussed in the next chapter.

CHAPTER IV

SIMULTANEOUS MULTINUCLEAR MRI/MRS FRONT-END FOR THREE NUCLEI

IV.1 Introduction

There has been a great deal of work to develop a broadband system to acquire multiple nuclei simultaneously due to the potential to detect more information in a one-time scan. In addition, simultaneous acquisition not only allows us to gather more metabolites in a single scan but also with less acquisition time. This can directly reduce the limitation on the number of observations for different nuclei in a given fixed time in hyperpolarized application. However, most *in vivo* commercial multinuclear MR scanners only involve a series of single-nuclear acquisitions. Even simultaneous function can be achieved by modifying existing MR scanners, it is still limited to dual nuclei till today [7, 16].

In this chapter, a reconfigurable broadband front-end at three nuclei will be introduced and is extended from Chapter III. This front-end filtering configuration allows us to split the incoming broadband signal for narrow band filtering as well as providing separate gain controls at each signal path. In order to acquire three nuclei NMR signal, a triple-tuned coil geometry was designed by a former student with different matching and tuning networks [57]. One was tuned at $^{1}H/^{23}Na/^{2}H$ (Coil 1) while the other one was tuned at $^{1}H/^{13}C/^{15}N$ (Coil 2). The reason to build the system fitting ^{2}H and ^{23}Na frequencies is that these two nuclei have stronger signal sensitivity and samples are easy to acquire. Additionally, ^{2}H and ^{23}Na have very close Larmor frequencies when compared to ^{15}N and

^{13}C, respectively. This can reduce the experiment difficulty in the early stage while acquiring signals. In fact, a triple-tuned coil can either be multiple single frequency coils or a single port triple nuclei coil. In our experiments, we proposed a single port triple-tuned coil because it presents less complexity and requires less space when compared to a set of coils separately. In chapter III, we have introduced the design and the performance of the reconfigurable RF filtering front-end at dual nuclei [52]. The flexible front-end is expanded in this chapter to a QWTL triplexer which can be used to separate an incoming broadband signal into three narrow bands for filtering.

In order to utilize only one input channel of a digitizer, a three-port signal combiner was designed based on section III.2.3 to combine three filtered bands into one output port before digitization. Therefore, other channels can remain available for other applications such as a multiband coil array. Furthermore, direct sampling one broadband signal also produces less data throughput when compared to digitize multiple nuclei signals separately. Here, two MRSs ($^{1}H/^{23}Na/^{2}H$ and $^{1}H/^{13}C/^{15}N$) were acquired and compared between single nuclear acquisition at three frequencies using the Varian system and simultaneous acquisition using the broadband system. Among simultaneous acquisition, single channel digitization spectra were also compared with three channel digitization without combining three filtered signals, showing that one channel digitization can perform as well as three channel digitization separately but generating less data throughput. Undersampling technique was also employed to provide an additional benefit of reducing throughput load. Large signal dynamic range nuclear were also investigated in this chapter to validate the triplexer front-end's performance.

Figure 17 shows the overall simultaneous acquisition diagram with single channel digitization. While planning to acquire multiple nuclei simultaneously, all the modules of the system must be able to accommodate all desired frequencies. It is necessary to have a transmitter to generate multiple RF excitation pulses simultaneously. In addition, a broadband transmit/receive (T/R) switch is required to prevent RF power from leaking into receiver chains and damaging components such as LNAs while using a transmit and receive coil. During receive mode, an incoming broadband signal passes through a low-noise amplification stage prior to channelization. The QWTL triplexer was developed to segregate the signal for filtering due to undersampling. Different gain stage can be applied in an individual signal channel for those low sensitivity nuclei other than proton by adding independent attenuators. Then all filtered signals are combined back for digitization.

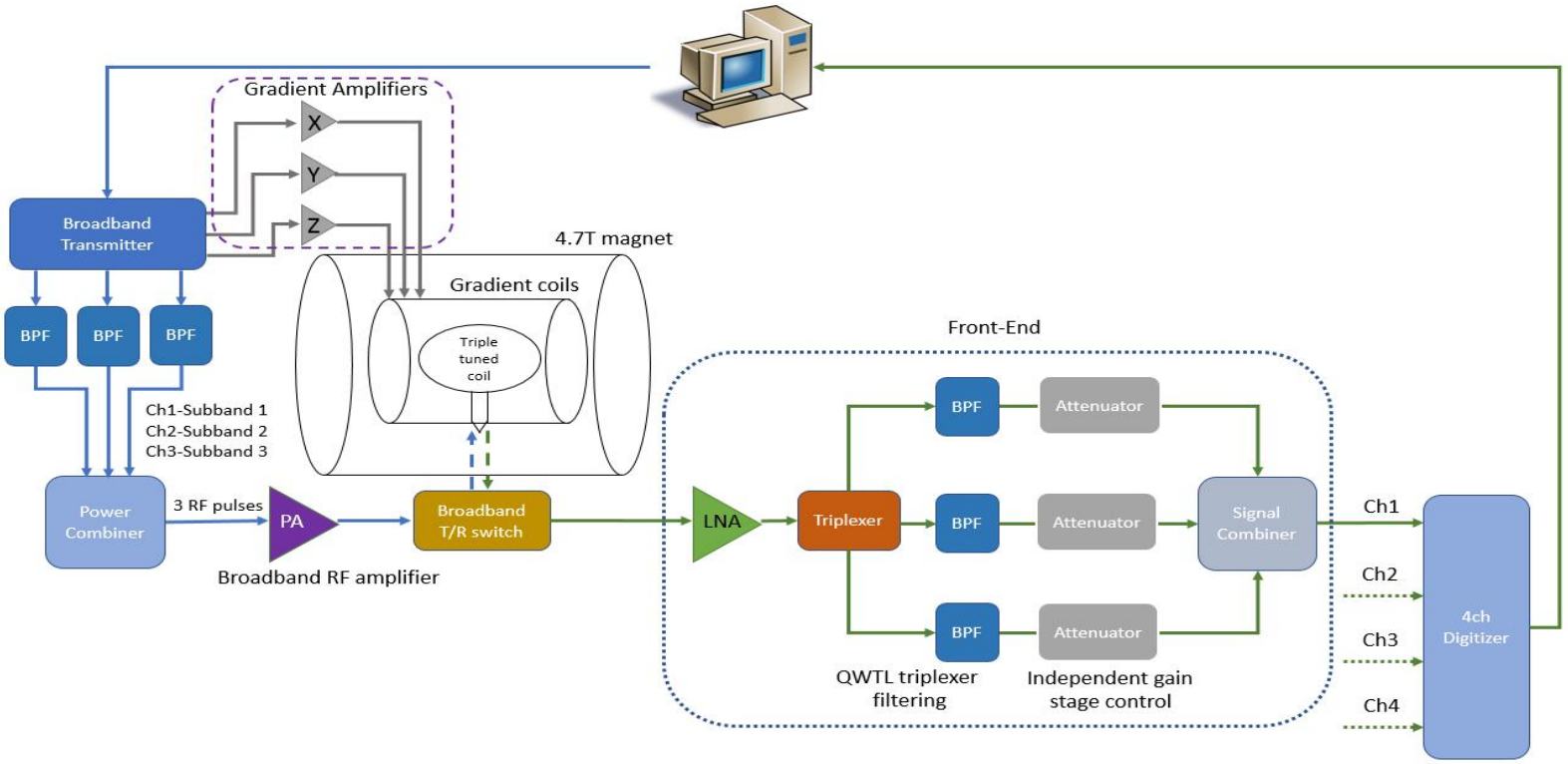

Figure 17. Block diagram of broadband system used for simultaneous multinuclear MRI/MRS. A LabVIEW console was designed by Texas A&M MRSL which is able to control the broadband transmitter to generate three different frequency RF pulses. Analog signals can be generated through the transmitter for gradients control. Three RF pulses are combined into one pulse sequence through a power combiner and being amplified for transmitting. A home-built broadband T/R switch was designed to apply with single port, triple tuned coil for simultaneous multinuclear acquisition. In receive mode, induced signal is sent to the triplexer front-end for narrow band filtering and applying different gain control at each nuclear. Finally, all optimized signals are combined back into one output channel for digitization.

IV.2 Method

The design of simultaneous multinuclear MRI and MRS front-end is discussed in this section. Simultaneous acquisition diagram consists of a broadband transmitter, a broadband Tx/Rx switch, a reconfigurable QWTL triplexer filtering, a three-port signal combiner, and data acquisition which are shown in Figure 17.

IV.2.1 Broadband transmitter

Simultaneous multinuclear acquisition in this dissertation was conducted based on a home-built broadband system [58]. The system is able to provide up to three different transmit frequencies simultaneously or in fast succession. The transmit system consists of a PCIe-6363 DAQ card (National Instruments, Austin, TX, USA) and an AD9959 DDS evaluation board (Analog Devices, Norwood, MA, USA). The PCIe-6363 provides analog outputs to control gradients as well as digital controls for the AD9959, which is used for RF pulse generation. On the receive side, a 4-channel, 16-bit, 250 MS/s/ch digitizer is used for signal acquisition (UltraView AD16-250). LabVIEW GUIs are used to control transmit and receive, and all acquired signals are reconstructed and analyzed with Matlab (Mathworks, Natick, MA). For MR imaging, a gradient echo sequence with simultaneous RF pulses is used. For MR spectroscopy, a fast succession of RF pulses is sent with a pulse and acquire sequence. The physical hardware is shown in Figure 18 (A). Previously, MRSL has developed and demonstrated a dual nuclei control program [58]. Here, we expand the program and are able to specify at most three different frequencies with a customized timing. Figure 18 (B) is used to generate three RFs simultaneously for the

MRI experiments whereas Figure 18 (C) is used to generate a fast succession of three RFs for the MRS experiments.

(A)

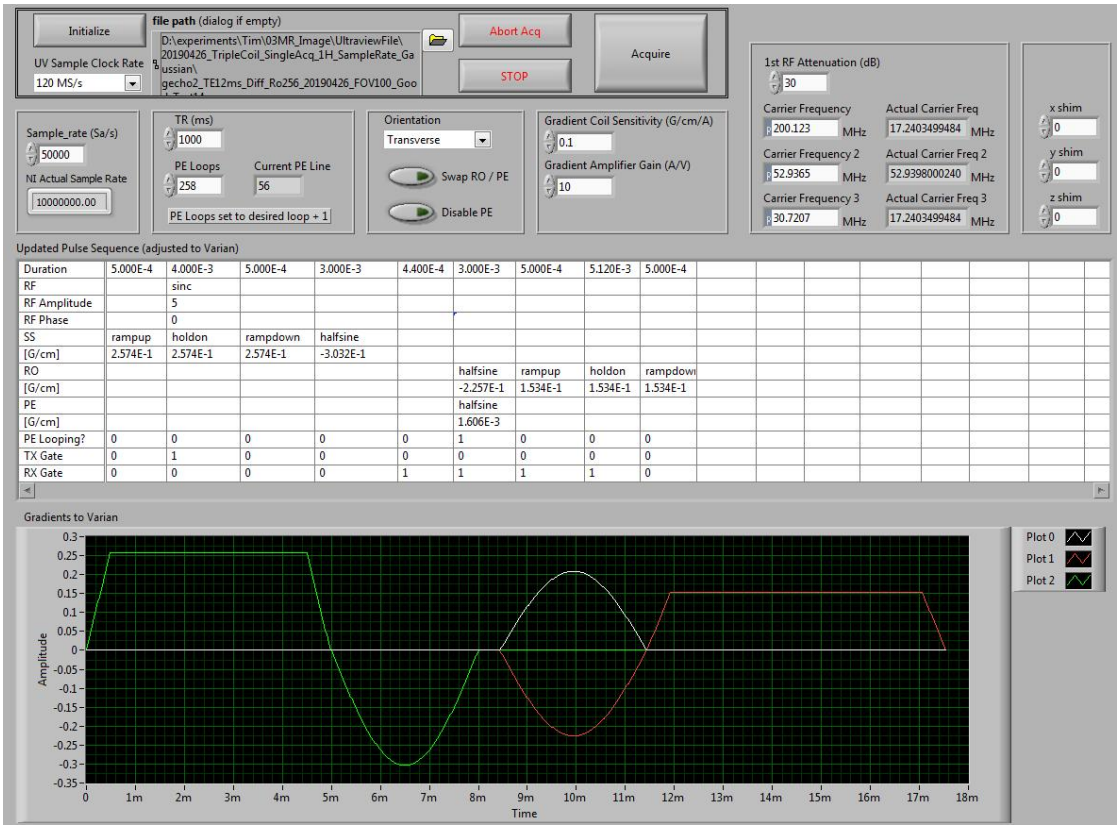

Duration	5.000E-4	4.000E-3	5.000E-4	3.000E-3	4.400E-4	3.000E-3	5.000E-4	5.120E-3	5.000E-4
RF		sinc							
RF Amplitude		5							
RF Phase		0							
SS	rampup	holdon	rampdown	halfsine					
[G/cm]	2.574E-1	2.574E-1	2.574E-1	-3.032E-1					
RO						halfsine	rampup	holdon	rampdow
[G/cm]						-2.257E-1	1.534E-1	1.534E-1	1.534E-1
PE						halfsine			
[G/cm]						1.606E-3			
PE Looping?	0	0	0	0	0	1	0	0	0
TX Gate	0	1	0	0	0	0	0	0	0
RX Gate	0	0	0	0	1	1	1	1	0

(B)

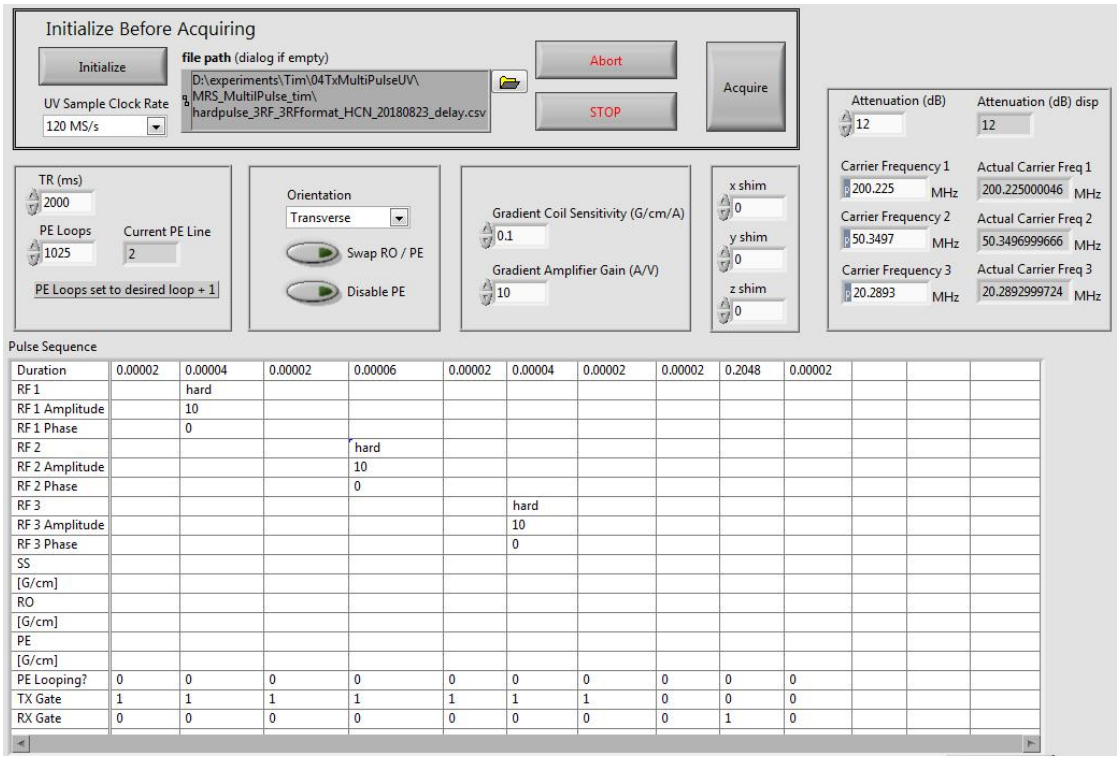

Duration	0.00002	0.00004	0.00002	0.00006	0.00002	0.00004	0.00002	0.00002	0.2048	0.00002
RF 1		hard								
RF 1 Amplitude		10								
RF 1 Phase		0								
RF 2				hard						
RF 2 Amplitude				10						
RF 2 Phase				0						
RF 3						hard				
RF 3 Amplitude						10				
RF 3 Phase						0				
SS										
[G/cm]										
RO										
[G/cm]										
PE										
[G/cm]										
PE Looping?	0	0	0	0	0	0	0	0	0	0
TX Gate	1	1	1	1	1	1	1	0	0	0
RX Gate	0	0	0	0	0	0	0	0	1	0

(C)

Figure 18. (A) The broadband transmitter which is capable of generating at most up to three RF frequencies signals. (B) The LabVIEW GUI used to generate three RFs simultaneously for MRI experiments. (C) The LabVIEW GUI used to generate three fast succession RFs for MRS experiments.

Due to three frequencies were generated at each of AD9959 channels separately, a broadband signal combiner (ZFSC-4-1-S+, Mini-Circuits, NY) was used to combine three frequencies into one output channel and sent to the RF power amplifier (AMT-3200, Herley Industries, PA). A GRE sequence was applied for both simultaneous and single frequency MRI at $^{1}H/^{23}Na/^{2}H$ shown in Figure 19 (A). Three RF pulses were sent simultaneously for simultaneous multinuclear acquisition where single nuclear excitation was sent individually but with same pulse width. Pulse and acquire pulse sequences were

employed for MRS acquisition which are shown in Figure 19 (B) and Figure 19 (C). Each top sequence is for simultaneous acquisition with the broadband transmitter whereas below sequence is for single nuclear acquisition with the Varian system. Three RF hard pulses are sent in a fast succession in an order according to signal sensitivity from high to low. However, in the $^{1}H/^{23}Na/^{2}H$ experiment, ^{2}H pulse was placed before ^{1}H due to deuterium sample volume was at least 5 times larger than water sample and the concentration is 99.9 %. This brings a larger SNR for deuterium rather than proton. Pulse width of each nuclear was calibrated to have 90˚ flip angle which are 500 us, 60 us, and 180 us at ^{2}H, ^{1}H, and ^{23}Na whereas 40 us, 60 us, and 40 us at ^{1}H, ^{13}C, and ^{15}N, respectively. Each RF pulse was separated by 20 us to prevent RF amplifier from saturation. Acquisition rising window was also delayed by 80 us and 20 us from RF pulses for two configurations, $^{1}H/^{23}Na/^{2}H$ and $^{1}H/^{13}C/^{15}N$ respectively, to avoid RF ringdown effect. The delay time between RF pulse and receive rising gate were same for both simultaneous acquisition and single frequency acquisition at each nuclear.

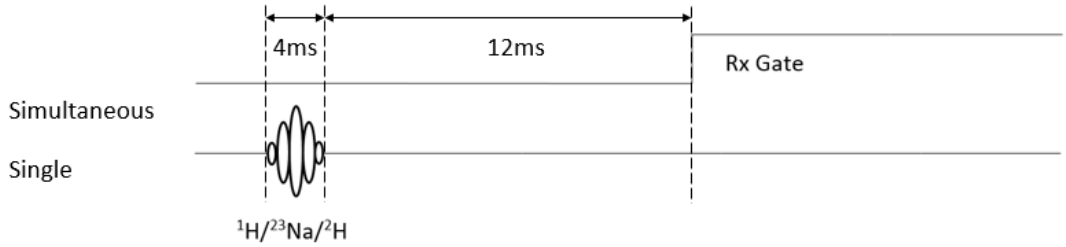

(A)

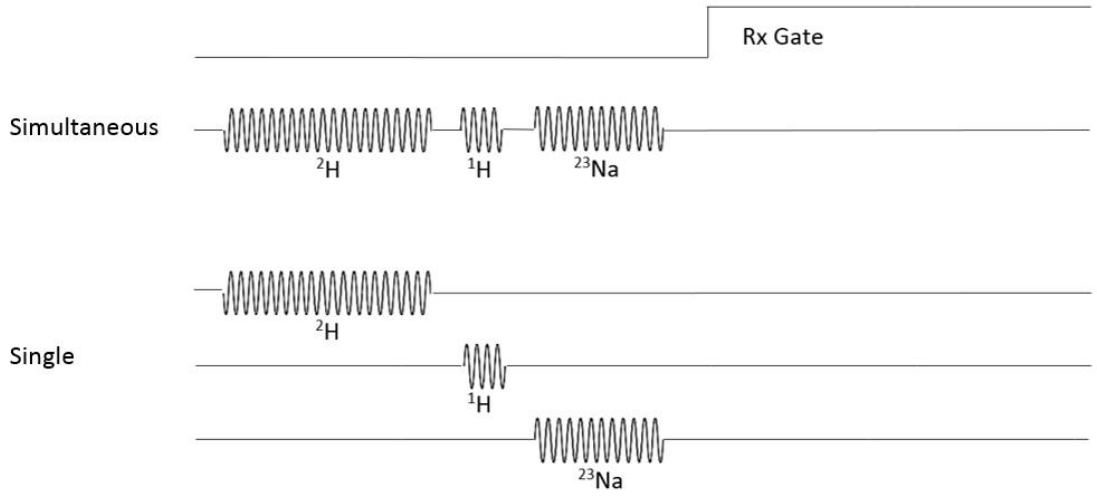

(B)

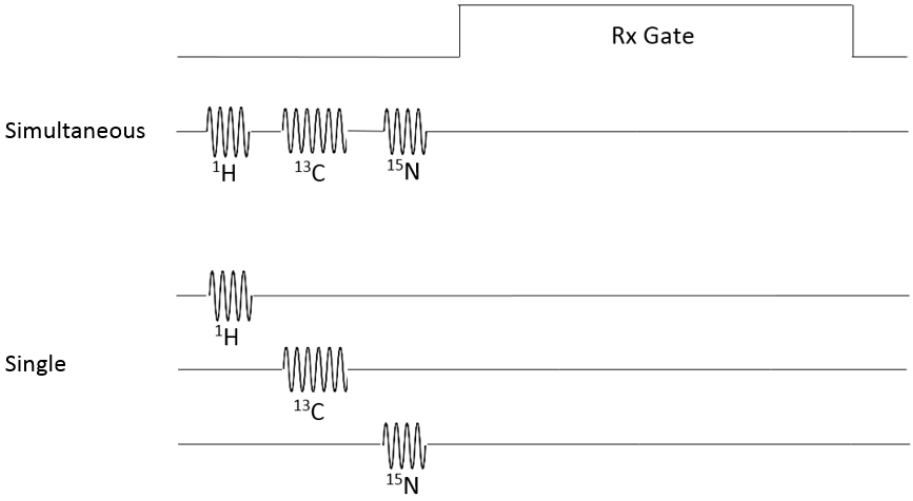

(C)

Figure 19. Pulse sequences for both the broadband system (simultaneous acquisition) and the Varian system (single frequency acquisition). (A) $^{1}H/^{23}Na/^{2}H$ and $^{1}H/^{15}N/^{13}C$ MRI acquisition with RF pulses sent simultaneously. (B) $^{1}H/^{23}Na/^{2}H$ MRS acquisition, and (C) $^{1}H/^{15}N/^{13}C$ MRS acquisition with a fast succession RF pulses.

IV.2.2 Broadband Tx/Rx switch

The broadband Tx/Rx switch was designed with KiCad (2017-11-24 Version) shown in Figure 20 (A) and physical hardware photograph is shown in Figure 20 (B). The TR switch consisted of PIN diodes, DC block capacitors, RF chokes and DC bias current limiter resistors. When DC bias 1 (J4) applied +5V, the PIN diode (MA4P7446F-1091T, Macom) at transmit side (D1) would be forward biased and the transmit RF signal was directed from transmit port (J1) to the coil (J2). At the same time, DC bias 2 (J5) applied -48V to confirm PIN diode at receive side (D2) was reverse biased to prevent transmit RF signal from leaking into receiver path. Similarly, when receiving the RF signal, DC bias 2 provided +5V while DC bias 1 applied -48V, the PIN diode at receive side was forward biased and the diode at transmit side was reverse biased. Induced RF signal was passed from the coil (J2) to receive port (J3). An additional PIN diode (D3) and two Schottky diodes (D4 and D5, MMBD701LT1G, ON Semiconductor) were added to protect the LNA as an additional protection. The shunt inverse direction Schottky diodes were used to prevent RF signal passing through while the RF amplitude was greater than its forward conducting voltage if the PIN diodes (D1 and D2) did not work properly. Since the conducting voltage value could be larger if the pulse width was narrow, hence another PIN diode (D3) was added to direct the leaking signal into ground while in transmit mode to better protect the LNA from breaking through. To this point, the conducting time of this PIN diode should be the same as the one at transmit side. Thus, two PIN diodes, D1 and D3 shared a same DC bias voltage (DC bias 1).

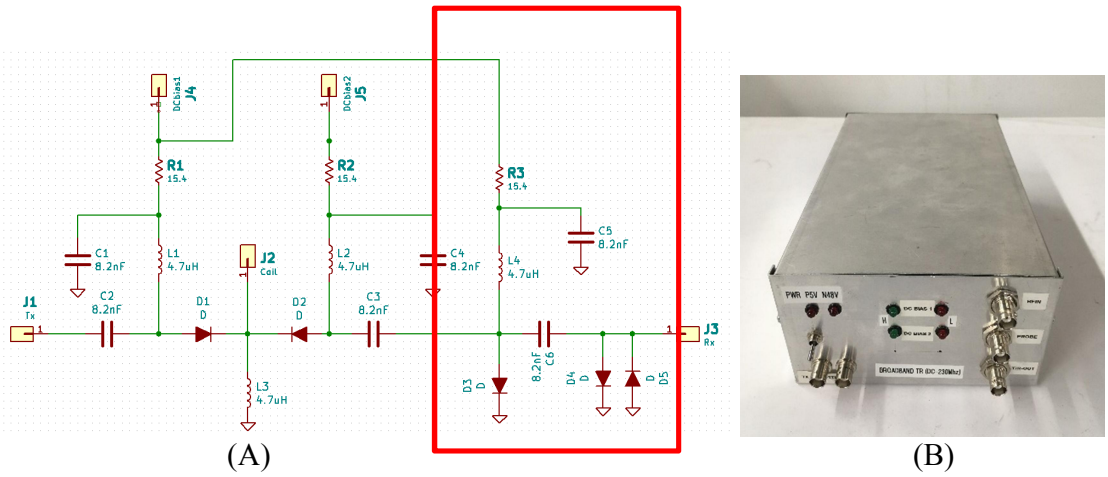

Figure 20. The broadband Tx/Rx switch uses PIN diodes to control transmit and receive mode. (A) Circuit diagram and (B) physical hardware photograph.

The PIN diodes used in the broadband Tx/Rx switch must have a fast switching time, low capacitance, and low impedance. Additionally, the broadband Tx/Rx switch was designed to handle a maximum transmit power up to 500 W. This means the input RF signal peak-to-peak voltage can be up to 447 V in a 50 Ω system. With such high RF input voltage, the reverse DC voltage of PIN diodes must take into consideration to prevent the diode from breakdown. Therefore, surface mountable PIN diodes in Metal Electrode Leadless Faced (MELF) package were used in our design.

The DC block capacitors were designed to prevent DC signal from leaking into transmit and receive ports and allowed RF signals to pass through. On the other hand, the RF chokes were designed to block RF signal and prevented RF signal from going into DC bias circuit. In general, the reactance of capacitors needed to be as low as 1 or 2 Ω and inductors had to be as high as over 500 Ω where the reactance of capacitor and inductor are dependent on the operating frequency shown as $X_c = {}^{1}/_{\omega_c}$ and $X_L = \omega_L$, respectively.

Since the Tx/Rx switch was designed for broadband use, the reactance was calculated based on the lowest operating frequency. In our case, ^{15}N has a lowest Larmor frequency of 20.289 Mhz among all targeted nuclei when main magnetic field is 4.7 T. The capacitor value was selected as 8.2 nF (C1206C822KDR, Vishay) and the inductor value was chosen to be 4.7 uH (BRC2012T4R7MD, Taiyo Yuden). One thing has to be noticed that the self-resonance frequency of both components has to be greater than our maximum operating frequency to avoid blocking RF signals.

The PIN diodes have a maximum forward conducting current of 500 mA. However, the PIN diodes will be fully conducted and present a low resistance when the forward conducting current reaches 100 mA or more. Thus, a forward conducting current of 150 mA was designed for the PIN diodes. Current limiters are based on the resistors placed in series of two DC bias inputs. While calculating the forward conducting current of the PIN diodes, impedance of inductors, PIN diodes, series resistors and previous stage PIN diode driver series resistance, must be taken into consideration. Thus, a 15.4 Ω resistor (ERJ-P08F15R4V, Panasonic) was chosen to present a conducting current of 150 mA when the diodes were forward biased. All PIN diode driver circuits are integrated into the Tx/Rx switch shown in Figure 20 (B). The driver takes a +5V TTL signal from the front panel and provides +5V when the TTL signal is high and -48V when the TTL signal is low for both DC bias feedings. The front panel has the ability to display both bias voltage outputs with green LEDs (+5V) and red LEDs (-48V) instantly to monitor its output function.

IV.2.3 Reconfigurable QWTL triplexer filtering

In chapter III, we have demonstrated an RF front-end for two nuclei, ^{1}H and ^{23}Na, that provides separate filtering and independent gain control with very flexible transmission line cables intended for undersampling [52]. The diplexer front-end has proved that both proton and sodium can provide comparable results when compared to a Varian Unity Inova system.

Here, we will expand the diplexer front-end into a triplexer front-end to accommodate three different nuclei. The structure diagram and photograph are shown in Figure 21. To obtain the best SNR, the noise figure of first LNA should be as low as possible. Therefore, an LNA (AU-1647, L3 Narda-Miteq, NY, USA) with a noise figure of 1.1 dB and a gain of 58 dB was selected for our front-end. The triplexer consists of three transmission line sections, which together form three different quarter-wavelength sections at different frequencies. Due to the characteristic inverse admittance of a quarter-wavelength transmission line, an open circuit will be seen when looking into one end of the transmission line if the other end is short-circuited. For example, three transmission line sections present three different shorted quarter-wavelength transmission lines (QWTLs) points J1, J2, and J3 at three desired sub-bands, e.g. ^{15}N, ^{13}C, and ^{1}H at 20.29 MHz, 50.35 MHz, and 200.23 MHz respectively. The QWTL cable lengths can easily be adjusted to shift the frequencies to those of ^{2}H and ^{23}Na. After the incoming broadband MR signal passes through the pre-amplification stage, the QWTL triplexer is able to separate ^{15}N first at J1 and direct ^{15}N signal into sub-band 1 because ^{15}N has the longest wavelength and sees an open circuit. At J2, ^{13}C signal is led into sub-band 2 because at

that point ^{13}C sees an open circuit. Similarly, at J3, ^{1}H is directed into sub-band 3. After the quarter-wavelength structure, commercial band-pass filters are used for narrow-band filtering. In our experiment, we use 2800-SMA, 2867 (KR Electronics, Avenel, NJ, USA) and BBP-30+ (Mini-Circuits, Brooklyn, NY, USA) for $^{1}H/^{23}Na/^{2}H$. BBP-30+ is replaced with SBP-21.4+ (Mini-Circuits, Brooklyn, NY, USA) while the other two filters remain same for $^{1}H/^{13}C/^{15}N$.

In order to implement under-sampled acquisition, two QWTL triplexers ($^{1}H/^{23}Na/^{2}H$ and $^{1}H/^{13}C/^{15}N$) were designed to segregate the incoming broadband signal into three narrow bands for filtering in order to prevent out of band noise from aliasing into the same band as the signals. The combination of the quarter-wavelength transmission line triplexer and bandpass filtering allows an incoming broadband signal to be separated to filtered signal paths for each nucleus.

Because the main structure is based on multiple section transmission line cables, it is easy to switch the pass-bands by changing the length of the quarter-wavelength transmission line and exchanging filters. This provides an advantage in flexibility over commercial diplexers and triplexers where the pass-bands are not reconfigurable.

Based on the desired nuclei at 4.7 T, each nuclear Larmor frequency and corresponding parameters can be calculated shown in Table 4. Due to the velocity factor of RG58 and RG223 is 0.659, thus the real cable length (in column 4) should multiply by the loss factor to the calculated quarter-wavelength (in column 3) of each nuclear.

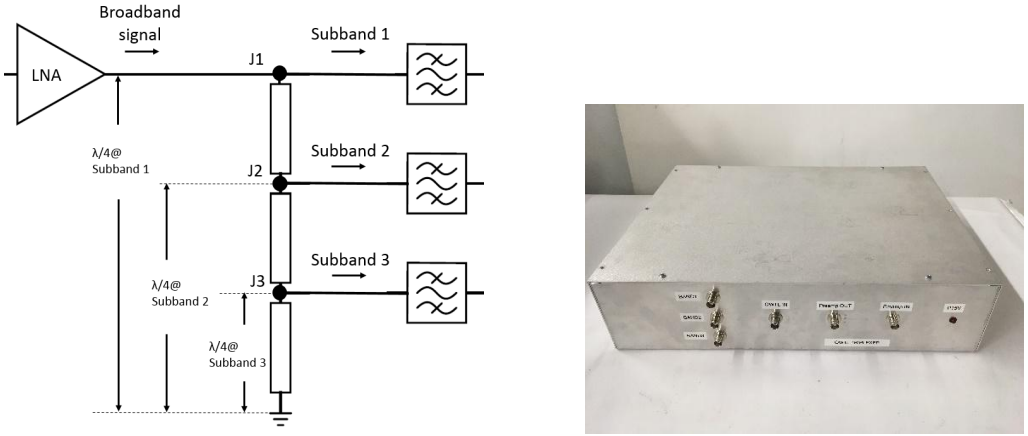

(A) (B)

Figure 21. QWTL triplexer is used to segregate a broadband incoming signal into three narrow bands for filtering. (A) configuration of the triplexer and (B) physical hardware photograph.

Table 4. Targeted nuclei Larmor frequency and corresponding quarter-wavelength values.

Nuclei	Larmor Frequency (Mhz)	Ideal QW length (cm)	Real QW length (cm)
^{1}H	200.125	37.48	24.70
^{23}Na	52.9359	141.68	93.37
^{13}C	50.3497	148.96	98.16
^{2}H	30.7207	244.14	160.89
^{15}N	20.2893	369.65	243.60

IV.2.4 Three port signal combiner

The purpose of the combiner is to combine all filtered signals into one channel. Utilizing a single input channel of the digitizer for simultaneous multinuclear acquisition can reduce raw data generated by 66% when compared to digitizing three nuclei separately. Additionally, combining the three signals leaves the other digitizer channels available for array applications.

The structure of the three-port signal combiner is mainly based on a wideband, low distortion operational amplifier (OPA843, Texas Instruments, Dallas, TX, USA) with an inverting summing amplifier circuit. The three-port signal combiner was designed through KiCad and the circuit schematic and hardware photograph are shown in Figure 22. The signal combiner consists of an op-amp, matching resistors, DC compensation resistors, and gain resistors. It can be seen that noise gain is designed to equal to 4, giving a 300 MHz bandwidth at a gain of -1 for each of sub-bands to maintain loop stability. Additionally, input termination resistors R_1, R_8 and R_{12} are added to bring the input impedance of the combiner to 50Ω. In order to keep a unity gain to all input signals of the op-amp, R_2, R_7 and R_{13} are same with R_3 where R_3 in larger values can reduce the output loading and improve harmonic distortion performance. Therefore, R_1, R_8 and R_{12} can be determined while keeping both the unity gain and input impedance matching. In our design, R_3 is designed to be 390 Ω. To achieve a gain of -1 for all inputs, R_2, R_7 and R_{13} are 390 Ω. This required R_1, R_8 and R_{12} to be 57.4 Ω to perform a 50 Ω input impedance to all signal sources where,

$$R_1 // R_2 = 50\ \Omega \tag{5}$$

$$R_8//R_7 = 50\ \Omega \tag{6}$$

$$R_{12}//R_{13} = 50\ \Omega \tag{7}$$

A shunt resistor R_4 was calculated and placed at input of noninverting port to compensate input bias current between two inputs of the Op Amp based on following equation,

$$R_4 = [(50//R_8 + R_7)//(50//R_1 + R_2)//(50//R_{12} + R_{13})]//R_3 \tag{8}$$

The circuit was fabricated on an LPKF C30 on two-layer copper-clad FR4 board.

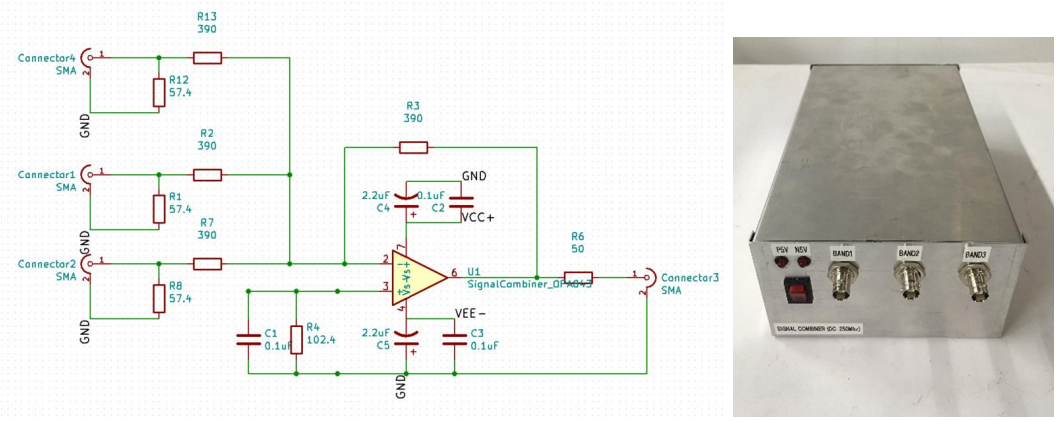

(A) (B)

Figure 22. The three-port signal combiner (A) circuit schematic and (B) hardware photograph.

IV.2.5 Phantoms

Some of nuclei have very low natural abundance in the world, e.g. ^{13}C and ^{15}N have an absolute sensitivity of 1.76×10^{-4} and 3.85×10^{-6} relative to ^{1}H, respectively. This requires a very large dynamic range digitizer to acquire those scarce X-nuclei with ^{1}H simultaneously if those signals are amplified through only one preamplifier with a

constant gain. For example, the dynamic range can be at least 108.3 dB in order to acquire both ^{1}H and ^{15}N signals. This requires at least an 18-bit digitizer to cover the signal range difference and this is still not considering ^{1}H sensitivity in the real acquisition.

Hyperpolarization can improve signal sensitivity by over 10,000 folds for those low natural abundance nuclei. This can greatly reduce dynamic range requirement of the digitizer. However, signal level difference between ^{15}N and ^{1}H can reduce down to 20.9 dB if we assume that ^{15}N sensitivity improves by a factor of 23,500. This makes it possible to obtain multiple nuclei simultaneously with a commercial 16-bit digitizer. But since the signal level between two nuclei still remains 21 dB, it is still possible that SNR is not optimized at all nuclei if the gain does not apply properly.

In order to fully investigate the front-end performance for the above two cases without applying hyperpolarization technique, enriched phantom and low concentration phantom are used to mimic hyperpolarization and naturally occurring condition, respectively.

IV.2.5.1 Enriched condition

For MR spectroscopy at $^{1}H/^{23}Na/^{2}H$, Phantom 1 was built which consists three 10 ml tubes in a Petri dish and is shown in Figure 23. Each tube was filled with different concentration sodium solution, 5.1 M, 3.8 M, and 2.6 M from left tube to right tube, respectively. Side tubes and the plate container were filled with 99.9% deuterium oxide (D, DLM-4, Cambridge Isotope Laboratories, Inc.) and the center tube was mixed with distilled water in the same amount. The reason to have water in the center tube is that ^{1}H signal goes into butterfly mode. Thus, center copper of the triple-tuned coil can have a

stronger B_1 field at ^1H frequency. The plate was also filled with deuterium oxide due to its low sensitivity. The whole phantom was positioned 1 cm away on top of the coil in order to have a better B_1 homogeneity.

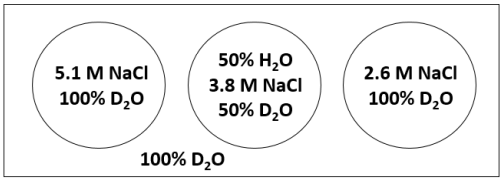

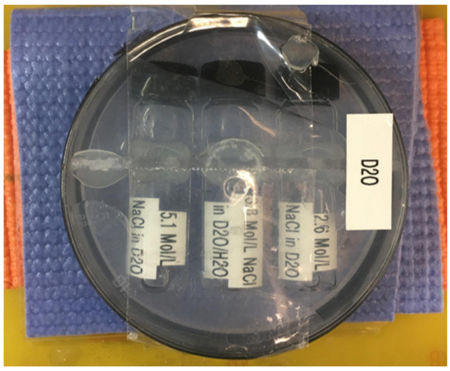

(A) (B)

Figure 23. Phantom 1 for $^1H/^{23}Na/^2H$ MRS acquisition. (A) Phantom section diagram and (B) top view photograph.

For MR imaging at $^1H/^{23}Na/^2H$, the phantom composition is slightly different from MR spectroscopy in order to observe all three nuclei image variation on all three tubes. Phantom 2 was built which consists of three 10 mL cylinder tubes in a Petri dish, shown in Figure 24. The tubes contain a mixture of water and deuterium oxide, with the ratio of H_2O:D_2O being 20:80, 90:10, and 20:80 from left to right. Sodium molar concentration is 5.37 M, 4.08 M, and 2.72 M from left to right. The area outside of tubes within the dish contains 100 % deuterium oxide. All three tubes are parallel and the center tube is aligned with the center conductor of the coil.

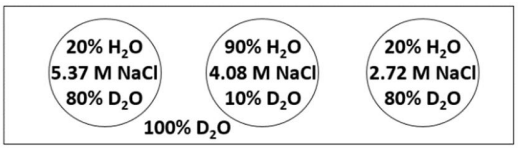

Figure 24. Phantom 2 axial diagram for $^{1}H/^{23}Na/^{2}H$ MRI acquisition.

Once the performance is confirmed at $^{1}H/^{23}Na/^{2}H$, we translate the system frequency to $^{1}H/^{13}C/^{15}N$. Due to ^{13}C and ^{15}N have very small sensitivity relative to ^{1}H [59] and the acquisition was without using hyperpolarization technique, enriched ^{13}C and ^{15}N were used in our experiments. Phantom 3 contains four separate cylinder tubes were used as shown in Figure 25. From left to right, they are 2 mL of 4.5 M ammonium chloride (NH_4Cl, ^{15}N, 98 %, NLM-467, Cambridge Isotope Laboratories, Inc.) in deuterium oxide, 10 mL of distilled water, 1 g of 99% (w/w) ^{13}C-enriched methanol, and 2 mL of 4.5 M ammonium chloride solution in deuterium oxide. Methanol and water tubes were positioned together along the center conductor of the coil. Two ammonium tubes were placed separately at each side next to methanol and water tubes, and close to the inner side of the loop conductor. All four tubes are aligned and parallel with center conductor of the coil.

In this experiment, the water tube was placed as close as to the center copper due to maximum B_1 field was produced because of butterfly mode characteristic. In general, loop mode has a better field uniformity at the center of the loop. However, magnetic field at center of loop is lower than its neighboring region due to the center conductor of the coil. Additionally, ^{15}N has relatively low sensitivity while compared to any other nuclei

here. In order to be able to acquire ^{15}N signal, two separated ammonium chloride tubes (left tube and right tube) were placed at each side close to conductor rim. Methanol tube was positioned between the water tube and one of ammonium chloride tubes. The reason to mix ammonium chloride with deuterium oxide is to remove J-coupling due to nitrogen and proton chemical pond, so that signal peak will not split into multiple peaks resulting in an inaccurate measurement while calculating SNR after applying phase correction to spectra.

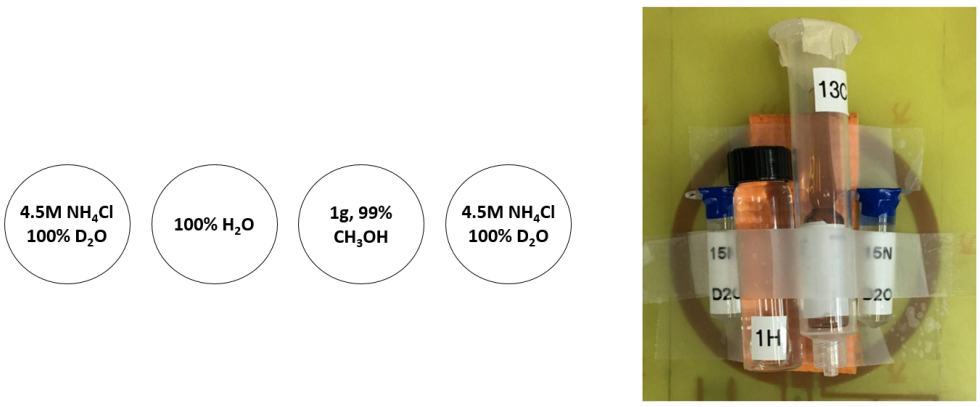

(A) (B)

Figure 25. Phantom 3 for $^{1}H/^{13}C/^{15}N$ MRS acquisition. (A) Phantom section diagram and (B) top view photograph.

IV.2.5.2 Naturally occurring condition

A naturally occurring condition was also investigated to demonstrate the triplexer front-end benefit on simultaneous multinuclear acquisition. Because the sensitivity of ^{15}N is much lower than that of ^{13}C, most research using ^{15}N uses hyperpolarization,

enrichment, or a large amount of averaging [60]. So, natural abundance work will focus on only ^{1}H and ^{13}C. Natural abundance ^{13}C and ^{1}H spectra will be acquired from isopropyl alcohol to investigate dynamic range issues that arise from studying natural abundance samples. To investigate this, a 10 mL, Phantom 4 contains 91 % solution of isopropyl alcohol in water was positioned and aligned with center conductor of the triple tuned coil.

IV.2.6 Experimental approaches

IV.2.6.1 Validate SNR performance between the triplexer front-end filtering and Varian receiver

Independent signal optimization by the triplexer front-end allows researchers to use simultaneous multinuclear acquisition with a simplified receiver chain structure (no mix down stages). But this may not be so desirable if this requires to sacrificing SNR performance too much. So, it is important to investigate the triplexer performance with a commonly known commercial systems. The experiments will be conducted by both MR imaging and spectroscopy.

$^{1}H/^{23}Na/^{2}H$ images were acquired both simultaneously through the broadband system with the front-end and separately through a Varian Unity Inova system with Phantom 2 and Coil 1. Both simultaneous multinuclear and single nuclear acquisition use single transient with a gradient echo pulse sequence. A TR of 1 s and a TE of 12 ms was used. A matrix size of 256 x 256 was applied with an acquisition time of 5.12 ms and a spectral width of 50 kHz. Separate gain was used for different nuclei, i.e. 46 dB, 52 dB, and 56 dB for ^{1}H, ^{23}Na, and ^{2}H, respectively. RF transmit power was calibrated to provide a 60, 90, and 60 degree tip angle at three nuclei respectively with the Varian system by

exciting one nuclear at a time. The RF power were interpolated to the broadband transmitter by adjusting a same power at the output of the RF amplifier for all nuclei. A sampling rate of 120 MSPS was applied for the simultaneous multinuclear digitization. Due to applying same gradients to all nuclei at same time, slice thickness and FOV will be inverse proportional to nuclear gyromagnetic ratio. Therefore, slice thickness of 1.79 mm, 6.75 mm, and 11.63 mm was applied to ^{1}H, ^{23}Na, and ^{2}H respectively. On the other hand, FOV at ^{1}H, ^{23}Na, and ^{2}H were 100 mm x 100 mm, 378 mm x 378 mm, and 651 mm x 651 mm, respectively. We zoom in ^{23}Na and ^{2}H FOV to have same FOV region as ^{1}H by extracting 67 x 67 points and 39 x 39 points, respectively. Both images were interpolated 256 by 256 for a better visual comparison.

Additionally, to demonstrate that this works with spectroscopy, $^{1}H/^{23}Na/^{2}H$ spectra were also acquired with Phantom 1 and Coil 1. The experiments were carried out in a 40 cm bore superconducting magnet at 4.7 T. A fast succession RF pulse sequence was used for the MRS acquisition which is introduced in section IV.2.1. All nuclei were calibrated to have 90 degree tip angle with the Varian in single frequency acquisition experiments. Parameters used for the single frequency experiments of three nuclei were 0.2 s acquisition time, 20 Khz spectral width, 1 average, and 2 s TR. A receive gain of 46 dB was applied to all three nuclei. The RF pulse voltage amplitude (peak-peak) used to achieve 90 degree tip angle on the Varian were also measured before the RF amplifier for the broadband transmitter power calibration. Thus, simultaneous acquisition MRS can be compared more objectively by adjusting to the same voltage amplitude at the input of the RF power amplifier. Additionally, for simultaneous acquisition, a sampling rate of 120 MSPS was

employed to implement undersampling technique at ^{1}H frequency while the other two frequencies were fully sampled and separated from ^{1}H aliased frequency.

We also validate this at $^{1}H/^{13}C/^{15}N$, spectra were acquired both simultaneously through the broadband system and separately through the Varian system with Phantom 3 and Coil 2. This was implemented in a 33 cm bore magnet. A fast succession RF pulse sequence was used in $^{1}H/^{13}C/^{15}N$ acquisition for the simultaneous multinuclear acquisition. RF power of 90 degree tip angle for all nuclei were calibrated with the Varian in single frequency acquisition experiments and same power were used in the broadband system by adjusting peak-to-peak RF voltage to same amplitude before the RF amplifier. RF power used on the Varian is 55 dB, 51 dB, and 52 dB where the gain is 26 dB, 44 dB, and 52 dB for $^{1}H/^{13}C/^{15}N$, respectively. A sampling rate of 120 MSPS was used for the simultaneous multinuclear digitization. Parameters used for the single frequency experiments of three nuclei were 0.2048 s acquisition, 10 Khz spectral width, 1 average, and 2 s TR. For ^{15}N, a 10 Hz line broadening was used to better observe the spectra in both single frequency acquisition and simultaneous acquisition.

IV.2.6.2 Validate SNR performance between 1 ADC channel and 3 ADC channels

Additionally, it must be shown that the front-end can combine all three filtered signals back into a single digitizer channel without sacrificing performance. This was done by acquiring both $^{1}H/^{23}Na/^{2}H$ and $^{1}H/^{13}C/^{15}N$ spectra simultaneously through the broadband system using the triplexer front-end filtering structure with Phantom 1 and Coil 1, and Phantom 3 and Coil 2, respectively. Spectra were acquired with and without

combining the three signals after the triplexer filtering structure. Parameters are same as described in the section IV.2.6.1.

IV.2.6.3 Validate SNR loss of the triplexer front-end hardware

In order to demonstrate the SNR improvement from using the triplexer that arises from applying separate filtering and independent gain control, the triplexer was compared to a simple low-pass filter. $^{1}H/^{23}Na/^{2}H$ MR images were acquired simultaneously using both the QWTL triplexer and a low pass filter with Phantom 2 and Coil 1. Simultaneous acquisition uses 120 MSPS sample rate where the low pass approach utilizes 240 MSPS. This low-pass filter must have a pass-band containing the resonant frequencies of all three nuclei, so a 200 MHz low-pass filter (BLP-200+, Mini-Circuits) is used. The triplexer approach uses separate narrow band filters and combines the filtered signals for digitization. The low-pass filter approach utilizes only the low-pass filter between the LNA and the digitizer. For the low-pass filter approach, the gain is optimized for ^{1}H for the later approach. Image parameters are same as described in the section IV.2.6.1.

IV.2.6.4 Demonstrate issue with one channel digitizer with same gain level

In order to demonstrate the importance of independent gain control of each nucleus, ^{1}H and ^{13}C spectra were acquired from Phantom 4 and Coil 2. With the triplexer front-end, we are still able to reconstruct ^{1}H signal and X-nuclei simultaneously without overflowing the receiver or not able to apply enough gain by simply adding independent attenuation to each path for independent signal optimization. This experiment was carried out by acquiring ^{1}H and ^{13}C simultaneously without separating the signals from each nucleus. Two approaches were compared by setting the gain level to best fit the ^{1}H signal

and the ^{13}C signal for the digitizer. A low pass filter (BLP-200+, Mini-Circuits) was applied to remove noise that are greater than proton frequency. Two approach results were also compared to optimized both nuclei separately with the triplexer front-end filtering.

IV.3 Experimental results

Experimental results of the simultaneous MRI and MRS front-ends are illustrated in this section. Performance of each module, i.e. the broadband Tx/Rx switch, the QWTL triplexer filtering, and the signal combiner, are verified on the bench with a HP 4195A network analyzer. Simultaneous three nuclei MRI and MRS at both $^{1}H/^{23}Na/^{2}H$ and $^{1}H/^{13}C/^{15}N$ are also acquired and compared with single nuclear acquisition.

IV.3.1 Broadband Tx/Rx switch isolation and circuit loss

In Figure 26, insertion loss magnitude (blue curve corresponding to blue y-axis) of the switch between the transmit port and the coil was measured across a wide range of frequencies when it was in transmit mode. It can be seen that the magnitude is less than -0.25 dB at our maximum observed frequency, 200 MHz. A forward transmit power will have a loss less than 5 % based on the insertion loss. Measured isolation between the transmit port and the receive port is presented in red curve. Even the isolation is getting worse when operating frequency increases, the maximum isolation magnitude at our maximum desired frequency, 200 Mhz, is only -33 dB. This means even a maximum RF power of 1 kW is transmitted from the RF amplifier, the maximum acceptable input power (+30dbm) of the Miteq LNA (AU-1647) is still able to handle the leaking RF power with such isolation. The overall measurements between the transmit and receive port present a

good isolation and this should be able to prevent the input RF power from leaking into receiver chain and damage the Miteq LNA.

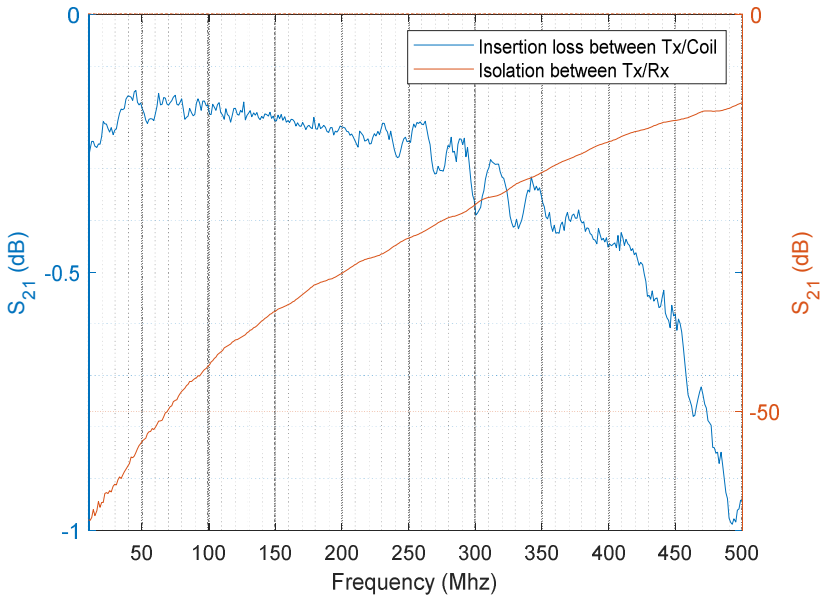

Figure 26. S-parameter plots of the broadband Tx/Rx switch at transmit mode. Blue curve presents insertion loss between the transmit port and the coil. Red curve shows isolation between the transmit port and the receive port. The corresponding y-axis is presented with same color.

IV.3.2 Three port signal combiner coupling and circuit loss

The signal combiner combines three filtered signals into one output channel in order to reduce the number of digitizer channels needed and the amount of data produced. It is important that the signal combiner not introduce an excessive amount of additional noise to the received signal. Using cascaded noise figure analysis, we can determine the contribution to the noise figure of the signal combiner. The NF of the signal combiner was

simulated based on Texas Instruments operational amplifier model which is 22.3 dB [51]. The LNA has a nominal gain of 58 dB, reducing the noise contribution of the signal combiner to an essentially negligible 0.004 dB.

Characterizing the coupling between the signal combiner inputs is desirable to maintain original signal integrity. Coupling between inputs of the signal combiner was measured as S_{21} with all other ports terminated in 50 Ω shown in Figure 27 (A). Coupling matrices at different nuclei are investigated and the worst case occurs at ^{1}H but still exceeding -30 dB. This presents a well decoupling between any two inputs of the signal combiner and helps the filtered signals retain signal integrity while combing into one channel. Figure 27 (B) shows insertion loss of the signal combiner between its inputs and output. The circuit loss for all three signal paths are quite similar and almost negligible in the observed bandwidths.

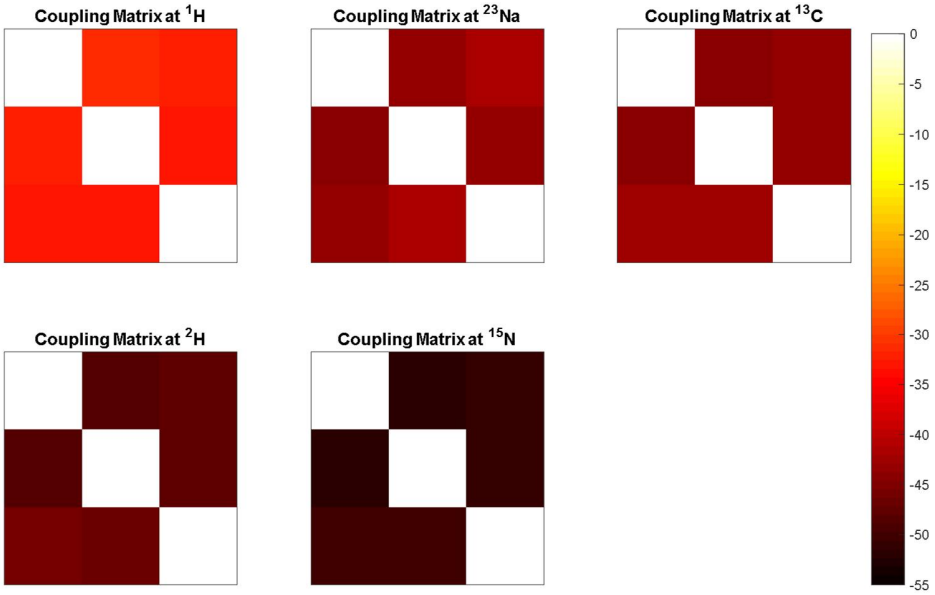

(A)

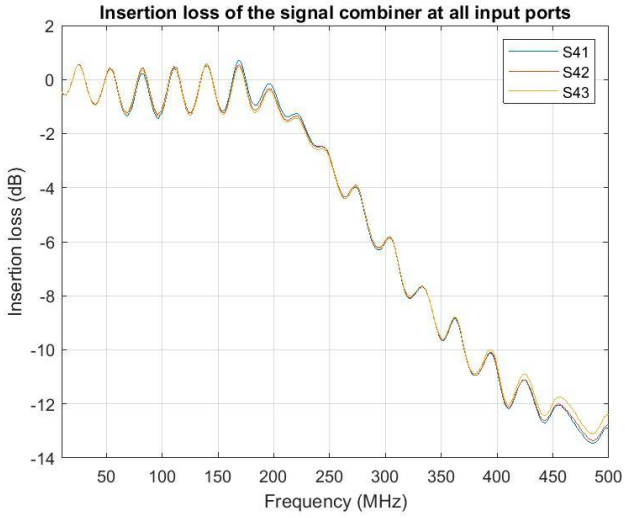

(B)

Figure 27. S-parameter measurements of the three-port signal combiner. (A) Coupling matrices at different nuclei frequency between any two inputs and (B) insertion loss between any input and the output.

IV.3.3 QWTL triplexer front-end performance

In the proposed front-end, signals will be filtered through narrow band filtering and combined back into one output channel before digitization. Any signal leaking between inputs and loss of each signal path may affect overall performance. Therefore, return loss and insertion loss were measured between the input of the QWTL triplexer and the output of the three-port signal combiner. The results were further compared with using BNC T-connectors and a 4-way commercial broadband splitter (ZFSC-4-1-S+, Mini-circuits) directly. The T-connectors and the broadband splitter are two common methods to divide an incoming power into multiple channels equally and each of channels still contains three frequencies but with less power.

Figure 28 shows return loss and insertion loss of using three different configurations at $^{1}H/^{23}Na/^{2}H$ where the 4-way splitter, the T-connectors, and the QWTL triplexer are plotted in black, blue, and red curves, respectively. In Figure 28 (A), even return loss at 52.9 Mhz may not be optimal with the QWTL triplexer, however, overall return loss at three Larmor frequencies shows an acceptable value while using the QWTL triplexer when compared to the other two structures. On the other hand, the T-connector structure and the commercial broadband 4-way splitter had the worst return loss, greater than -5 dB, at 200 Mhz and 30 Mhz, respectively. The insertion loss of both the T-connector and the 4-way splitter structure were also not as good as the QWTL triplexer presented in Figure 28 (B). In general, the 4-way splitter had an average of 6 dB more loss when compared to the QWTL triplexer at three desired bands. This is because a commercial power splitter normally has a 3 dB loss when there are two outputs and 6 dB

loss when there are four outputs. In our case, as we were using a 4-way power splitter, it is not surprising that a 6 dB loss existed. For the loss in the T-connector structure, ideally the T-connector divided the input signal intensity equally, resulting in multi-frequency entering into each channel path. But since each of bandpass filters had different input impedance for those out of band ranges, this will cause signal bouncing between bandpass filters and T-connectors. Additionally, isolation between T-connector outputs is not as good as the commercial power splitter. This makes the T-connector return loss is much worst than the other two structures and the insertion loss somehow fluctuates between the 4-way power splitter insertion loss and the QWTL triplexer insertion loss.

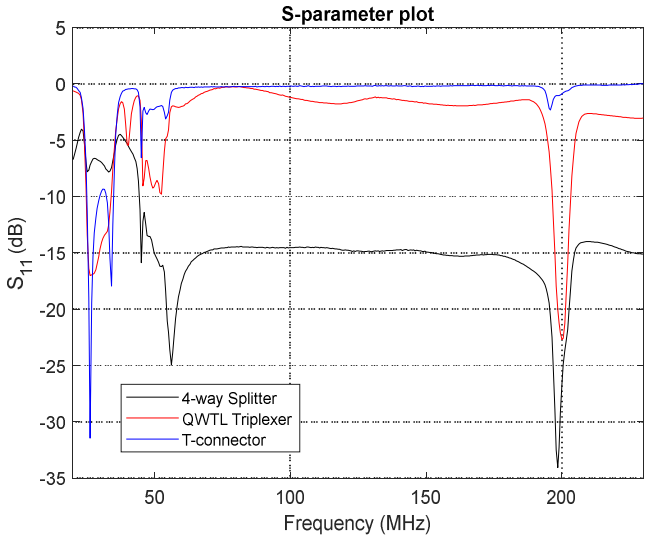

(A)

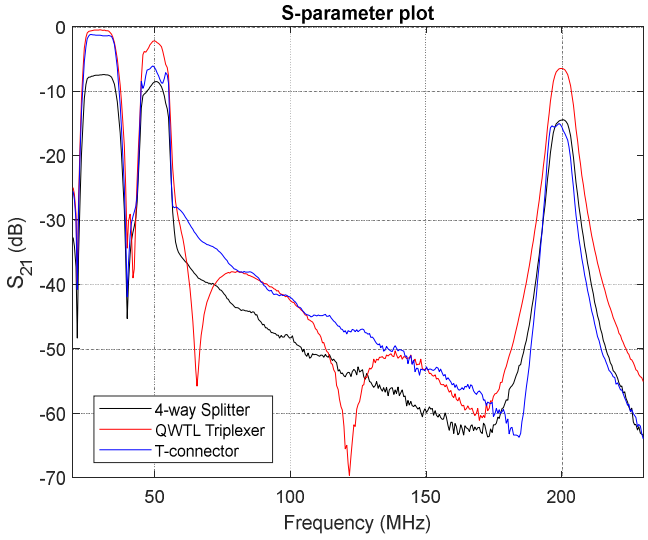

(B)

Figure 28. S-parameter measurement between the input of the RF splitting structures at $^{1}H/^{23}Na/^{2}H$ with 4-way splitter, QWTL triplexer, T-connector and the output of the three-port signal combiner. (A) Return loss and (B) insertion loss of using three configurations.

Similar measurement results were found with $^{1}H/^{13}C/^{15}N$ design presented in Figure 29. Comparison of different configurations verifies that the QWTL triplexer can have a better performance than just splitting input power evenly at outputs with either T-connectors or commercial power splitters. As we can expect, the QWTL triplexer presents the best insertion loss at all three frequency bands among these three structures both at $^{1}H/^{23}Na/^{2}H$ and $^{1}H/^{13}C/^{15}N$ while still being able to provide an acceptable return loss. The insertion loss are -6.8 dB, -3 dB, and -1 dB at ^{1}H, ^{23}Na, ^{2}H respectively. The commercial filter loss at corresponding frequencies is -6 dB, -3 dB, and -1.02 dB, respectively. Similarly, insertion loss of ^{1}H, ^{13}C, and ^{15}N are -6.8 dB, -2.1 dB, and -1 dB respectively. The corresponding filter loss is -6 dB, -2 dB, and -0.95 dB, respectively. While comparing to the triplexer front-end filtering insertion loss to the commercial filters, we can observe that proton has a slightly larger noise which is about 0.8 dB generated from the triplexer front-end. But the overall loss at each frequency is mainly dominated by the filters and this must be taken into consideration while determining overall gain stage at each signal path for simultaneous acquisition.

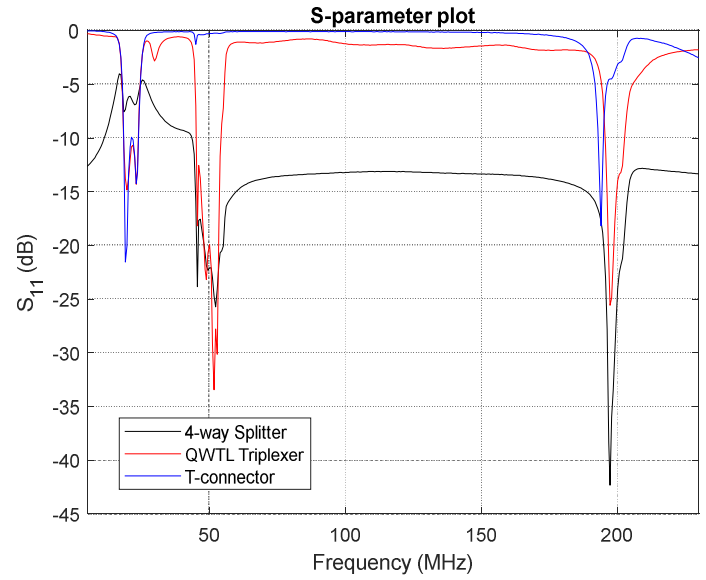

(A)

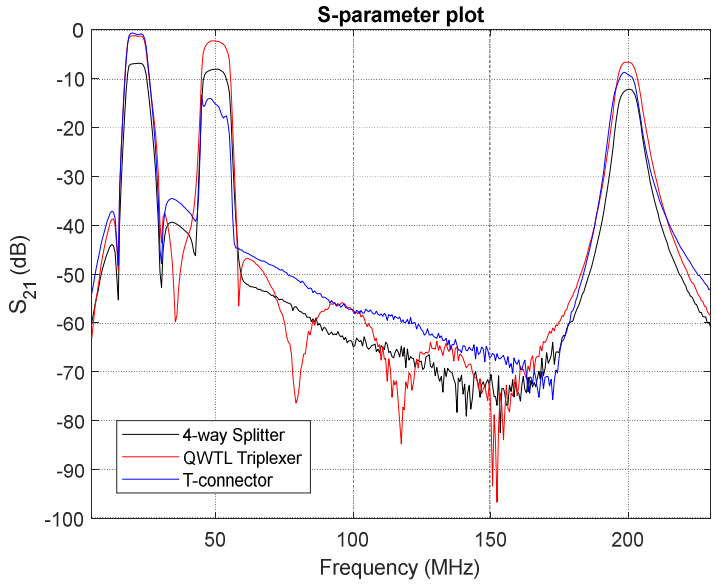

(B)

Figure 29. S-parameter measurement between the input of the RF splitting structures at $^{1}H/^{13}C/^{15}N$ with 4-way splitter, QWTL triplexer, T-connector and the output of the three-port signal combiner. (A) Return loss and (B) insertion loss of using three configurations.

IV.3.4 SNR validation

IV.3.4.1 Triplexer front-end performance

Circuits including cables in the triplexer front-end may introduce additional loss to the received signal, which can degrade SNR performance if not handled carefully. As described in section IV.2.6.1, it is necessary to compare the triplexer front-end to a commercially available system. NMR spectra from three nuclei ($^{1}H/^{23}Na/^{2}H$ and $^{1}H/^{13}C/^{15}N$) are acquired simultaneously with the triplexer front-end. This result will be compared to a commercial Varian Unity Inova System with which each nucleus is acquired separately.

Initially, the spectra were acquired at $^{1}H/^{23}Na/^{2}H$ because the ^{23}Na and ^{2}H absolute signal sensitivity is larger than ^{13}C and ^{15}N, and phantom is easier to obtain. Figure 30 shows MRS for $^{1}H/^{23}Na/^{2}H$ acquisition. The first column shows spectra obtained by the Varian system where the SNR of $^{1}H/^{23}Na/^{2}H$ is 6630, 87, and 14817, respectively. The Second column illustrates spectra acquired by the broadband system with triplexer front-end which utilizes the triplexer front-end to split the incoming broadband signal into three narrow bands for filtering and application of an optimized gain for each nucleus. All optimized signals then are combined back into one channel for digitization. The corresponding SNR in column 2 is 5176, 99, 13566, respectively. Proton shows a slightly smaller SNR in the simultaneous multinuclear acquisition. This may due to that out of band noise was added after the filtering and the reason could be from the digitizer as we described in section III.3.1. However, overall SNR is comparable between two configurations.

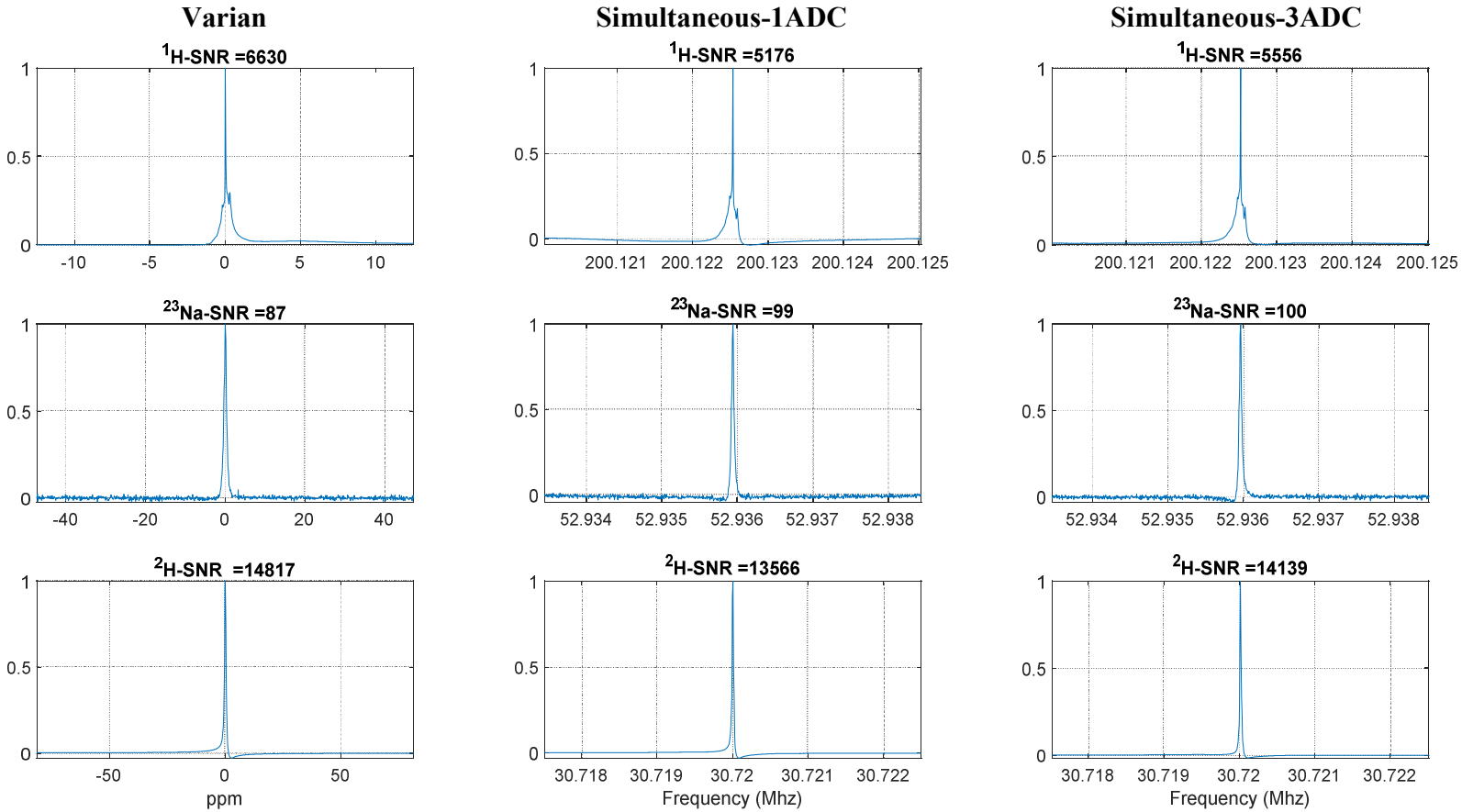

Figure 30. Single frequency and simultaneous MRS acquisition for $^{1}H/^{23}Na/^{2}H$. Spectra were normalized to its peak independently. Single transient was used for the data acquisition. First column is the single frequency acquisition by sending one frequency at a time with the Varian. Second and third column are spectra obtained with the broadband MRS system, but second column used 1 ADC channel digitization whereas third column utilized 3 ADC channel digitization.

Then, the frequency is shifted to $^{1}H/^{13}C/^{15}N$ for further verification. Figure 31 shows MRS for $^{1}H/^{13}C/^{15}N$ acquisition. Even enriched ^{15}N was used for the acquisition, the signal level was still at a lower range. To better observe the spectrum, 10 Hz line broadening was applied to ^{15}N spectrum. The first column shows spectra obtained by the Varian system where the SNR of $^{1}H/^{13}C/^{15}N$ is 6164, 54, and 8.1, respectively. The second column illustrates spectra acquired simultaneously in a single ADC channel and corresponding SNR is 5730, 80, 10.3, respectively. As we can expect, proton presents a slightly lower SNR in the simultaneous acquisition as it appears in $^{1}H/^{23}Na/^{2}H$ MRS acquisition. This could be same issue that noise was added after the filtering and a possible reason is from the digitizer. Here, we notice that carbon also shows a lower SNR in the Varian system. We doubt that the Varian system is not stable when frequency is around 50 Mhz. While looking back in $^{1}H/^{23}Na/^{2}H$ acquisition, we can observe that sodium with similar frequency range also presents a slightly lower SNR in the Varian system. This somehow shows the Varian system will acquire a larger noise at this frequency region.

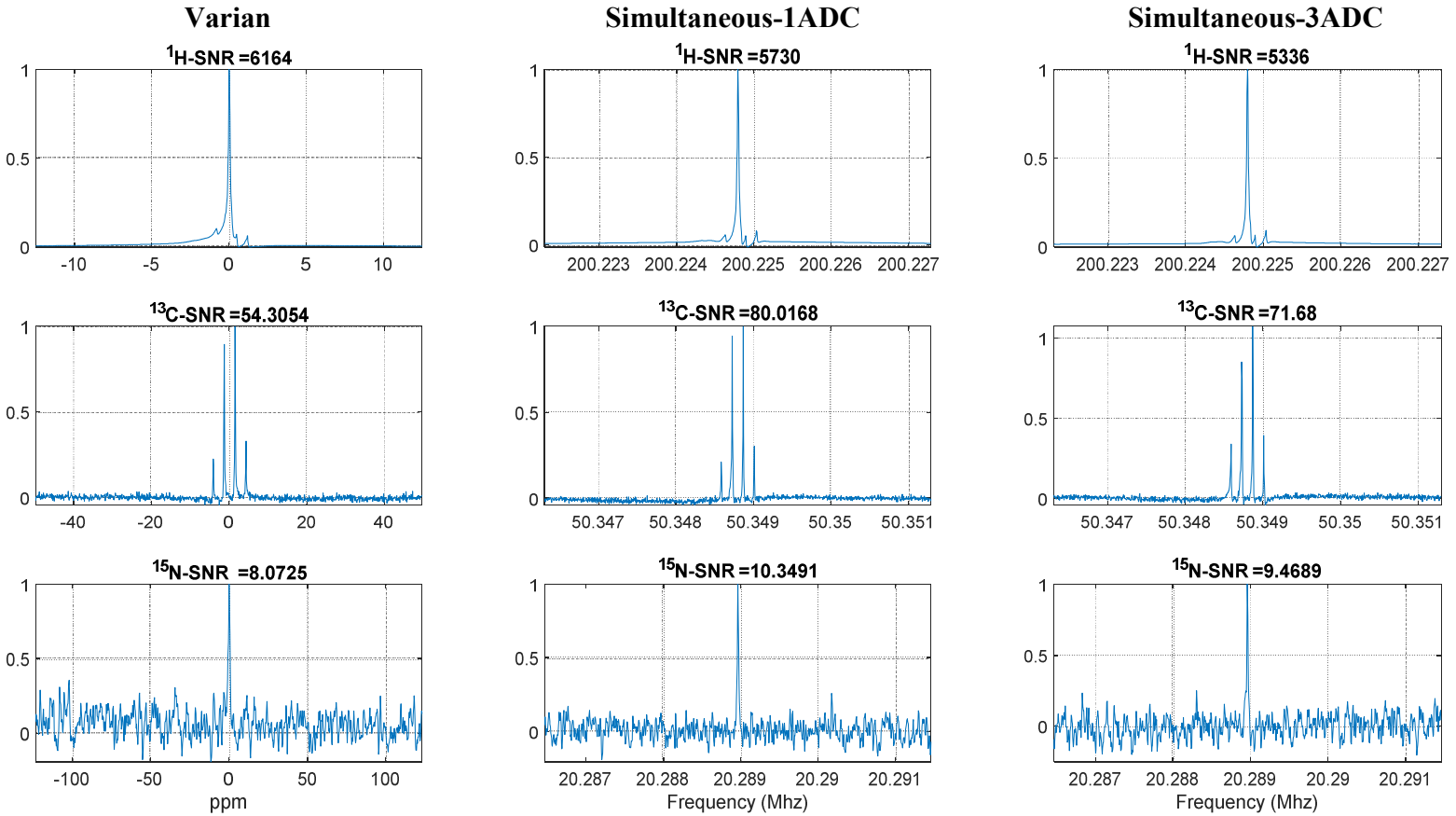

Figure 31. Single frequency and simultaneous MRS acquisition for $^{1}H/^{13}C/^{15}N$. Spectra were normalized to its peak independently. Single transient was used while ^{15}N applied a 10 Hz line broadening. First column is the single frequency acquisition by sending one frequency at a time with the Varian. Second and third column are spectra obtained with the broadband MRS system, but second column used 1 ADC channel digitization whereas third column utilized 3 ADC channel digitization.

The performance of the triplexer front-end loss is also demonstrated with MR imaging, shown in Figure 32 first and third column. First column images were acquired simultaneously with the front-end whereas third column images were obtained separately with the Varian Unity Inova system. In the simultaneous acquisition, each nucleus experiences the same gradient fields, resulting in different FOV because of the difference in gyromagnetic ratio. But the FOV of X-nuclei in Figure 32 is interpolated to 100 mm x 100 mm as described in section IV.2.6.1 for better visualization.

While comparing two approaches, proton SNR presents a slightly lower where sodium shows a higher SNR in the simultaneous acquisition. These are similar to the spectroscopy results as we have discussed previously. Importantly, all nuclei SNR is corresponding to the concentration at different spatial location. Overall, all nuclei SNR shows approximately in a same level. Till now, this section demonstrated that the triplexer front-end can be applied on the simultaneous multinuclear and the performance is as well as a commercial Varian Unity Inova system receiver on both MR imaging and spectroscopy.

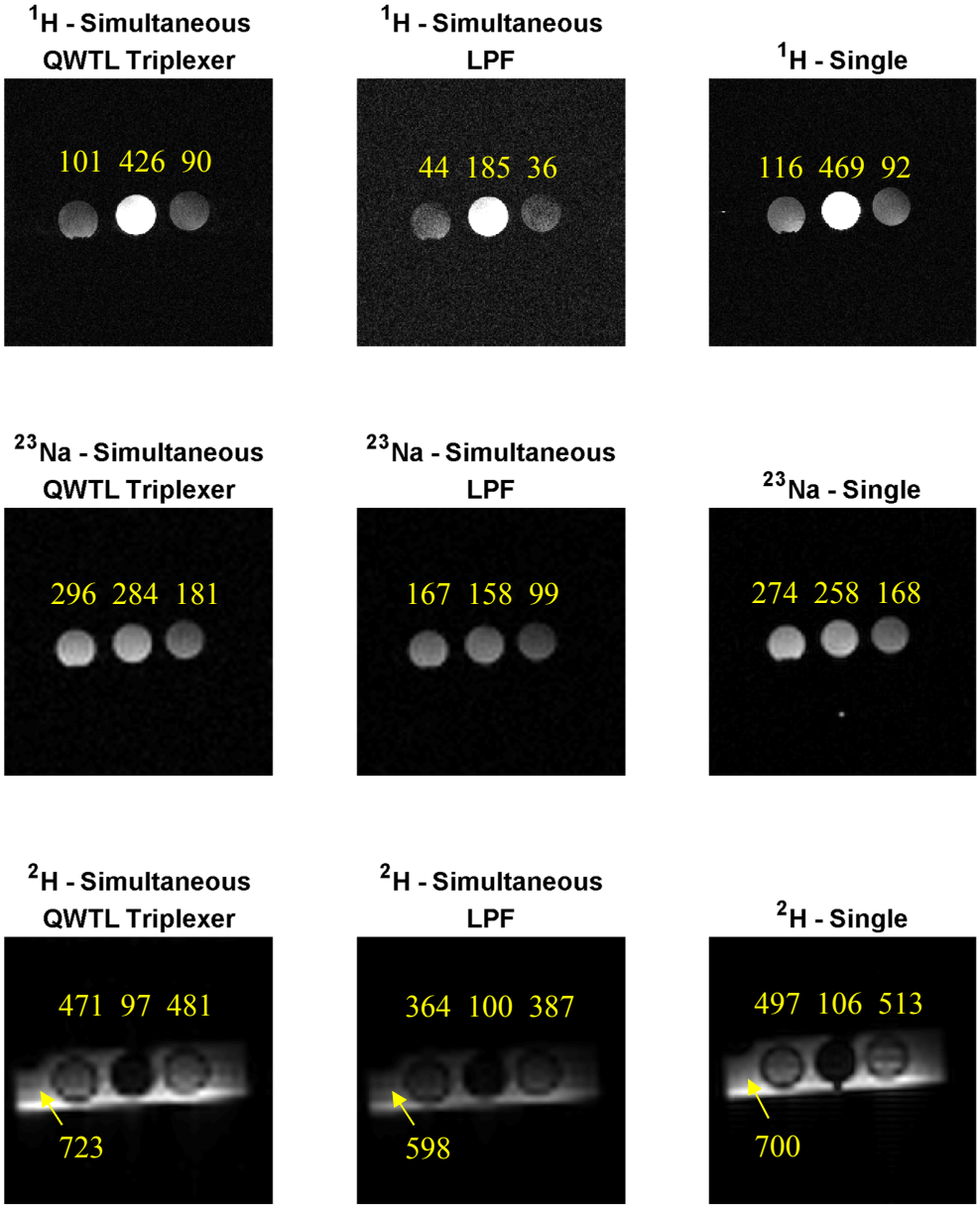

Figure 32. Simultaneous multinuclear and single nuclear MRI at ^{1}H/^{23}Na/^{2}H with corresponding SNR. A single transient was acquired at all nuclei. X-nuclei (^{23}Na and ^{2}H) images are resized to same FOV relative to ^{1}H. First and second column presents images acquired with the proposed front-end filtering and a wideband, low pass filtering respectively using simultaneous acquisition. The overall SNR of all nuclei present at a lower value while using a low pass filter due to out of band noise is aliased into ^{1}H band and not enough gain is applied at X-nuclei. Third column shows images acquired from the Varian with single nuclear acquisition separately and SNR of all nuclei is comparable to simultaneous acquisition with the proposed front-end.

IV.3.4.2 Triplexer front-end with one channel acquisition

Digitizing the signal from all three nuclei in a single channel provides is superior to digitizing them separately because it generates less data and allows other digitizer channels to remain available. However, combining the filtered signals back into one channel can result in the introduction of noise, degrading SNR performance. In order to investigate this, we compare the SNR of spectra acquired using 1 ADC channel for all three nuclei and 3 ADC channels, one for each nucleus.

In Figure 30, the $^{1}H/^{23}Na/^{2}H$ spectra in both the second and third column were acquired simultaneously with 1 ADC channel and 3 ADC channels respectively. The corresponding SNR for both two configurations is 5176, 99, 13566, and 5556, 100, 14139, respectively.

In Figure 31, the $^{1}H/^{13}C/^{15}N$ spectra in both the second and third columns were acquired simultaneously with 1 ADC channel and 3 ADC channels respectively. The corresponding SNR for both two configurations is 5730, 80, 10.3, and 5336, 72, 9.5, respectively.

Both approaches show a comparable SNR for all nuclei. This demonstrates that digitizing all nuclei with the front-end going into a single ADC can perform as well as digitizing three nuclei in separate channels, but producing 1/3 as much raw data.

IV.3.4.3 Triplexer front-end loss

Undersampling allows researchers to digitize signals while producing less data. To avoid aliased noise from degrading the SNR, proper filtering is required for each

frequency of interest. The proposed front-end can provide such filtering to achieve preserve the SNR while undersampling.

The advantage to using this front-end to condition a signal for undersampling can be shown by comparison to a single low-pass anti-aliasing filter. This was done by acquiring $^{1}H/^{23}Na/^{2}H$ images as described section IV2.6.3. The images are shown in Figure 32. The first column is our reference image acquired simultaneously with the triplexer front-end filtering. The second column is images acquired with the low pass filtering approach. As a constant gain is optimized at proton, ideally proton should maintain similar SNR relative to the triplexer approach. While digitizing with a sampling rate of 240 MSPS, out of band signal and noise that are at 120 MHz will fold back onto the signal band and degrade proton SNR. From Figure 32, the SNR decreases from 101 to 44, as expected. This shows that separating the nuclei and using independent narrow band filtering can benefit undersampled simultaneous acquisition.

For both X-nuclear images, SNR is also reduced when using the low pass filtering approach. This is because not applying optimized gain and proper filtering for both nuclei independently. The optimized gain at each nuclear to fit its signal sensitivity will be discussed in more detail in the next section.

IV.3.5 Dynamic range validation

The broadband receive signal goes into a single channel with a constant gain and fixed pass-band. Signal from only one nucleus can be optimized to fit the digitizer's limited dynamic range while other nuclei may either saturate the digitizer or not have enough gain.

Figure 33 shows simultaneously acquired ^{1}H and ^{13}C spectra with different filtering configurations. The spectra in the first column were obtained with the triplexer front-end whereas spectra in the second and third columns were acquired with a low pass filter, BLP-200+, and a constant gain applied to all signal. When gain is optimized for ^{1}H (third column) and compared to the triplexer approach, we can observe that ^{13}C SNR decreases because insufficient gain has been applied to the signal. Importantly. out of band noise at higher frequency will aliase into this region, making it difficult to discern the spectra. We can also observe that ^{1}H has a smaller SNR relative to using the triplexer. This is from out of band noise at 60 MHz which the ^{1}H signal aliases on top of, degrading SNR.

When the gain is optimized for ^{13}C (second column), we can observe that the SNR of ^{1}H decreases significantly because the large gain causes the ^{1}H signal to saturate the digitizer. This also degrades the SNR of ^{13}C, as a saturated digitizer will poorly capture weaker signals. Additionally, there is noise aliasing down into the ^{13}C signal, further degrading the SNR.

From the two approaches, we can see that single channel, single filtering does degrade SNR performance on both ^{1}H and ^{13}C because it does not provide either proper filtering to remove out of band noise or separate gain to fit each nuclear sensitivity. Although we are still able to acquire multiple nuclei simultaneously in this case, the performance is dramatically worse.

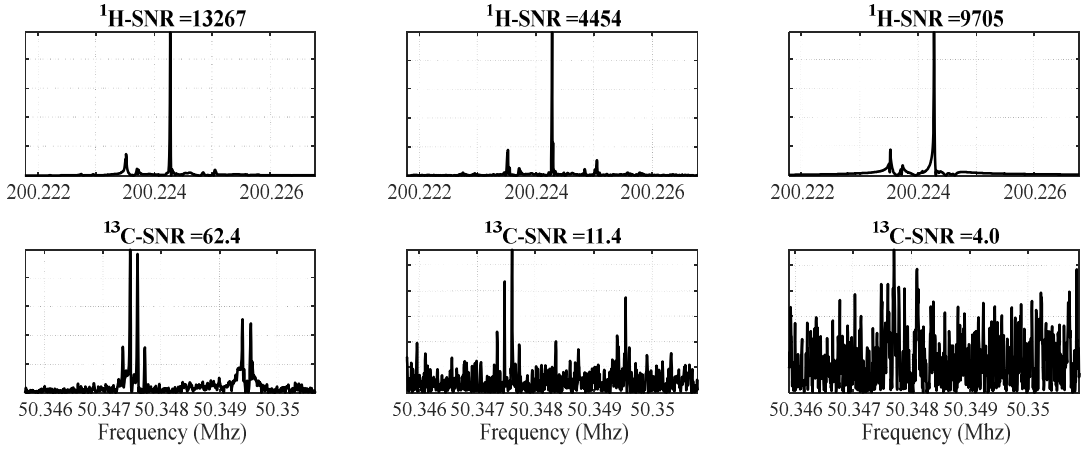

Figure 33. Simultaneous ^{1}H and ^{13}C MRS with different filtering and gain approach using 64 averages. 10 Hz line broadening is applied to ^{13}C spectra and all spectra are normalized to its peak First column shows spectra acquired by the triplexer front-end with gain optimized for each nucleus. Second column and third column are spectra obtained with a low pass filter with a constant gain optimized at carbon and proton, respectively. Single filtering does degrade SNR on both nuclei no matter gain is optimized at proton or carbon because it does not provide either proper filtering to remove out of band noise or separate gain to fit each nuclear sensitivity

IV.4 Discussion and conclusion

Use of a home-built triplexer front-end allows signals from multiple nuclei to be acquired with no reduction in SNR. Additionally, because each nucleus is filtered separately and can have its gain independently adjusted, three nuclei can be acquired with the same high-speed digitizer.

Enabling the signals from a triple-tuned coil to be acquired by a single digitizer channel is important for the development of arrays of dual or triple-tuned elements. Supporting the use of single-port triple-tuned coils reduces the difficulty of constructing multi-tuned arrays, as only a single cable is required for each element. Reducing the cost and complexity of receive hardware is also crucial for making these arrays feasible.

Allowing multiple nuclei to share a digitizer channel greatly reduces the number of required receive channels, which are typically the most expensive part of the MR receive system.

Without independent control over the gain of each received nucleus, a much higher resolution digitizer would be required to simultaneously capture signals from nuclei with large differences in sensitivity. For example, a dynamic range of at least 108.3 dB would be needed in order to acquire both ^{1}H and ^{15}N from a natural abundance sample based on nuclear absolute sensitivity. In this case, a digitizer with at minimum effective resolution of 18 bits would be required to digitize both signals without saturating the digitizer. Importantly, the triplexer front-end enables us to apply independent attenuation to reduce the ^{1}H amplitude in order to prevent saturation, allowing us to achieve good results with a 16-bit digitizer.

Without independent control of the gain from each nucleus, it would be necessary to use another approach to reduce the ^{1}H signal. A very small tip angle could be used, or a water-suppression technique such as jump-return or watergate could be used to reduce the signal [61, 62]. However, suppression techniques may have come are sensitive to non-uniform excitation profiles, B_0 inhomogeneities and can introduce severe baseline distortions. So, the ideal solution is to use the triplexer front-end to reduce the difference in dynamic range between nuclei.

Our present direct sampling scheme digitizes a whole spectrum where the bandwidth will contain all of the desired resonant frequencies. Even when undersampling, the amount of data produced is still very large and is driven by the sample rate. How low

we can take the sampling rate is limited by the quality of our filters. The it is important that the aliased passbands do not overlap so that noise does not alias into the signals. The most effective approach to further reduce the size of the raw data produced is to integrate into the digitizer multiple narrow-band digital down-conversion (DDC) receivers. If the signal has been down-converted, filtered, and decimated, it would be possible to only record narrow-band signals. Performing down-conversion in hardware would greatly reduce the size of data files produced, reducing the computational burden of post-processing.

CHAPTER V

INVESTIGATION OF BROADBAND PREAMP DECOUPLING APPROACH WITH A HIGH INPUT IMPEDANCE OPERATIONAL AMPLIFIER

V.1 Introduction

Array coils have been investigated during these years due to its advantages, e.g. improved sensitivity, reduced scan time, etc. However, coupling between coil elements has always been a major issue while it can degrade the overall MRI/MRS performance. Section II.4 illustrates the conventional preamp decoupling by using a matching network to match the coil to 50 Ω and transforms the preamplifier impedance from low to an open circuit to block the induced current between coils. While we are investigating multiple frequency decoupling here, this approach may still be possible but requires relative cumbersome matching networks which will add loss before preamplifiers. On the other hand, the proposed structure shown in Figure 6 (B) utilizes high input impedance characteristic of an Op Amp to achieve a reflection coefficient of nearly 1.0 to block the input current. The advantage of this method is that these devices are inexpensive when compared to commercial low input impedance preamplifiers. Moreover, it can provide a very high input impedance over a wide operating range of frequencies. It is also important to note that the amplifier noise is a key factor when deciding the amplifier. As technology improves day by day, we have found an Op Amp from Texas Instruments (OPA847) with a very low input referred voltage noise of 0.85 $\mathrm{nV}/\sqrt{Hz}$ [63]. With such low noise capability, we believe this can be a main component in the broadband preamplification stage design.

V.2 Amplifier circuit development

In this section, the Op Amp circuit was developed by Kicad. The circuit schematic and physical hardware are shown in Figure 34. The circuit was designed based on the noninverting Op Amp configuration with a voltage gain ratio of 20 by setting the feedback resistor to 750 Ω and the ground resistor to 39.2 Ω. While designing the amplification stage with an Op Amp, DC block at both input and output of the Op Amp must be taken into consideration to prevent previous or later stage from affecting bias current loading. Otherwise, input bias voltage may swing and the Op Amp becomes unstable or saturated if DC voltage is not well isolated in the AC amplification. From Figure 34 (A), we can see that there are three DC block capacitors at both input terminals and one output terminal of OPA847. At the input of OPA847, R3 and C8 create a high pass filter for the measured signal. In general, C8 has to perform at least less than 0.2 Ω for the lowest observed frequency (68 nF, 1206B683K500N, Garrett). This presents a short circuit for AC signal with a frequency higher than 2.3 Mhz while still being able to block DC voltage.

The OPA847 can operate at both single side supply and dual side configuration. Here, we choose dual power configuration which allows an output of the amplifier to swing from -Vcc to Vcc. The advantage of dual supply mode than single supply is to provide a more accurate output if input signals are around ground reference without a need to add a biasing circuit. Moreover, adding additional biasing circuit makes the circuit more complex and have a larger power consumption. Common-mode noise from power supply may also be amplified along with the input signal while using single power supply configuration.

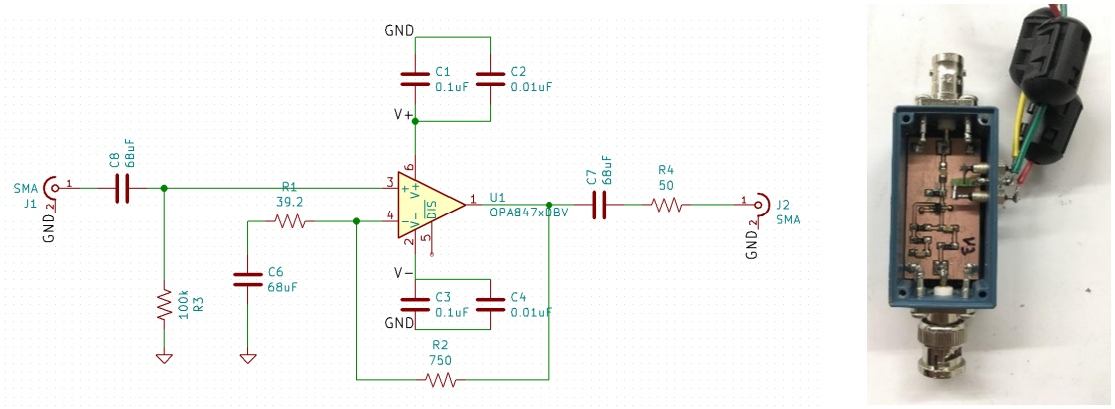

(A) (B)

Figure 34. OPA847 amplifier (A) circuit schematic by using a noninverting configuration with dual power supply and (B) physical hardware top view.

While designing an amplifier, the amplified gain ratio is the most important factor. Without a functional gain amplification, we cannot enlarge the input NMR signal. This will result in inaccurate measurements because of the small input signal and noise. Importantly, signal noise will even lower than device noise floor level during digitization. Therefore, before discussing the NF of OPA847, we have to confirm that the Op Amp can operate as a functional amplification stage.

For unterminated noninverting Op Amp configuration, simulated voltage gain curve from TINA-TI SPICE (Texas Instruments) and measured voltage gain curve are illustrated in Figure 35. Two gain curves are not matched perfectly, however, the overall gain curves are in negative values. This tells us that the unterminated configuration cannot amplify the input signal correctly even though this allows us to achieve an optimal NF for OPA847.

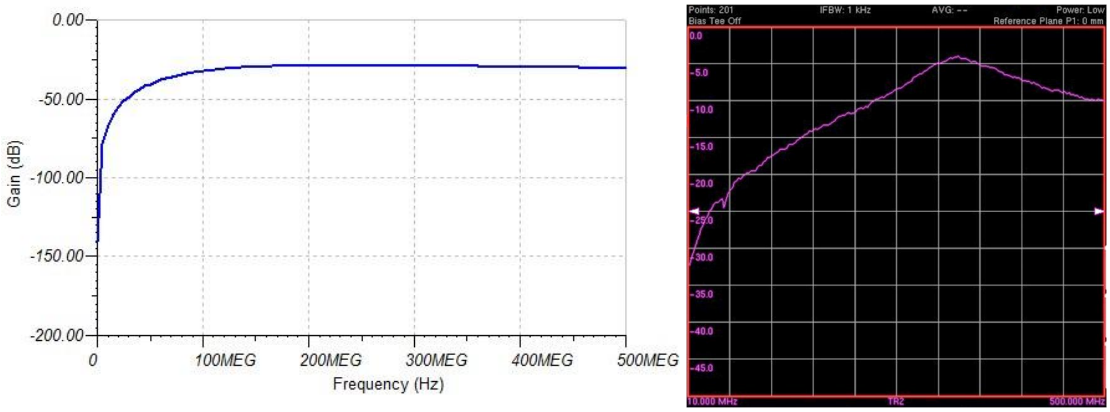

(A) (B)

Figure 35. Unterminated OPA847 gain curve between input and output from (A) TINA-TI simulation and (B) bench measurement.

One of the possible reasons that causes above issue may be that there is no DC ground path for the bias current. In order to verify this, we use terminated configuration with a termination resistor of 100 kΩ to mimic unterminated configuration. With a given bias current of -19 uA in datasheet, a bias voltage of -1.9 V will present at the noninverting input. Since OPA847 is operated at dual supply from -5 V to 5 V and the input bias voltage is in this region, the output signal will not be saturated with such condition. As expected, the simulated gain curve corresponds to bench measurement results presented in Figure 36. Even this terminated configuration is not exactly same as the unterminated structure, however, the simulated NF difference between two configurations is less than 0.02 dB and this terminated configuration can still provide a proper gain stage. Therefore, we will be using the terminated configuration with R_T equals 100 kΩ to mimic unterminated design in the real world.

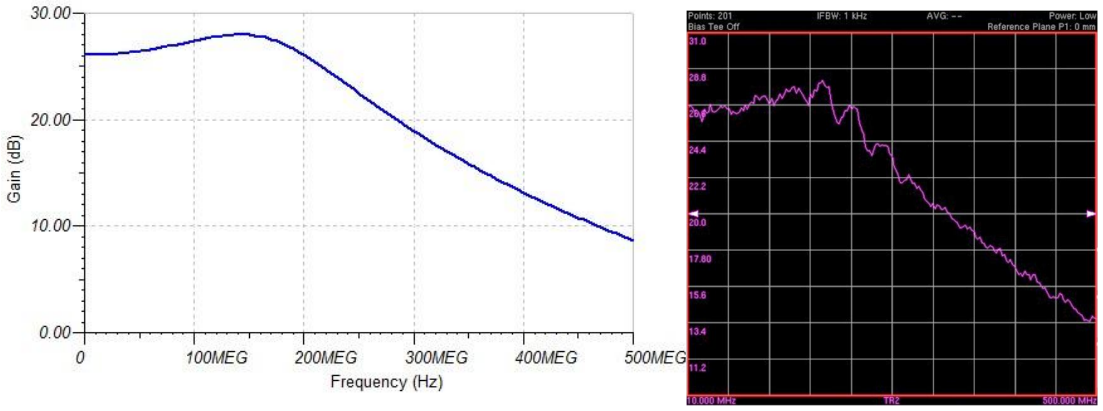

(A) (B)

Figure 36. Terminated OPA847 gain curve between input and output with R_T=100 kΩ from (A) TINA-TI simulation and (B) bench measurement.

V.3 Noise figure

As described in section II.4, noise generated in the early amplified stages contribute most of the noise in the system. Therefore, it is important to analyze the noise in the preamplifier itself because it can affect overall noise power at the output. Therefore, developing noise models of an Op Amp can benefit us in designing preamplification stage while still achieving a desirable NF as well as gain ratio.

A noninverting noise model was developed based on Karki [51] where the model diagram is shown in Figure 37. Noise sources can be identified from two input referred current noise, i_{ni} and i_{ii} at noninverting and inverting ports respectively, one input referred voltage noise, e_{ni} at noninverting input port, and with associated external impedances, R_S, R_F, R_G, and R_T. Generally, an overall Op Amp voltage noise density will depend on the equivalent source resistance. With different source resistances, dominated

noise could be either from intrinsic voltage noise, thermal noise, or current noise which makes us hard to design the circuit. This is why we need a noise model to fully understand the noise level in an Op Amp. Friis [46] has demonstrated that NF of a device is the power ratio of the input SNR to the output SNR.

$$F = \frac{S_i/N_i}{S_o/N_o} = \frac{N_o}{GN_i} = 1 + \frac{N_A}{N_i} \tag{9}$$

where S_i and S_o are signals at input and output of the amplifier respectively in Figure 37. Similarly to noise, N_i and N_o are noise power at input and output of the amplifier respectively. N_A is the added noise by the amplifier itself which will contribute to the total input available noise power and G is the amplifier gain.

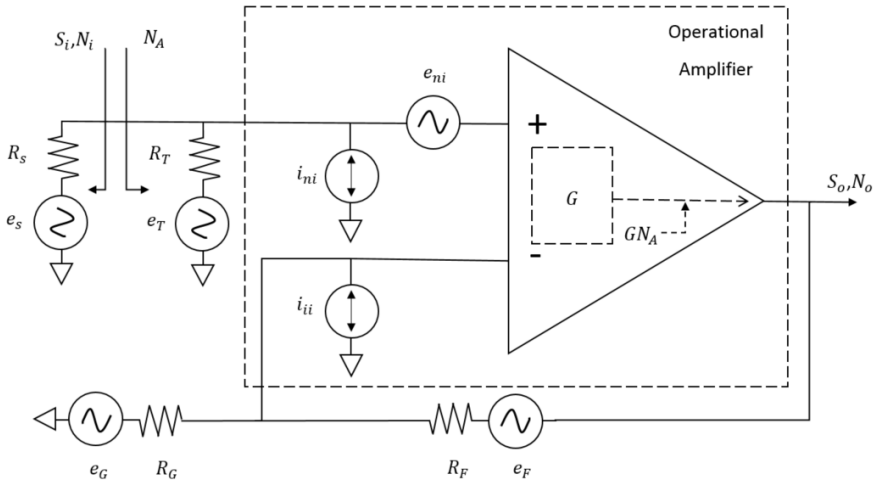

Figure 37. Overall noise source in a noninverting Op Amp model.

From Eq. (9), N_A and N_i must be calculated in order to acquire the amplifier NF. All noise forms are presented as a power term. Therefore, noise will be listed in a voltage-square terms in the following derivation. From Figure 37, the added noise from the amplifier can be written as

$$N_A = C_1 e_{ni}^2 + C_2 i_{ni}^2 + C_3 i_{ii}^2 + C_4 e_T^2 + C_5 e_G^2 + C_6 e_F^2 \tag{10}$$

where C_1 to C_6 are corresponding scaling factors to each of noise sources and e_T, e_G, e_F are voltage noise generated from resistors. As the noninverting voltage noise is fed directly to the input of the amplifier, the scaling factor can be realized as a unity which is

$$C_1 e_{ni}^2 = e_{ni}^2 \tag{11}$$

For current noise at both input ports, the current will generate a voltage while flowing through resistors. For example, an input voltage is presented at noninverting input port when i_{ni} flows through in parallel combination of source resistor (R_S) and termination resistor (R_T). Thus, the scaling factor of i_{ni} noise is

$$C_2 i_{ni}^2 = \left(\frac{R_S R_T}{R_S + R_T}\right)^2 i_{ni}^2 \tag{12}$$

Same as the other current noise i_{ii}, the scaling factor is based on the input voltage at inverting input port generated from the current noise flowing through parallel combination of R_F and R_G. The scaling factor then can be written as

$$C_3 i_{ii}^2 = \left(\frac{R_F R_G}{R_F + R_G}\right)^2 i_{ii}^2 \tag{13}$$

For the other three noise sources, noise generated from resistors is regarded as a thermal voltage noise, e.g. overall voltage noise e_T from R_T will be $\sqrt{4kTR_T}$ where k is Boltzman's constant, T is temperature in Kelvin. Once a thermal voltage is known, the

input effective voltage at noninverting port can be calculated based on voltage divider between R_S and R_G. Thus, the scaling factor of e_T is

$$C_4 e_T^2 = \left(\frac{R_S}{R_S+R_T}\right)^2 4kTR_T \tag{14}$$

With the same concept of effective input noise voltage, the scaling factors of e_G and e_F are presented as

$$C_5 e_G^2 = \left(\frac{R_F}{R_F+R_G}\right)^2 4kTR_G \tag{15}$$

$$C_6 e_F^2 = \left(\frac{R_G}{R_F+R_G}\right)^2 4kTR_F \tag{16}$$

The source voltage noise delivered to the amplifier input can also be derived by applying voltage divider between R_S and R_T with a thermal voltage noise $\sqrt{4kTR_S}$, so that

$$N_I = \left(\frac{R_T}{R_S+R_T}\right)^2 4kTR_S \tag{17}$$

Recall Eq. (9), NF of a noninverting operational amplifier can be obtained from these calculated scaling factors of each noise source derived from Eq. (11) to Eq. (17). Inverting and differential models were also developed which are not shown in this dissertation in order to find a suitable Op Amp.

V.3.1 Simulated noise figure with developed model

Determine the NF of a given preamplifier circuit is an important factor for a receiver because we need to know how much noise is being added from the circuit. To ensure the credibility of the developed noise models, we compare some common Op Amp measured NFs from Texas Instruments document [51]. Table 5 shows that both simulated and measured NF are quite comparable.

Table 5. Comparison of simulated NF (from noise models) and measured NF (from Texas Instruments) with different Op Amp configurations.

Op Amp Model	Configuration	Simulated NF (dB)	Measured NF (dB)
THS3202	Noninverting	13.5	13.0
THS3202	Inverting	11.4	11.5
THS4501	Differential	30.1	30.6

With the developed noise model, we found that OPA847 Op Amp can provide an optimal NF of 1.32 dB when an input source resistance is 458 Ω which is shown in Figure 38. This simulation was done by using a noninverting Op Amp configuration with a voltage gain of 20 by setting the feedback resistor (R_F) to 750 Ω and the ground resistor (R_G) to 39.2 Ω, and a termination resistor (R_T) of 100 kΩ. It is noted that this case is not matched to source impedance. However, using such a configuration allows us to have minimal NF even it is not power matched. Generally, coils are made from copper and have very low resistance. An impedance transformation structure is necessary to transform the coil impedance into the optimized source resistance region in order to have a good noise figure. This part will be discussed in the later section.

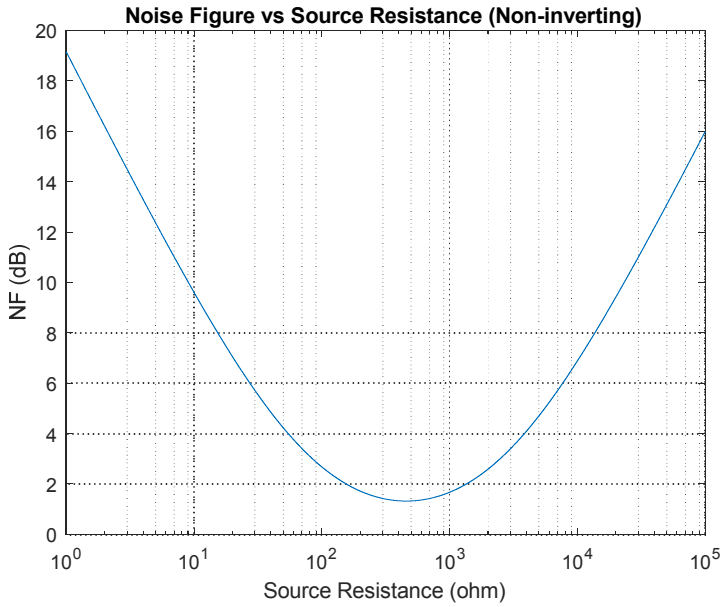

Figure 38. Simulated OPA847 NF versus source resistance with noninverting configuration. A termination resistor is set to 100 kΩ with a voltage gain ratio of 20 V/V.

From Figure 38, we can observe that OPA847 has the advantage of providing low NF which is less than 3 dB over a wide range of source resistance range from tens of Ω to kilo Ω. The broadband high input impedance characteristic of the OPA847 gives us a flexible frequency range while still being able to provide impedance block function for the induced current generated from other coils. Thus, in this dissertation, OPA847 will be used as a main component for the broadband decoupling preamp unless a better device is found.

V.3.2 Measured noise figure with Y-factor

One simple way to measure NF is to use the cold source approach. By measuring the gain and the output noise power of the tested amplifier, NF can be calculated by using

Eq. (9). However, this approach only applies to those large NF devices. The measured results may be highly inaccurate when dealing with low noise preamplifiers. Thus, we are using another measurement here, Y-factor approach, which can provide a more precise measurement for small NF devices. Typically, Y-factor utilizes two different temperature noise at input termination which is also known as hot/cold source. Y value is defined as the ratio between two output noise power listed below,

$$Y = \frac{N_{o,T_H}}{N_{o,T_C}} = \frac{N_{i,T_H}+N_A}{N_{i,T_C}+N_A} \tag{18}$$

where N_{i,T_H} and N_{i,T_C} are two different temperature input noise sources and N_A is the added amplifier input noise power.

From Eq. (18), additional added input noise by the amplifier, N_A can be solved as

$$N_A = \frac{YN_{i,T_C}-N_{i,T_H}}{1-Y} \tag{19}$$

We can assume that N_A, N_{i,T_C}, and N_{i,T_H} are noise originated from random sources, i.e. thermal noise because other sources are negligible. Therefore, noise power can be written as

$$N = kTB \tag{20}$$

where k is Boltzman's constant, T is temperature in Kelvin, and B is an observed bandwidth.

In the hot/cold source measurements, the input noise is generated with resistors at two different temperatures. We can have one of two noise sources to be equivalent to room temperature. The other noise source can either be higher or lower than the room

temperature. When bandwidth is constant, amplifier effective temperature is obtained by substituting Eq. (20) into Eq. (19),

$$T_A = \frac{YT_C - T_H}{1-Y} \tag{21}$$

Generally, input noise is from terminated resistors and the circuit network itself. While keeping the terminated resistance constant, input noise is proportional to temperature. The lower the resistor temperature, the lower the noise will be. Therefore, having high temperature T_H equals to T_0 is desirable so that we can keep the other temperature as low as possible. Typically, liquid nitrogen (LN_2) is used to cool down the resistor temperature, T_C, down to 77 K which can be seen in Figure 39. A spectrum analyzer is used to detect noise power for the DUT. If the DUT gain is not high enough, an additional amplifier at the DUT output is needed to elevate the power of the measured device.

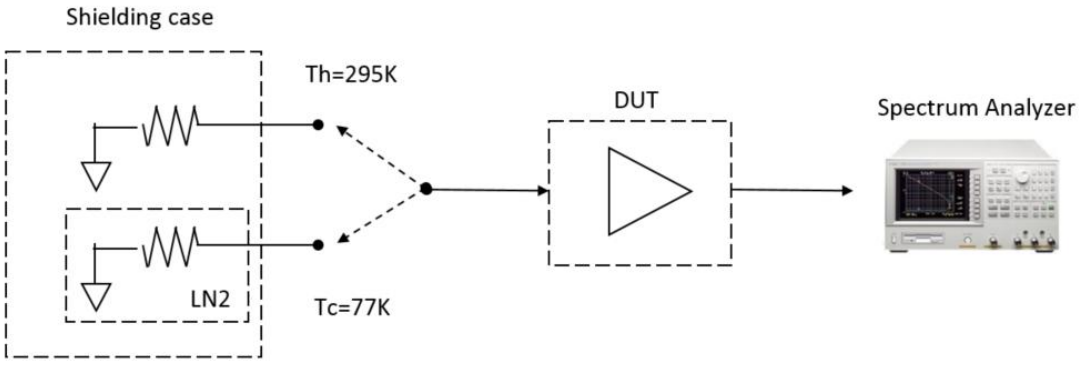

Figure 39. NF measurement setup diagram by using Y-factor method with hot/cold noise source.

Using spectrum analyzers is preferable because it can have better sensitivity over power meters. The measurement procedure is quite straight forward. First, measure the noise power, N_{o,T_H}, when load resistor is placed at 295 K. Then, toggle the switch to the other resistor which is immersed in LN_2 and monitor the noise power, N_{o,T_C}, until it gets stabilized. Now, the Y-factor can be calculated by using Eq. (18) when both hot/cold source noise power are obtained. Next, equivalent noise temperature of the amplifier is calculated from Eq. (21). Combining Eq. (9) and Eq. (20), we have

$$F = 1 + \frac{T_A}{T_0} \tag{22}$$

With a known equivalent amplifier temperature from Eq. (21), Eq. (22) allows us to obtain the measured NF of the amplifier.

Table 6 presents all measured NF by using above mentioned Y-factor approach with different preamplifiers. All measured NFs here are including cable loss where the cables are used to connect hot/cold resistors to DUT before spectrum analyzer. All corresponding cable loss is described in Table 7. We can observe that both the Miteq (AU-1583) and the HP (8447A) preamplifiers show that NFs are at a stable region. Similarly, the measured NF of OPA847 are also stable for both R_T equals to 50 Ω and 100 kΩ.

Table 6. Measured NF of different preamplifiers including cable losses at different frequencies. Column 1 and 2 are NF from commercial matched preamplifiers. Column 3 to 4 are measured NF from OPA847 whereas column 3 is a matched case and column 4 is used to mimic unterminated case.

Frequency (Mhz)	Miteq1583 (dB)	HP8447A (dB)	OPA847 (dB) (R_T=50 Ω)	OPA847 (dB) (R_T=100 kΩ)
20.3	1.42	6.33	10.58	5.88
30.7	1.43	6.33	10.17	5.96
52.9	1.54	6.68	10.89	6.05
81	1.53	7.83	10.73	5.44
200.2	2.11	8.49	12.37	6.05

Table 7. Physical cable loss at different frequencies.

Frequency (Mhz)	Cable loss (dB)
20.3	0.23
30.7	0.29
52.9	0.39
81	0.52
200.2	0.83

While reading noise power from spectrum analyzer, a reading error may exist and is known as a probable error. It can be described as εP_0. If we assume this error is 1 percent, then corresponding probable error can be calculated based on Mumfort [64].

$$\mathrm{PE(dB)} \cong 4.34 \times \mathrm{Y} \times \left(\frac{Y+1}{Y-1}\right) \times \varepsilon \tag{23}$$

where Y is Y-factor value in dB and ε is 0.01. Therefore, a probable error curve corresponding to Y-1 can be plotted based on Eq. (23) illustrated in Figure 40. Then, we are able to calculate the reading probable error for each of preamplifiers which are listed in Table 8.

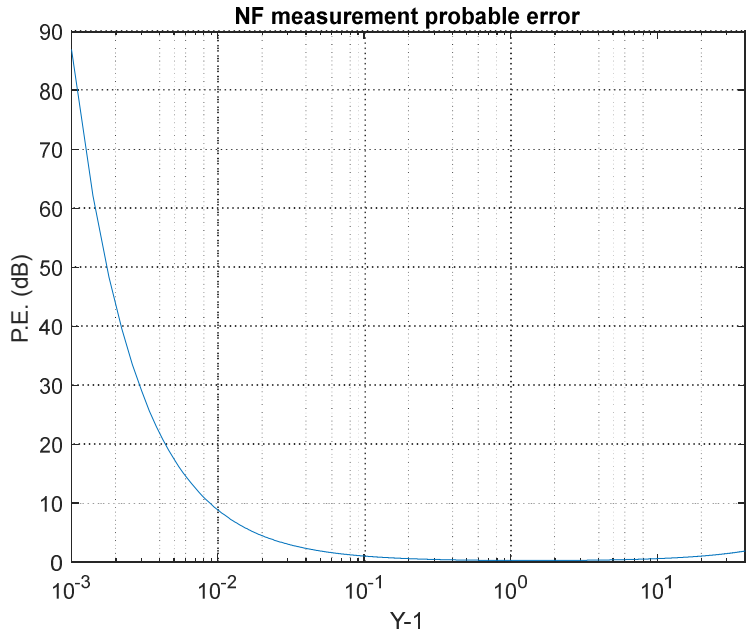

Figure 40. Reading probable error in dB corresponding to different Y values.

Overall, each NF of preamplifiers listed in Table 8 can be found by subtracting the measured NF to cable loss at different frequencies plus adding a probable error. While taking these errors into consideration and comparing with rating NF in datasheets, both the Miteq and HP preamplifiers present a very comparable measured NF while OPA847 shows a slightly higher measured NF. The measured NF of OPA847 is 2.24 dB and 0.92 dB higher than the simulated NF (9.3 dB and 4.2 dB) at 200 Mhz when R_T equals to 50 Ω and 100 kΩ respectively. One possible reason is that OPA847 is not that stable at 200 Mhz. From Figure 36, the gain flatness is not that smooth and there is an overshoot. In reality, bench measurement presents more severely while there is oscillation around the gain curve. This may cause OPA847 to become more instable around the corner frequency region. But for R_T equals to 100 kΩ, overall NF performance does not degrade so obviously and still in an acceptable range.

For the commercial preamplifiers, the measured NF also presents slightly larger at 200 Mhz. This may due to this frequency range is not isolated well in the shielding room, resulting in more noise leaking into preamplifiers.

Table 8. Calculated preamplifier NF including probable error with different preamplifiers at different frequencies. Column 1 and 2 are NF from commercial matched preamplifiers. Column 3 and 4 are measured NF from OPA847 whereas column 3 is a matched case and column 4 is used to mimic the unterminated case.

Frequency (Mhz)	Miteq1583 (dB)	HP8447A (dB)	OPA847 (dB) (R_T=50 Ω)	OPA847 (dB) (R_T=100 kΩ)
20.3	1.19 ± 0.26	6.10 ± 0.58	10.36 ± 1.39	5.65 ± 0.51
30.7	1.14 ± 0.26	6.04 ± 0.58	9.88 ± 1.27	5.68 ± 0.52
52.9	1.15 ± 0.26	6.29 ± 0.6	10.5 ± 1.49	5.67 ± 0.53
81	1.01 ± 0.26	7.31 ± 0.7	10.21 ± 1.43	4.92 ± 0.47
200.2	1.28 ± 0.27	7.66 ± 0.9	11.54 ± 2.06	5.22 ± 0.53

All above NF measurements use a 50 Ω resistor as the noise source. This is not the optimal NF case for OPA847, so it would be better to measure NF with an optimal source resistance which can be found from Figure 38. Therefore, we have tried to use a 471 Ω resistor to mimic the optimal source resistance where the simulated NF can be as low as 1.33 dB. However, a NF of 4 dB was measured for OPA847 and this presents that 2.67 dB higher than the theoretical value. With same setup, we also measured the Miteq (AU-1583) and the Hp (8447A) preamplifier NF with same source resistance. The results turn out that the Miteq and the Hp NF increased up to 3.8 dB and 11.8 dB at 200 Mhz, respectively. Due to the similar increment of the measured NF for both commercial preamplifiers and OPA847 with a 471 Ω source resistor, the Y-factor may not be so precise while measuring

NF with long coaxial cables which characteristic impedance is not matched to source resistance.

V.3.3 Image SNR versus NF at different termination resistor

Since the NF of OPA847 has been measured with Y-factor approach, we also need to verify that if the image quality will correspond to the NF. In general, image SNR will degrade while the overall NF increases. Here, imaging experiments were carried out at the Varian 4.7 T scanner. In Figure 41 (A), we can see that the transmit coil is a 19 cm diameter birdcage coil and the receive coil is a 36 mm diameter surface loop coil. In order to have a good decoupling without interfering between the birdcage and the loop coils, the birdcage coil was operated at linear mode so that the coupling can be as low as possible due to the loop coil can position at a direction where the B_1 field is perpendicular to the birdcage coil. In addition, a parallel LC trap circuit with passive diodes were placed on the receive loop coil to prevent preamplifiers from damaging by the leaking transmit RF power. Measured S_{21} between the birdcage coil and the loop coil is shown in Figure 41 (B) which is less than -50 dB at 200 Mhz. Phantom is a 2 ml, 40 mM copper sulfate solution with water placing under the loop coil.

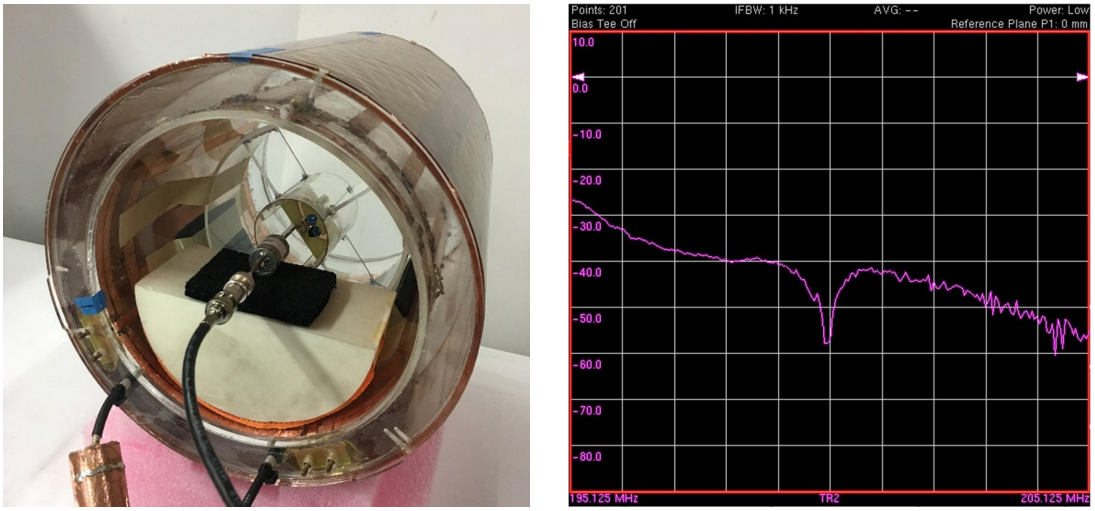

(A) (B)

Figure 41. (A) Single frequency (200 Mhz), single preamplifier image experiment coils setup and (B) decoupling measurement between transmit and receive coils. Transmit coil is a 19 cm (inner diameter) birdcage coil whereas receive coil is a 36 mm (diameter) loop coil. The birdcage coil is operated at linear mode where the receive coil can achieve a good decoupling.

Images were acquired using "sems" pulse sequence with 64 x 64 matrix, 30 mm x 30 mm FOV, 1 average, 3 mm slice thickness, 1 s repetition time, 30 ms echo time, 46030 Hz spectral width, and 1.3904 s acquisition time. To compare image quality objectively, acquired images were using same parameters on the Varian while only using different preamplifier configurations as a first amplification stage. As described previously, unterminated configuration can allow us to achieve an optimal NF. But in reality, without DC ground path, the Op Amp will act abnormally. On the other hand, using high resistance for the termination resistor (R_T) can mimic as unterminated case while the Op Amp still performs well. Thus, we will image by using different termination resistors from 50 Ω up to 100 kΩ to verify the NF performance. NF is simulated based on the noninverting noise

model developed in section V.3. Source impedance uses 50 Ω so that we can compare the simulated NF to the image without modifying hardware setup too much. In Figure 42, simulated NF is illustrated in blue curve whereas measured image SNR is plotted in red curve. We can observe that the simulated NF curve becomes flat when R_T is larger than 10 kΩ. Additionally, the NF decreases from 9.3 dB to 4.3 dB while R_T increases from 50 Ω to 10 kΩ. On the other hand, image SNR improves from 27.1 dB to 32.5 dB in the same R_T range. The difference of the simulated NF is consistent to the SNR difference, showing that the developed noise model can correspond to real image SNR variation.

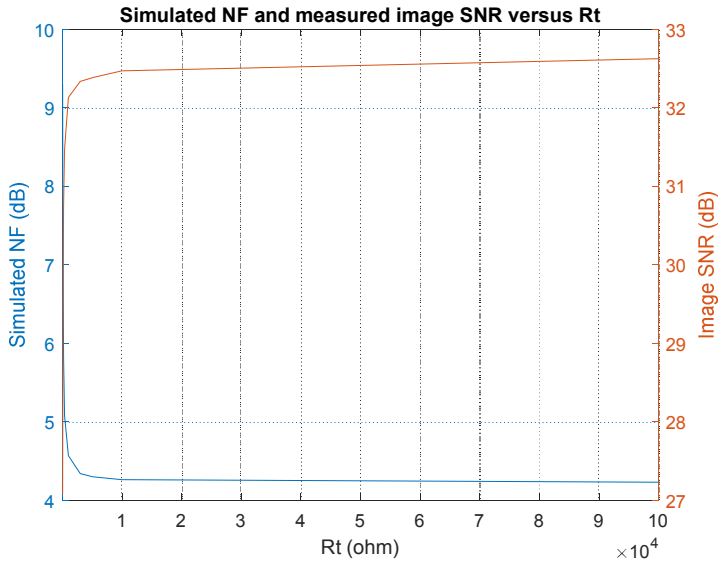

Figure 42. Simulated NF (blue curve) and image SNR (red curve) of OPA847 at different Rt where OPA847 is served as the first amplification stage preamplifier in the Varian receiver during imaging.

After verifying the variation between the simulated NF and image SNR of OPA847, we have to determine the Op Amp performance by comparing OPA847 to

commercial preamplifiers. In Table 8, the measured NF of OPA847 (R_T=100 kΩ) is 5.22 dB. This is 3.94 dB larger than the Miteq measured NF, 1.28 dB. Images were also acquired and compared between two preamplifiers which are shown in Figure 43. Image SNR acquired by the Miteq is 69.7 whereas OPA847 is 42.8. This corresponds to 4.23 dB difference. From above, both the measured NF difference and image SNR difference are less than 0.3 dB. Compared with the simulated NF, OPA847 is 4.23 dB and the Miteq is 1.1 dB. The measurements are slightly larger than the theoretical values. This could be due to the reading probable error when measuring NF and there may be some noise adding into OPA847 due to manufacture defect in the real world.

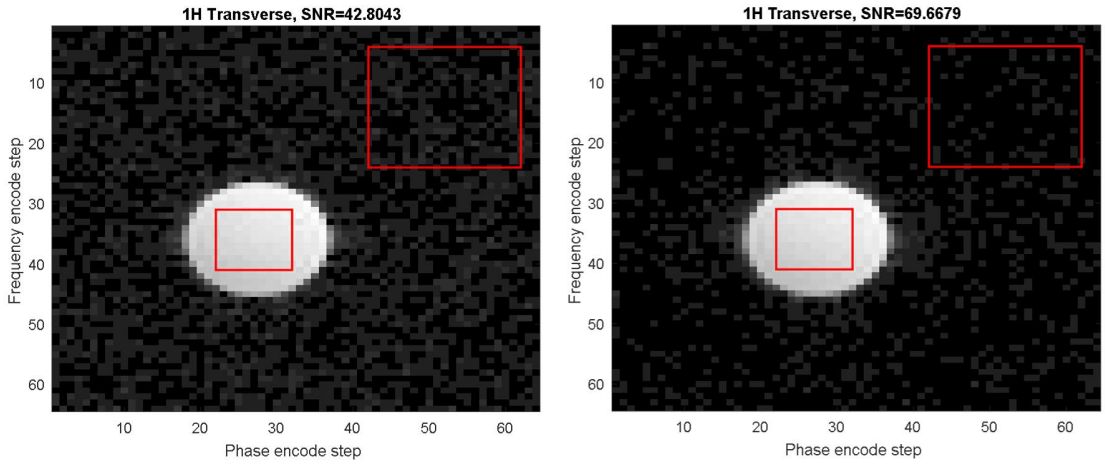

(A) (B)

Figure 43. Images acquired by using (A) OPA847 with R_T=100 kΩ and (B) Miteq1583 (B-right) as a first stage preamplifier.

V.4 Impedance transformation

The motivation of this dissertation is based on hyperpolarized studies. SNR may not so critical than fast data collection with arrays. Therefore, we assume that a NF less than 3 dB is still acceptable. In this section, NF is simulated based on OPA847 in terminated case with a terminated resistor of 100 kΩ. For matching convenience, a 3 dB NF contour on the Smith chart shown in Figure 44 is plotted based on section V.3 noise model. Any transformed coil impedance within red circle can provide a NF of less than 3 dB. So, the objective is to move the coil impedance into this 3 dB NF contour instead of matching to the preamplifier. A diameter of 4 cm loop coil geometry and a phantom with specific conductivity was used for coil impedance simulation. The simulated coil impedance at different frequencies are listed in Table 9 which will be used while analyzing NF and decoupling performance.

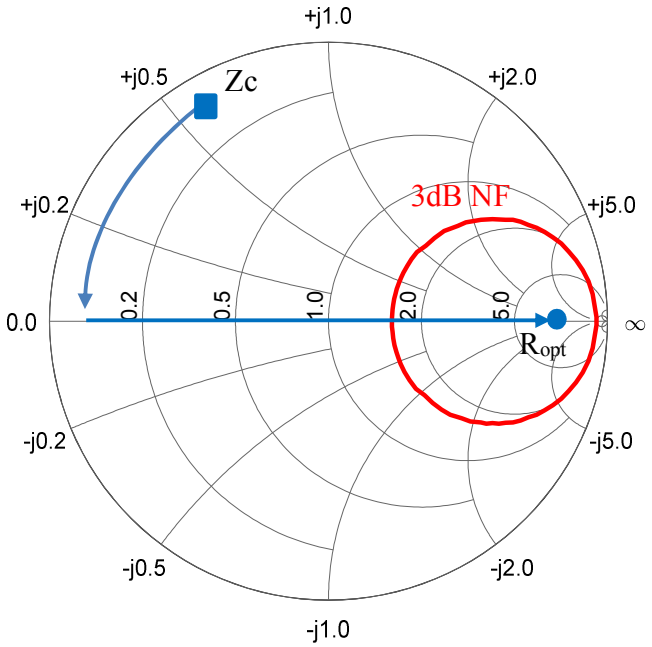

Figure 44. A simulated 3 dB NF contour (red circle) of OPA847. Input impedance of OPA847 within red circle presents a NF less than 3 dB with a minimum NF of 1.3 dB when Zin is 458 Ω. Single frequency impedance transformation is done by applying a series capacitor to cancel reactance (blue curve arrow) of a coil impedance (blue square, Z_c) and converted to an optimal source resistance (blue point, R_{opt}) with an impedance transformer (blue line arrow).

Table 9. Simulated coil impedance at different frequencies.

Frequency (Mhz)	Coil impedance (Ω)
200	3 + j128
50	0.16 + j31
20	0.072 + j12.8

Currently, there are several approaches to implement impedance transformation, e.g. transmission lines, lumped elements, and transformers. The transmission line approach is able to provide an adequate NF, but it is hard to have a high blocking impedance for decoupling. Lumped elements method has more losses while using capacitors and inductors. For transformers, it can only transform an impedance by a ratio without cancelling reactance if it is already existed. Therefore, it is somehow hard to utilize only one method to transform the coil impedance into the 3 dB NF source impedance region.

In order to study at multiple frequencies, it is desirable to series compensate the coil to minimize coil reactance at the frequency of interest. So, here we are evaluating an approach by using a combination of series resonant circuit with transformers. The equivalent hardware diagram is shown in Figure 6 (B). The principle can be easily realized by going through Figure 44 blue color part. At single frequency, the blue square represents a coil impedance. While applying a series capacitor, the impedance is transformed to pure resistance through the blue curve arrow. Then, an impedance transformer is applied to convert the resistance to the optimal NF source resistance along the blue line arrow. When it is more than one frequency, a more complicate series resonant circuit can be used, e.g. LC-C network for dual nuclei, to cancel reactance. Therefore, a multiple stage parallel LC resonant circuit in series with a capacitor were simulated in 2016 ADS at $^{1}H/^{13}C/^{15}N$ shown in Figure 45. Two parallel LCs were found to be 169 nH and 170.6 pF, 60 nH and 17.5 pF, respectively. These two series resonant LCs are in series with a capacitor which is 134.4 pF. With such configuration, the reactance before a transformer looking into the

coil at ^{1}H, ^{13}C, and ^{15}N frequency is 0.403, -0.007, and 0.012, respectively. Once the reactance is minimized at all three desired frequencies, a transformer with an impedance ratio of 512 is applied to transform the impedance to the desired NF region where the impedance at secondary winding increases by a factor of the impedance ratio between primary and secondary windings. Table 10 illustrates simulated NF for OPA847 with Figure 45 circuits at three frequencies. It appears that it is somehow hard to design a network with two stage LC resonant circuits to keep all three nuclei ($^{1}H/^{13}C/^{15}N$) within the 3 dB NF region due to OPA847 characteristic (3 dB NF source impedance region not wide enough).

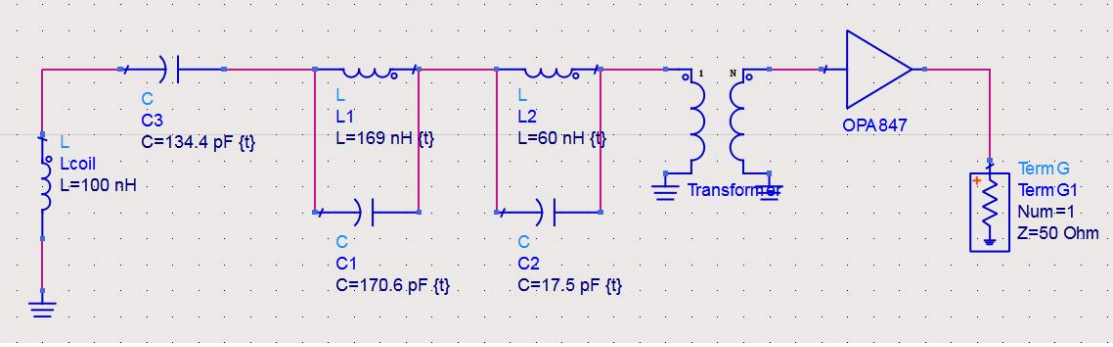

Figure 45. Two stage LC in series with a capacitor circuit. Reactance looking into coil before the transformer was minimized at $^{1}H/^{13}C/^{15}N$.

Table 10. NF analysis with impedance transformation networks at different nuclei.

Nuclei	NF (dB)
^{1}H	3.3
^{13}C	3.4
^{15}N	5.1

Even Table 10 presents a slightly larger NF at all nuclei than expected, but the simulated NF is not that large. There may be a more complex series resonant circuit or other advance low NF Op Amps with larger 3 dB NF source impedance range to improve NF performance. However, we believe that this approach is significantly less complicated than traditional multi-tuned networks since it is not matched the coil to 50 Ω at different frequencies, but transforming the coil impedance into the 3 dB NF region.

V.5 Induced current decoupling

An evaluation of OPA847 decoupling with impedance transformation networks is necessary while bad coupling can distort image quality and make images undistinguishable even NF of a preamplifier is low in the array applications. Therefore, pursuing a good isolation is desirable as well as an acceptable NF.

In general, almost no noise or NMR signal will be coupled to other coils if there are only little current flows on the surface coils during receiving process. Therefore, we have to evaluate the decoupling performance of OPA847 by applying a fixed voltage, i.e. 1 V excitation voltage source, to mimic the induced voltage from coupling effect. The induced current on the coil can be calculated by dividing the fixed voltage source to the impedance looking into the preamplifier including all impedance transformation networks

and series resonant circuits shown in Figure 6 (B). This current will be compared to the matched case induced current for decoupling evaluation where the matched case is operated when the coil is connected to its conjugate impedance. Table 11 presents decoupling analysis at ^{1}H, ^{13}C, and ^{15}N including impedance transformation networks discussed in the section V.4.

Table 11. Decoupling analysis with impedance transformation networks at different nuclei.

Nuclei	Decoupling (dB)
^{1}H	4.7
^{13}C	-22.1
^{15}N	-35.8

V.6 Discussion and conclusion

This Chapter discusses a possibility of preamp decoupling by using a high input impedance Op Amp to block input induced current from neighboring coil elements. The advantage of this approach is that Op Amps are inexpensive when compared to commercial low input impedance preamplifiers. Additionally, it can provide a very high input impedance over a wide operating range of frequencies which can be easily applied on the multinuclear array decoupling.

Op Amp noise models are developed and discussed here. Based on the noise models, OPA847 is selected and the non-inverting structure is used as the main design diagram due to its low NF performance. The amplifier performance is conducted by using

TINA-TI simulation and gain curve are measured on the bench for both unterminated and terminated structures. A final design is recommended to use the terminated structure with a termination resistor of 100 kΩ to mimic the unterminated case as well as maintaining a similar NF but can eliminating DC ground path issue for the Op Amp. Overall, the design can have a gain of about 26 dB when frequency is below 200 Mhz.

NF of OPA847 is conducted by using Y-factor and compared to commercial preamplifiers, i.e. Miteq1583, to verify the added noise by the Op Amp. For a 50 Ω noise source, OPA847 (R_T=100 kΩ) has a measured NF of 5.22 dB whereas the Miteq measured NF is 1.28 dB. In addition, images are also obtained to verify SNR performance by using two preamplifiers with experiment setup fixed. The image SNR acquired by OPA847 is 4.23 dB larger than the Miteq, which could correspond to the measured NF difference. However, the measured NF presents about 2.7 dB larger than theoretical NF for both OPA847 and the Miteq preamplifier while using an optimal source resistance of 471 Ω at 200 Mhz. This could be due to cable characteristic impedance between the noise source and preamplifiers are not matched, resulting in inaccurate measurements with Y-factor approach. Currently, we are not able to solve this issue due to limited time. But in the future, one possible approach is that we can use commercial noise sources for NF measurement to reduce transmission line effect between the noise source and the preamplifiers. Another approach is more expensive and may not be practical which is to customize a cable with desired characteristic impedance which is same to the noise source.

Impedance transformation of the coil impedance and induced current decoupling are also evaluated in this chapter for preliminary study of preamp decoupling with an Op

Amp. A series LC-LC-C resonant circuit was simulated by 2016 ADS to minimize coil reactance at $^{1}H/^{13}C/^{15}N$ before the transformer. A turn ratio of 512 was used for the transformer while calculating source impedance for OPA847. The simulated NF are 3.3 dB, 3.4 dB, and 5.1 dB for ^{1}H, ^{13}C and ^{15}N, respectively. This shows that NF is slightly larger than we expected. There may be more complex series resonant circuit or other advance low NF Op Amps with larger 3 dB NF source impedance range to improve NF performance. For decoupling simulation, both ^{13}C and ^{15}N present a decoupling less than -22 dB with the resonant circuit, but ^{1}H shows a strong coupling. As our targeted nuclei is X-nuclei, ^{1}H is used as a reference signal and may not that critical at this point. However, future study should focus on decreasing ^{1}H decoupling while still maintaining X-nuclei decoupling performance as well as keeping overall NF as low as possible.

CHAPTER VI

CONCLUSIONS AND FUTURE WORKS

VI.1 Conclusions

Here, we investigate a frequency multiplexing approach that allows use of a single digitizer channel for multiple nuclei but is still able to perform individual signal conditioning for each nucleus. The proposed front-end is able to split the incoming broadband signal into multiple paths for filtering and provide separate gain control for each signal path to best use the digitizer's dynamic range. The easy construction of the triplexer allows researchers to apply this to different nuclei by swapping cables and filters, and it makes it straightforward to transition to different magnetic field strengths.

RF filtering front-end performance was verified at simultaneous multinuclear MRI and MRS at $^{1}H/^{23}Na/^{2}H$ and $^{1}H/^{13}C/^{15}N$. Both at enriched and naturally occurring condition were investigated with the triplexer front-end filtering. The triplexer front-end can perform as well as a commercial Varian Unity Inova system while applying in simultaneous multinuclear acquisition but using less acquisition time. A comparison of using 1 ADC digitization for three nuclei can present similar performance while digitizing all nuclei separately in each channel. This proves that the triplexer front-end allows researchers to use only 1 ADC channel of the digitizer while other channels still remain available but not sacrificing SNR performance. The triplexer loss is also conducted by comparing to using a low pass filtering approach. The image results show that the triplexer front-end can achieve at a larger SNR at all nuclei because it can provide separate gain control and proper filtering at each path independently. Lastly, signal dynamic range is

investigated by comparing ^{13}C and ^{1}H spectroscopy either setting an optimal constant gain at proton and carbon separately with a low pass filtering approach in a single channel. The triplexer front-end shows a great improvement on SNR performance while comparing to the low pass filtering approaches because separate signal conditioning allows us to best use of a digitizer's dynamic and be able to filter out of band noise, and optimize the SNR.

Applying arrays is inevitable in the next few years for simultaneous multiple nuclear acquisition because it can have better sensitivity on the NMR signal and less scan time. Decoupling between multiband array elements will be a key factor since it can degrade SNR performance as well as in single nuclear acquisition. A low decoupling preamp approach based on an Op Amp was evaluated due to its high input impedance and low NF across a wide range of source impedance characteristics. A noninverting Op Amp noise model was developed to find an optimal NF condition. OPA847 was chosen based on the noise model which gives out an optimal NF of 1.3 dB. NF of OPA847 (with a 100 kΩ termination resistor) was measured to verify the developed noise model performance and compared to commercial preamplifiers with Y-factor approach when source impedance is 50 Ω. All measured NFs were in a comparable region while comparing with theoretical values. Impedance transformation technique was discussed based on a transformer to convert a coil impedance to around 3 dB NF region for both ^{1}H and ^{13}C, and 5 dB at ^{15}N. Current decoupling simulation of OPA847 was conducted with the series resonant circuit where the decoupling is below -22 dB for both ^{13}C and ^{15}N except for ^{1}H. Overall, the evaluation of Op Amp decoupling approach provides a possibility on

multiband array with an ease and fixed structure over conventional cumbersome resonant circuits.

VI.2 Improvements and future work

As discussed in section III.3.1, the digitizer in the current broadband system acquires a noise bandwidth up to 700 Mhz even though an external antialiasing filter is applied at the input of the digitizer. This could lead to a smaller SNR while using a lower sampling rate with undersampling technique if a dominated noise level is low. One possible improvement on this is to implement an advanced digitizer which sampling rate can cover at least twice of the highest interested nuclear Larmor frequency. This can simplify the system structure at the receive side, i.e. there is no need to apply filtering before digitization by direct sampling. Another possible improvement is to use a multiple DDC core digitizer with internal narrow band filtering. This approach is more economical than using a very high-speed digitizer due to generating less data throughput and also reduce post data processing load.

With the proposed reconfigurable front-end filtering for simultaneous multinuclear acquisition, digital step attenuators can be implemented and integrated into current control console to replace analog attenuators for the ease of operation. Another advantage of using digital attenuators is they can make the gain setting more stable and precise since gain step resolution can be better and no need to plug and unplug hardware back and forth.

The proposed front-end in chapter IV has demonstrated the feasibility of acquiring multiple nuclear MR imaging and spectroscopy simultaneously with high concentration ^{23}Na and enriched ^{13}C, ^{15}N instead of using hyperpolarization technique. In TAMU,

Hilty's group has been involving with DNP research including ^{13}C spectroscopy at a 400 Mhz NMR spectrometer [65]. For the proposed front-end, even the frequency cannot support ^{1}H frequency at 9.4 T, but it is enough for most of X-nuclei. This allows us to implement preclinical studies on simultaneous acquisition with hyperpolarization at both ^{13}C and ^{15}N with the proposed front-end.

Section V.3.2 has discussed about the NF measurement of an Op Amp while source impedance is not matched to cable impedance with Y-factor. Both the proposed Op Amp and a commercial Miteq preamplifier have a larger NF than theoretical values. Possible solution to reduce mismatch issue could be either using commercial noise sources for NF measurement to reduce transmission line effect between the noise source and the preamplifiers or customizing a cable with desired characteristic impedance which is same to the optimized noise source. But the later approach would be more expensive and may not so practical if using different Op Amps. Moreover, impedance transformation with transformers has been discussed in section V.4 theoretically. A physical hardware of impedance transformation based on the discussion is necessary to verify low NF Op Amp performance as well as blocking function. Multiple element array is also required while the proposed preamps can be applied at each coil element and investigate decoupling performance between these elements.

REFERENCES

[1] R. L. Siegel, K. D. Miller, and A. Jemal, "Cancer statistics, 2018," *CA: A Cancer Journal for Clinicians,* vol. 68, no. 1, pp. 7-30, 2018.

[2] N. Ahmed *et al.*, "Metabolic Signatures of Lung Cancer in Sputum and Exhaled Breath Condensate Detected by 1H Magnetic Resonance Spectroscopy: A Feasibility Study," *Magnetic Resonance Insights,* vol. 9, pp. 29-35, 2016.

[3] S. Uma, S. Rani Gupta, and R. J. Naranamangalam, "Magnetic Resonance Imaging (MRI) and Spectroscopy (MRS) in Breast Cancer," *Magnetic Resonance Insights,* vol. 2, pp. 93-108, 2008.

[4] H. Wen, Y. J. An, W. J. Xu, K. W. Kang, and S. Park, "Real-Time Monitoring of Cancer Cell Metabolism and Effects of an Anticancer Agent using 2D In-Cell NMR Spectroscopy," *Angewandte Chemie International Edition,* vol. 54, no. 18, pp. 5374-5377, 2015.

[5] B. Condon, "Magnetic resonance imaging and spectroscopy: how useful is it for prediction and prognosis?," *The EPMA Journal,* vol. 2, no. 4, pp. 403-410, 2011.

[6] T. Schaeffter and H. Dahnke, "Magnetic Resonance Imaging and Spectroscopy," in *Molecular Imaging I*, W. Semmler and M. Schwaiger, Eds. Berlin, Heidelberg: Springer Berlin Heidelberg, 2008, pp. 75-90.

[7] Y. He *et al.*, "Simultaneous acquisition of multi-nuclei enhanced NMR/MRI by solution-state dynamic nuclear polarization," *Science China Chemistry,* vol. 59, no. 7, pp. 830-835, 2016.

[8] H. Gutte *et al.*, "The use of dynamic nuclear polarization 13C-pyruvate MRS in cancer," *American Journal of Nuclear Medicine and Molecular Imaging,* vol. 5, no. 5, pp. 548-560, 2015.

[9] J. H. Lee, Y. Okuno, and S. Cavagnero, "Sensitivity Enhancement in Solution NMR: Emerging Ideas and New Frontiers," *Journal of magnetic resonance* vol. 241, pp. 18-31, 2014.

[10] A. Miccheli *et al.*, "Metabolic profiling by 13C-NMR spectroscopy: [1,2-13C2]glucose reveals a heterogeneous metabolism in human leukemia T cells," *Biochimie,* vol. 88, no. 5, pp. 437-448, 2006.

[11] J. P. Wijnen *et al.*, "In vivo 13C magnetic resonance spectroscopy of a human brain tumor after application of 13C-1-enriched glucose," *Magnetic Resonance Imaging,* vol. 28, no. 5, pp. 690-697, 2010.

[12] I. Tea *et al.*, "13C and 15N natural isotope abundance reflects breast cancer cell metabolism," *Scientific Reports,* vol. 6, p. 34251, 2016.

[13] R. Ouwerkerk *et al.*, "Elevated tissue sodium concentration in malignant breast lesions detected with non-invasive 23Na MRI," *Breast Cancer Research and Treatment,* vol. 106, no. 2, pp. 151-160, 2007.

[14] G. Madelin and R. R. Regatte, "Biomedical Applications of Sodium MRI In Vivo," *Journal of magnetic resonance imaging : JMRI,* vol. 38, no. 3, pp. 511-529, 2013.

[15] N. V. Anisimov and O. S. Pavlova, "Simultaneous Recording of NMR Signals from Nuclei with Different Gyromagnetic Ratios Using Undersampling Technique," *Applied Magnetic Resonance,* journal article vol. 49, no. 5, pp. 523-532, 2018.

[16] M. Meyerspeer, A. W. Magill, A. Kuehne, R. Gruetter, E. Moser, and A. I. Schmid, "Simultaneous and interleaved acquisition of NMR signals from different nuclei with a clinical MRI scanner," *Magnetic Resonance in Medicine,* vol. 76, no. 5, pp. 1636-1641, 2016.

[17] H. Kovacs and Ē. Kupče, "Parallel NMR spectroscopy with simultaneous detection of 1H and 19F nuclei," *Magnetic Resonance in Chemistry,* vol. 54, no. 7, p. 543, 2016.

[18] J. R. Fitzsimmons, B. L. Beck, and H. Ralph Brooker, "Double resonant quadrature birdcage," *Magnetic Resonance in Medicine,* vol. 30, no. 1, pp. 107-114, 1993.

[19] G. Isaac, M. D. Schnall, R. E. Lenkinski, and K. Vogele, "A design for a double-tuned birdcage coil for use in an integrated MRI/MRS examination," *Journal of Magnetic Resonance,* vol. 89, no. 1, pp. 41-50, 1990.

[20] M. D. Schnall, V. Harihara Subramanian, J. S. Leigh, L. Gyulai, A. McLaughlin, and B. Chance, "A technique for simultaneous 1H and 31P NMR at 2.2 T in Vivo," *Journal of Magnetic Resonance,* vol. 63, no. 2, pp. 401-405, 1985.

[21] K. R. Thulborn, N. F. Soffe, and G. K. Radda, "Simultaneous in vivo measurement of oxygen utilization and high-energy phosphate metabolism in rabbit skeletal muscle by multinuclear 1H and 31P NMR," *Journal of Magnetic Resonance,* vol. 45, no. 2, pp. 362-366, 1981.

[22] J. H. Ardenkjær-Larsen *et al.*, "Increase in signal-to-noise ratio of > 10,000 times in liquid-state NMR," *Proceedings of the National Academy of Sciences,* vol. 100, no. 18, p. 10158, 2003.

[23] D. Ma *et al.*, "Magnetic Resonance Fingerprinting," *Nature,* vol. 495, no. 7440, pp. 187-192, 2013.

[24] M. R. Smith *et al.*, "In Vivo Imaging and Spectroscopy of Dynamic Metabolism Using Simultaneous 13C and 1H MRI," *IEEE Transactions on Biomedical Engineering,* vol. 59, no. 1, pp. 45-49, 2012.

[25] A. Reykowski, S. M. Wright, and J. R. Porter, "Design of Matching Networks for Low Noise Preamplifiers," *Magnetic Resonance in Medicine,* vol. 33, no. 6, pp. 848-852, 1995.

[26] M. S. Ramirez, et al., "Resonance Shift Decoupling: A Potential Alternative to Low Input Impedance Preamplifiers," *17th International Society for Magnetic Resonance Medicine Annual Meeting,* p. 103, 2009.

[27] S. B. King, "The Effects of Ultra Low Input Impedance Preamplifiers on Phased Array Coil Design," *10th International Society for Magnetic Resonance Medicine Annual Meeting,* p. 330, 2002.

[28] J. Jevtic, "Ladder Networks for Capacitive Decoupling in Phased-Array Coils," *9th International Society for Magnetic Resonance Medicine Annual Meeting,* p. 17, 2001.

[29] P. B. Roemer, W. A. Edelstein, C. Hayes, S. P. Souza, and O. M. Mueller, *NMR phased array*. 1990, pp. 192-225.

[30] R. K. Harris, "Nuclear Spin Properties and Notation," in *eMagRes*, 2007, pp. 2-3.

[31] D. B Plewes and W. Kucharczyk, *Physics of MRI: A primer*. 2012.

[32] D. Weishaupt, V. D. Köchli, and B. Marincek, *How Does MRI Work? An Introduction to the Physics and Function of Magnetic Resonance Imaging*. 2006.

[33] Z. P. Liang, *Principles of Magnetic Resonance Imaging : A Signal Processing Perspective*. 1999.

[34] B. R. Plantinga *et al.*, "Ultra-high field magnetic resonance imaging of the basal ganglia and related structures," *Frontiers in Human Neuroscience,* Technology Report vol. 8, no. 876, 2014.

[35] P. Balchandani and T. P. Naidich, *Ultra-High-Field MR Neuroimaging*. 2014.

[36] K. Wachowicz, *Evaluation of active and passive shimming in magnetic resonance imaging*. 2014, p. 1.

[37] E. Boskamp, "Volume and Surface Coils (Educational topic)," *21th International Society for Magnetic Resonance Medicine Annual Meeting,* 2013.

[38] G. Giovannetti *et al.*, "Comparison between volume and surface coils for pig cardiac metabolism studies with hyperpolarized 13C MRS," *Journal of Cardiovascular Magnetic Resonance,* vol. 13, no. Suppl 1, p. 343, 2011.

[39] J. H. Kalkavage, K. G. Petrillo, E. J. Adles, and T. R. Clark, "Photonic downsampling receiver for millimeter-wave communications," in *2017 IEEE Photonics Conference (IPC)*, 2017, pp. 213-214.

[40] R. P. S. Rathore, "Reconfigurable digital radar receiver implemented in FPGA using Under-sampling, Direct IQ generation, Multi-rate filter and pulse compression," in *2014 IEEE International Microwave and RF Conference (IMaRC)*, 2014, pp. 174-177.

[41] M. L. Zierhut *et al.*, "Kinetic modeling of hyperpolarized 13C1-pyruvate metabolism in normal rats and TRAMP mice," *Journal of magnetic resonance,* vol. 202, no. 1, pp. 85-92, 2010.

[42] B. Keil and L. L. Wald, "Massively parallel MRI detector arrays," *Journal of Magnetic Resonance,* vol. 229, pp. 75-89, 2013.

[43] A. Deshmane, V. Gulani, M. A. Griswold, and N. Seiberlich, "Parallel MR Imaging," *Journal of magnetic resonance imaging : JMRI,* vol. 36, no. 1, pp. 55-72, 2012.

[44] C. Stumpf, M. Malzacher, and L.-P. Schmidt, "Radio Frequency Modeling of Receive Coil Arrays for Magnetic Resonance Imaging," *Journal of Imaging,* vol. 4, no. 5, p. 67, 2018.

[45] S. M. Wright and L. L. Wald, "Theory and application of array coils in MR spectroscopy," *NMR in Biomedicine,* vol. 10, no. 8, pp. 394-410, 1997.

[46] H. T. Friis, "Noise Figures of Radio Receivers," *Proceedings of the IRE,* vol. 32, no. 7, pp. 419-422, 1944.

[47] X. Cao, D. Zu, X. Zhao, Y. Fan, and J. Gao, *The design of a low-noise preamplifier for MRI*. 2011, pp. 1766-1770.

[48] D. I. Hoult and R. E. Richards, "The signal-to-noise ratio of the nuclear magnetic resonance experiment," *Journal of Magnetic Resonance,* vol. 24, no. 1, pp. 71-85, 1976.

[49] M. P. McDougall and S. M. Wright, "A Parallel Imaging Approach to Wide-field MR Microscopy," *Magnetic Resonance in Medicine,* vol. 68, no. 3, pp. 850-856, 2012.

[50] J. A. Bankson and S. M. Wright, "Simulation-based investigation of partially parallel imaging with a linear array at high accelerations," *Magnetic Resonance in Medicine,* vol. 47, no. 4, pp. 777-786, 2002.

[51] J. Karki, "Calculating noise figure in op amps," *Analog Applic.,* vol. 4Q, pp. 31-37, 2003.

[52] C. Huang, S. E. Ogier, M. Gu, and S. M. Wright, "Flexible RF Filtering Front-End For Simultaneous Multinuclear MR Spectroscopy," in *40th Annual International Conference of the IEEE Engineering in Medicine and Biology Society (EMBC)*, 2018, pp. 1368-1371.

[53] J. A. Bankson and S. M. Wright, "Multi-channel magnetic resonance spectroscopy through time domain multiplexing," *Magnetic Resonance Imaging,* vol. 19, no. 7, pp. 1001-1008, 2001.

[54] M. M. Mansour, A. A. T. Shalaby, E. S. M. El-Rabaie, and N. W. Messiha, "Design and simulation of microwave diplexer based on D-CRLH metamaterials," in *2014 International Conference on Engineering and Technology (ICET)*, 2014, pp. 1-5.

[55] Q. Xu, H. Wang, Z. Xu, and G. Li, "Frequency domain multiplexing for parallel acquisition of MR images," *Electronics Letters,* vol. 42, no. 6, pp. 326-327, 2006.

[56] T. Instruments, "Wideband, Low Distortion, Medium Gain, Voltage-Feedback Operational Amplifier (Rev. C)," p. OPA843 datasheet, 2008.

[57] C.-H. Huang, H. Dong, S. E. Ogier, C. Sun, and S. M. Wright, "A triple tuned coil and front-end for simultaneous multinuclear MR imaging and spectroscopy," in *27th International Society for Magnetic Resonance Medicine Annual Meeting (#1580)*, 2019.

[58] J. C. B. Stephen Ogier, and Steven M. Wright, "A Broadband Spectrometer for Simultaneous Multinuclear Magnetic Resonance Imaging and Spectroscopy," *24th International Society for Magnetic Resonance Medicine Meeting (#0546),* 2016.

[59] B. N. T. Peter J. Mohr, David B. Newell, "CODATA recommended values of the fundamental physical constants: 2006," *J. Phys. Chem. Ref. Data,* vol. 37, no. 3, 2006.

[60] D. Gust, R. B. Moon, and J. D. Roberts, "Applications of natural-abundance nitrogen-15 nuclear magnetic resonance to large biochemically important molecules," *Proc Natl Acad Sci U S A,* vol. 72, no. 12, pp. 4696-4700, Dec 1975.

[61] M. Piotto, V. Saudek, and V. Sklenář, *Gradient-Tailored Excitation for Single-Quantum NMR Spectroscopy of Aqueous Solutions*. 1992, pp. 661-665.

[62] P. Plateau and M. Gueron, "Exchangeable proton NMR without base-line distorsion, using new strong-pulse sequences," *Journal of the American Chemical Society,* vol. 104, no. 25, pp. 7310-7311, 1982.

[63] T. Instruments, "Wideband, Ultra-Low Noise, Voltage-Feedback Operational Amplifier with Shutdown," p. OPA847 datasheet, Jul. 2002 [Revised Dec. 2008].

[64] W. W. a. S. Mumford, Elmer H, *Noise performance factors in communication systems*. Dedham, Mass: Horizon House-Microwave, 1968.

[65] G. Zhang, S. Ahola, M. H. Lerche, V.-V. Telkki, and C. Hilty, "Identification of Intracellular and Extracellular Metabolites in Cancer Cells Using 13C Hyperpolarized Ultrafast Laplace NMR," *Analytical Chemistry,* vol. 90, no. 18, pp. 11131-11137, 2018.